Developing advanced MR imaging to assess spinal cord function and tract integrity

Moreno Pasin

Dissertation submitted for the degree of:

Doctor of Philosophy

in MRI Physics

NMR Research Unit

Department of Neuroinflammation

UCL Institute of Neurology

University College London

Declaration

I, Moreno Pasin, confirm that the work presented in this thesis is my own.

Where information has been derived from other sources, I confirm that this has been indicated in the thesis.

London, 16th December 2014.

Abstract

The overall purpose of this thesis is to develop a way to match diffusion and functional acquisition techniques in the spinal cord (SC) in order to offer a comprehensive assessment of factors responsible for functional and structural integrity. I began by optimising a pipeline to acquire and process spinal functional data and I finished by matching the functional information with that derived from diffusion imaging (DI) performed during the same scan session as fMRI. In order to characterize the interactions between local structural connections (derived from DI) and functional activation of the SC it has been necessary to develop an imaging protocol that acquires transverse SC images with both modalities, matching their spatial and geometrical characteristics. This is because transverse cord images possess the relevant anatomical information in terms of grey-white matter structure and allow better localisation of the functional response and structural properties within the spinal cord. My main contribution to the field has been:

1. To demonstrate that it is possible to use the "ZOOM" sequence for spinal fMRI

2. To characterize the signal obtained and the comparison of different image analysis approaches

3. To propose a final pipeline for acquisition and analysis of spinal fMRI

4. To demonstrate that there is a dependency of pathological functional and structural changes

The same ZOOM-EPI sequence has been applied for all the functional studies reported in this thesis. The outcome of the optimisation for spinal fMRI has been matched by a DI protocol, using standard DI parameters for spinal microstructural characterization and constitutes the final MR protocol used in a pilot study including a group of healthy controls and a group of patients

affected by multiple sclerosis (MS). Based on the gathered experience and results from data acquired and analysed over the years I have concluded with some recommendations for future studies and development strategies for structural and functional MRI of the spinal cord.

Acknowledgements

Sincere acknowledgements are due to those people that contributed - in any way - to the realization of this project: I can hardly express how grateful I am to them all.

*In particular, I would like to thank **A LOT** my supervisors Dr Claudia Wheeler-Kingshott and Dr Ahmed Toosy for their availability to develop this project throughout the years.*

I would like to really thank Dr Marios Yiannakas - best radiographer ever - whose help has been essential for the experimental part of each spinal fMRI experiment.

Thanks to Mr Pavlou for building the electric device that I used in this thesis for delivering sensory stimulation.

I would like to thank Dr Paul Summers for his really experienced advice and opinions about spinal fMRI.

Volunteers' and patients' time has been essential too, without them I would have had no data to work with.

And a huge 'THANKS!!!' to Patrizia and Gianfranco, as always.

Thank you

Moreno Pasin

Ma s' io avessi previsto tutto questo,
dati causa e pretesto, forse, farei lo stesso.

(cit. F.Guccini)

TABLE OF CONTENTS

CHAPTER 3 – FUNCTIONAL MRI IN THE SPINAL CORD

CHAPTER 4 – PREPROCESSING

CHAPTER 5 – PHYSIOLOGICAL NOISE

CHAPTER 6 – HAEMODYNAMIC RESPONSE FUNCTION(s)

Introduction

6.1 - Neurovascular coupling as a confound in functional MRI

6.2 - The Haemodynamic Response Function

6.3 - The spinal HRF

- 6.3.1 - Purpose
- 6.3.2 - Materials and Methods
- 6.3.3 - Results
- 6.3.4 - Conclusion and Discussion

CHAPTER 7 – SPINAL FMRI WITH MOTOR AND SENSORY STIMULI

Introduction

7.1 - Spinal functional study with motor paradigm

- 7.1.1 - Purpose
- 7.1.2 - Materials and Methods
- 7.1.3 - Results
- 7.2.4 - Discussion

7.2 - Spinal functional study with sensory paradigm

- 7.2.1 - Purpose
- 7.2.2 - Materials and Methods
- 7.2.3 - Results
- 7.2.4 - Discussion

7.3 - Conclusion

CHAPTER 8 – FUNCTIONAL–STRUCTURAL RELATIONSHIP IN THE CERVICAL SPINAL CORD: APPLICATION TO MULTIPLE SCLEROSIS

Introduction

LIST OF TABLES

LIST OF FIGURES

Fig. 4.4: Number of activated voxels within the SC of the 5 subjects obtained using Slice Timing Correction (STC), Temporal Derivatives (TD) and not applying any correction (UN).

Fig. 4.5: Histograms of the mean t-values for the activated voxels within the SC of the 5 subjects obtained using Slice Timing Correction (STC), Temporal Derivatives (TD) and not applying any correction (UN).

Fig. 4.6: Activations detected in the 5 subjects applying 2 mm FWHM smoothing (in yellow) and no-smoothing (in red) overlaid on the mean image. The slice number refers to Fig. 4.3.

Fig. 5.1: Schematic illustration of the cardiac phase φ_c for the slice acquired at the time τ (vertical black line) between the two R-wave peaks t_1 and t_2. The cardiac trace is shown in red.

Fig. 5.2: Schematic illustration explaining how to obtain the H(b) histogram. Respiratory peaks, slice acquired at the time τ and normalised respiratory amplitude are depicted. The recorded points of the respiratory trace corresponding to the b-th bin are shown in red and indicated by red arrows.

Fig. 5.3: Schematic illustration of the histogram H(b). The respiratory phase of the slice acquired at the time corresponding to the b-th bin can be represented as the ratio between two regions of the histogram, as indicated in the formula reported in the picture.

Fig. 5.4: Example of plot of the physiological file downloaded from the scanner showing the patterns of the gradients (vertical lines in green and black) and the physiological traces (the black curve is the respiratory trace and the red one, smaller, is the cardiac trace; see Fig. 5.6).

Fig. 5.5: Plot of the traces of the gradients during the acquisition of 3 slices. Different colours are used for each gradient (G_x in green, G_y in red, G_z in black).

Fig. 5.6: Plots of the cardiac (in red) and respiratory (in black) traces from the physiological file downloaded from the scanner. Regular recording is displayed in the figure at the top and irregular recording is shown in the figure at the bottom.

Fig. 5.7: Localization of the slices. Only activations localized in the 6 central slices (from slice 3 to slice 8) covering the whole C6 segment were considered.

Fig. 5.8: Activations in the 3 subjects obtained using the RETROICOR method (a; in red) and the DRIFTER software (a; in green) corrections. Yellow voxels (a) indicate overlapping between results obtained with the two different approaches. Activations obtained without applying any physiological correction are displayed for each subject as well (b; in light-blue). Activations are overlaid on the mean image. Slice numbers refer to Fig. 5.7.

Fig. 5.9: Activated voxels found in the 3 subjects during the first (a) and the second (b) scans. Left and right hemicords are divided by a central line. In subject 1 (a) two voxels in the slice 8 and one in the slice 6 are deemed in the CSF. In subject 3 (a and b) one voxel in the slice 4 is deemed in the CSF. Slice numbers refer to Fig. 5.7.

Fig. 6.1: Canonical HRF (dashed line) and spinal HRF used in this study.

Fig. 6.2: Activations in the 3 subjects using the canonical HRF (in red) and the spinal HRF (in light-blue). Yellow voxels indicate overlapping between results obtained with the two different HRFs.

Fig. 7.1: Localization of the slices. Slices 1,2 and 3 were included in T1 vertebral level; slices 4,5 and 6 in C7; slices 7,8 and 9 in C6.

Fig. 7.2: Total number of ipsilateral (in yellow) and contralateral (in blue) activated voxels over all subjects in C6, C7 and T1 spinal segments, considering both right and left stimulation.

Fig. 7.3: Activations in the 9 slices for all subjects for right (in red) and left (in green) hand finger-tapping. Activated voxels are overlaid on the mean image. Slice order refers to that shown in Fig. 7.1.

Fig. 7.4: Average signal time course for the activated voxels inside the SC for both right and left hand stimulus.

Fig. 7.5: Locatization of the 9 slices. The slices were always centred transverse to the cord and the central slice was always placed in the middle of the C6 spinal segment.

Fig. 7.6: Activations in the 6 central slices for the 10 subjects for right (in red) and left (in green) hand stimulation. Activated voxels are overlaid on the mean image. Slice order refers to that shown in Fig. 7.5.

Fig. 7.7: Average signal time course for the activated voxels inside the SC for both R-H and L-H stimulus.

Fig. 7.8: Total number of ipsilateral (in yellow) and contralateral (in blue) activated voxels over all subjects in the 6 analyzed slices, considering both right and left stimulation. Slice numbers refer to Fig. 7.5.

Fig. 8.1: Localization of the slices.

Fig. 8.2: Activations in the 6 central slices for the 10 controls for right (in red) and left (in green) hand stimulation. Activated voxels are overlaid on the mean image. Slice order refers to that shown in Fig. 8.1.

Fig. 8.3: Activations in the 6 central slices for the 9 MS patients for right (in red) and left (in green) hand stimulation. Activated voxels are overlaid on the mean image. Slice order refers to that shown in Fig. 8.1.

Fig. 8.4 : Spinal activity in one of the subjects for left (a; in green) and right (b; in red) hand stimulation overlaid to the mean image. The number of the slice refers to Fig.1. In the count of activated voxels, only those within the SC and excluded by the CSF mask, were taken into account The blue rectangles show the voxels considered for the CSF mask. In c) it is shown an example of the b0 images associated with the same slices and overlaid the LH (in yellow) and the PCWM (in red) masks.

Fig. 8.5: Average time course of all activated voxels within the spinal cord of 10 controls for both right and left task. Activation epochs are indicated by black lines.

Fig. 8.6: Average time course of all activated voxels within the spinal cord of 9 MS patients for both right and left task. Activation epochs are indicated by black lines.

Fig. 8.7: Mean values of fractional anisotropy (FA) calculated for the 10 controls (HC, in green) and the 9 MS patients (MS, in red) referring to 4 different kinds of ROIs covering: whole cord (WC), right hemisphere (RH), left hemisphere (LH) and posterior column white matter (PCWM).

Fig. 8.8: Correlation between fractional anisotropy (FA) calculated in the posterior column white matter (PCWM) for MS patients and overall lateralization index (LI) [$p=0.025$; R^2linear$=0.631$].

Fig. 8.9: Correlation in MS patients between EDSS and overall lateralization index (LI) [p=0.002; R^2linear=0.773].

CHAPTER 1 – PRINCIPLES OF MAGNETIC RESONANCE IMAGING

Introduction

In this chapter, a description of physical properties of a single spin in a magnetic field is reported. Dynamics of spins in bulk material is also discussed and it is shown that, when a steady and homogeneous magnetic field $\vec{B}_0$ is switched on, it gives rise to a bulk magnetization $\vec{M}$ precessing around the direction of $\vec{B}_0$ with a characteristic frequency ω_L, called Larmor frequency. Moreover, it is described how, applying a magnetic field $\vec{H}_1$ oscillating at the Larmor frequency, it is possible to drive the magnetization. Both classical and quantum mechanics approaches are reported and it is underlined that they both lead to the same results.

Finally, Bloch equations describing the motion of $\vec{M}$ are reported and it is explained that the intensity of the signal depends on the density of nuclear magnetic moments generating $\vec{M}$ and on the rate (T_1 and T_2 relaxation times) at which the signal decays due to interactions between the spins and their surroundings.

1.1 - Magnetic properties of the atomic nucleus

Magnetic Resonance Imaging (MRI) relies on a physical property, common to most nuclei, to have a spin angular momentum $\vec{I}$ not null. The measurable values of the projection of this momentum along any random direction, for example along the $\hat{z}$ axis, are: $I_z = \hbar\, I,\ \hbar(I-1), \hbar(I-2), \ldots, -\hbar(I-2), -\hbar(I-1), -\hbar\, I$. These nuclei have got an associated magnetic moment:

$$\vec{\mu} = \gamma\, \vec{I} \qquad \text{Eq. 1.1}$$

with γ indicating the gyromagnetic ratio (that is a constant depending on the nucleus) and $\hbar$ (~1.055×10^{-34} J·sec) is the Planck constant divided by 2π (Andrew, 1955; Abragam, 1961). The magnetic moment $\vec{\mu}$ is quantized as well along the $\hat{z}$ direction:

$$\mu_z = \gamma\, I_z \qquad \text{Eq. 1.2}$$

Only those nuclei with a non-null magnetic moment can be investigated using MRI technique and, among these (^{13}C, ^{14}N, ^{19}F, ^{23}Na, ^{31}P), the most popular atom being studied is the hydrogen atom ^{1}H (I=1/2 and $\gamma/2\pi$ = 42.576 MHz/T). In the following sections, only the case of hydrogen nuclei, *i.e.* protons, will be dealt with.

1.2 - Single spin dynamics

According to the classical description of a proton (hydrogen nucleus) in a steady and homogeneous magnetic field $\vec{B}_0$, time evolution of its spin can be described in terms of classical vectors (Rigamonti and Carretta, 2009). In this context, a nuclear magnetic moment $\vec{\mu}$ located in $\vec{B}_0$ precesses at the Larmor frequency ω_L around the direction of $\vec{B}_0$ following the equation:

$$\frac{d\vec{\mu}}{dt} = \gamma\,\vec{\mu} \times \vec{B}_0 \qquad \text{Eq. 1.3}$$

If another magnetic field $\vec{H}_1$, rotating in the plane perpendicular to it, is switched on, then the magnetic moment $\vec{\mu}$ experiences a torque ($\vec{\mu} \times \vec{H}_1$) whose effect is to vary the angle between $\vec{\mu}$ and $\vec{B}_0$. If $\vec{H}_1$ varies with a frequency $\omega \neq \omega_L$ then its effect on the motion of $\vec{\mu}$ is negligible, but if $\omega = \omega_L$, resonance occurs and the magnetic moment precesses around the direction of $\vec{H}_1$. The motion equation of the system in the laboratory frame ($\hat{x}$, $\hat{y}$, $\hat{z}$) is described by the following equation:

$$\frac{d\vec{\mu}}{dt} = \gamma\,\vec{\mu} \times \left[\vec{B}_0 + \vec{H}_1(t)\right] \qquad \text{Eq. 1.4}$$

The time-dependence of $\vec{H}_1(t)$ can be removed considering a frame of reference ($\hat{x}'$, $\hat{y}'$, $\hat{z}'$) rotating with the same angular frequency of $\vec{H}_1$ around the direction of the $\hat{z}$ axis. In this rotating coordinates system $\vec{H}_1$ is static and, supposing it along the $\hat{x}'$ axis, the equation of motion is given by:

$$\frac{d\vec{\mu}}{dt} = \vec{\mu} \times \gamma\left[\left(B_0 - \frac{\omega}{\gamma}\right)\hat{z}' + H_1\,\hat{x}'\right] = \vec{\mu} \times \gamma\vec{H}_e \qquad \text{Eq. 1.5}$$

In the rotating frame, the spin experiences an effective static magnetic field $\vec{H}_e$ and precesses around it (Fig. 1.1). There is resonance for $\omega = \omega_L$ and $\vec{H}_e = \vec{H}_1$ and the precession motion now occurs in the plane $y'z'$.

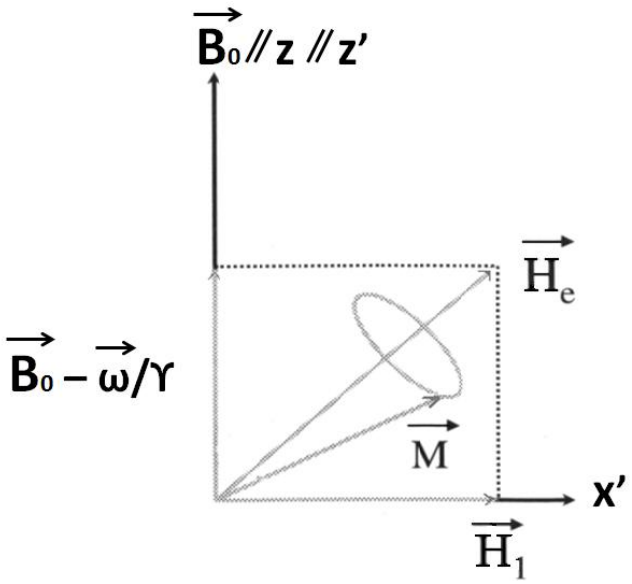

Fig. 1.1: For $\omega = \omega_L$ there is resonance and $\vec{H}_e = \vec{H}_1$. The magnetization $\vec{M}$ precesses around $\vec{H}_e$. [adapted from: Carretta, 2007].

According to quantum mechanics (Andrew, 1955; Abragam, 1961; Slichter, 1990; Rigamonti and Carretta, 2009), when a single proton (I=1/2) is in a steady and homogeneous magnetic field $\vec{B}_0$ applied along the z direction, two different energy levels are created, corresponding to $\mu_z = \pm \gamma\hbar/2$. The energy of these two levels, called Zeeman levels, is:

$$E_{\pm} = -\vec{\mu} \cdot \vec{B}_0 = -\mu_z B_0 = -\gamma I_z B_0 \qquad \text{Eq. 1.6}$$

that implies:

$$E_{+} = -\gamma B_0 \frac{\hbar}{2} \qquad \text{Eq. 1.7a}$$

and

$$E_{-} = +\gamma B_0 \frac{\hbar}{2} \qquad \text{Eq. 1.7b}$$

E_+ and E_- indicate the energy of the proton when μ_z is, respectively, aligned and anti-aligned with the magnetic field $\vec{B}_0$. The energy difference between these levels is:

$$\Delta E = \gamma B_0 \hbar = \hbar\omega_L \qquad \text{Eq. 1.8}$$

where $\omega_L = \gamma B_0$ is called Larmor frequency (Fig. 1.2).

If a photon with energy ΔE interacts with a proton in the energy level E_+, this proton will be excited to the energy level E_-. In other words, transition between Zeeman levels occurs when radiation whose frequency is equal to the energy separation between those levels is applied.

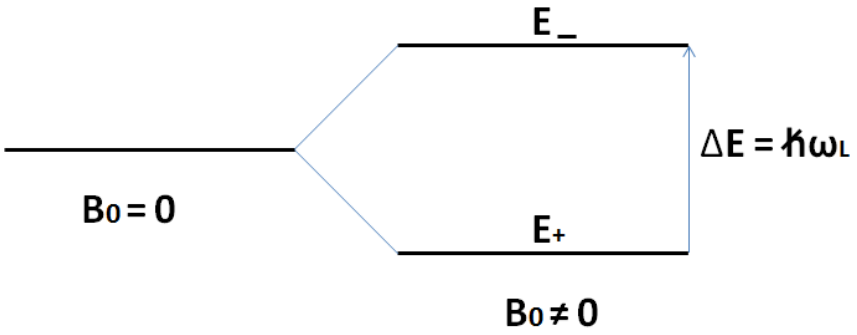

Fig. 1.2: Splitting of the proton energy levels due to the application of the magnetic field $\vec{B}_0$.

Let us now consider the equations of motion for the components of the proton spin $\vec{s}$ when the aforementioned magnetic fields $\vec{B}_0$ and $\vec{H}_1$ are applied. These equations can be obtained, using the time-dependent Schrödinger equation, as expectation values of the spin components. Taking $\vec{B}_0$ along the $\hat{z}$ axis and $\vec{H}_1$ oscillating along the $\hat{x}$ direction, at resonance condition, reversing of $\vec{s}$ with respect to $\vec{B}_0$ occurs.

Using the standard bra-ket notation of the quantum mechanics formalism (Dirac, 1930), any state $|\phi>$ of the spin $\vec{s}$ can be expressed as a linear combination of a state $|\uparrow>$ parallel to the $\hat{z}$ axis and a state $|\downarrow>$ antiparallel to it:

$$|\phi> = c_1 |\uparrow> + c_2|\downarrow> = c_1 \begin{vmatrix}1\\0\end{vmatrix} + c_2 \begin{vmatrix}0\\1\end{vmatrix} = \begin{vmatrix}c_1\\c_2\end{vmatrix} \qquad \text{Eq. 1.9}$$

with $| c_1 |^2 + | c_2 |^2 = 1$, where $| c_1 |^2$ indicates the probability that the spin is aligned along the direction of $\vec{B}_0$ and $| c_2 |^2$ the probability that it is antiparallel to it.

When the magnetic field $\vec{B}_0$ is switched on, the Hamiltonian energy function ***H*** expressing the interaction between the magnetic moment $\vec{\mu}$ and the field can be written as:

$$\boldsymbol{H} = -\vec{\mu} \cdot \vec{B}_0 = \mu_B \vec{s} \cdot \vec{B}_0 \qquad \text{Eq. 1.10}$$

with μ_B indicating the Bohr magneton, and $\vec{s}$ the spin angular momentum that is quantized along the $\hat{z}$ axis.

The Schrödinger equation describing the spin motion:

$$i\hbar \frac{\partial|\phi>}{\partial t} = \boldsymbol{H}\,|\phi> \qquad \text{Eq. 1.11}$$

can be re-written as:

$$i\hbar \begin{vmatrix} \dot{c_1} \\ \dot{c_2} \end{vmatrix} = \mu_B \vec{s} \cdot \vec{B}_0 \begin{vmatrix} c_1 \\ c_2 \end{vmatrix} \qquad \text{Eq. 1.12}$$

that is:

$$i\hbar \begin{vmatrix} \dot{c_1} \\ \dot{c_2} \end{vmatrix} = \hbar\,\omega_L\, s_z \begin{vmatrix} c_1 \\ c_2 \end{vmatrix} \qquad \text{Eq. 1.13}$$

with $\omega_L = \mu_B B_0/\hbar$ indicating the Larmor frequency.

From the eigenvalues of s_z, it follows :

$$i \begin{vmatrix} \dot{c_1} \\ \dot{c_2} \end{vmatrix} = \omega_L \begin{vmatrix} c_1 \\ -c_2 \end{vmatrix} \qquad \text{Eq. 1.14}$$

that yields:

$$\dot{c}_1 = -i\,\omega_L\, c_1 \qquad \text{Eq. 1.15a}$$

$$\dot{c}_2 = i\,\omega_L\, c_2 \qquad \text{Eq. 1.15b}$$

and then:

$$c_1(t) = c_1(t_0)\ e^{-(i\,\omega_L\,t)} \qquad \text{Eq. 1.16a}$$

$$c_2(t) = c_2(t_0)\ e^{+(i\,\omega_L\,t)} \qquad \text{Eq. 1.16b}$$

The expectation values of the components of the spin can now be calculated. Neglecting constant factors and setting the arbitrary initial phase equal to zero, results can be written in the following way:

$$< \phi(t)|\ s\ |\phi(t) > = \left(< s_x >, < s_y >, < s_z > \right) = (\ \cos(\omega_L t),\ \sin(\omega_L t)\ ,\ \cos\theta\ ) \qquad \text{Eq. 1.17}$$

indicating that the components of the spin $\vec{s}$ in the plane xy perpendicular to the direction of the applied magnetic field vary periodically with the Larmor frequency. The component s_z along the direction of $\vec{B}_0$ instead, does not change its value because it's time-independent.

If a magnetic field $\vec{H}_1(t)$:

$$\vec{H}_1(t) = H_0 e^{\pm(i\,\omega_L\,t)} \qquad \text{Eq. 1.18}$$

oscillating in the plane xy is switched on, the expectation values of the spin components could be calculated in a similar way. I report the results that come out from the Schrödinger equation considering the effect of $\vec{H}_1(t)$ on the precessing spin. As done previously, neglecting constant factors and setting the arbitrary initial phase = 0:

$$< \phi(t)|\ s\ |\phi(t) > = \left(< s_x >, < s_y >, < s_z > \right) \qquad \text{Eq. 1.19}$$

$$< s_x > \ = -\ \sin(2\Omega t)\sin(\omega_L t) \qquad \text{Eq. 1.20a}$$

$$< s_y > \; = \sin(2\Omega t)\, \cos(\omega_L t) \qquad \text{Eq. 1.20b}$$

$$< s_z > \; = \; - \sin(2\Omega t) \qquad \text{Eq. 1.20c}$$

with $\Omega = \mu_B H_1/\hbar$. These equations show that the motion of the spin $\vec{s}$ can be explained as resulting from the precession around the $\hat{z}$ axis at the Larmor frequency plus the rotation around the direction of $\vec{H}_1(t)$ at the frequency 2Ω. In the rotating frame of reference $(\hat{x}', \hat{y}', \hat{z}')$ it corresponds to a rotation of $\vec{s}$ by an angle that depends on the duration of the RF pulse (Andrew, 1955; Abragam, 1961; Slichter, 1990; Rigamonti and Carretta, 2009).

1.3 - Dynamics of spins in matter

Let's hereafter consider a hydrogen spins system of N weakly interacting spins, placed in a steady and homogeneous magnetic field $\vec{B}_0$ (Rigamonti and Carretta, 2009).

At thermal equilibrium, attained after a relaxation time T_1, the spins occupy the 2 energy levels corresponding to the different allowed orientations of the nuclear spin $\vec{I}$ (Fig. 1.3). The spin population of each energy level is regulated by the Boltzmann statistics and is proportional to the exponential Boltzmann factor 'exp(-E/K_BT)', where E indicates the energy of the level (see Eq. 1.6), K_B is the Boltzmann constant ($8{,}62 \cdot 10^{-5}$ eV K^{-1}) and T is the temperature (expressed in Kelvin).

The population on each hydrogen energy level can be statistically evaluated as:

$$N_+ = \frac{N}{Z}\; e^{+\frac{\vec{\mu}\cdot\vec{B}_0}{K_B T}} \qquad \text{Eq. 1.21a}$$

$$N_- = \frac{N}{Z}\; e^{-\frac{\vec{\mu}\cdot\vec{B}_0}{K_B T}} \qquad \text{Eq. 1.21b}$$

with:

$$Z = e^{-\frac{\vec{\mu}\cdot\vec{B}_0}{K_B T}} + e^{+\frac{\vec{\mu}\cdot\vec{B}_0}{K_B T}} \qquad \text{Eq. 1.22}$$

N_+ indicates the lower energy level (Eq. 1.21a) corresponding to I_z= +1/2 (N_- with I_z= -1/2 indicates the higher energy level; Eq. 1.21b) and Z in Eq. 1.22 is the partition function, commonly used in statistical mechanics for describing the properties of the system.

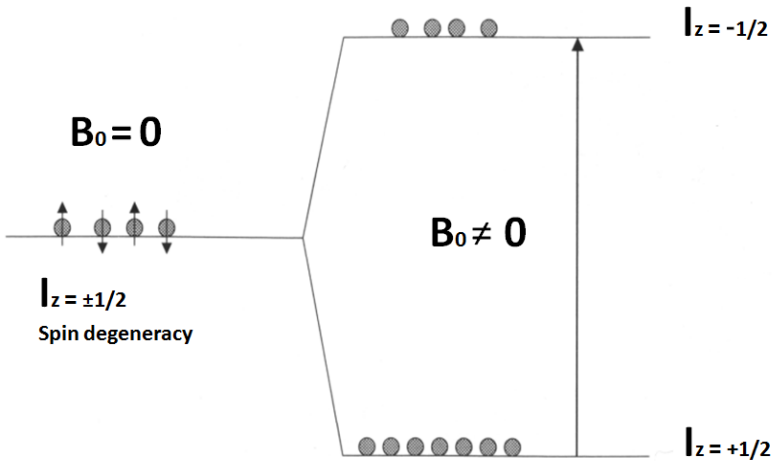

Fig. 1.3: Sketch of the energy levels splitting for a system of hydrogen atoms when the magnetic field $\vec{B}_0$ is applied [adapted from: Rigamonti and Carretta, 2009].

Considering now the spins system placed in the field $\vec{B}_0$, the macroscopic effect of the interaction is a macroscopic magnetic moment $\vec{M}$, not null, aligned along the direction of the applied magnetic field and with intensity M_0 :

$$M_0 = \frac{N\mu^2 B_0}{3K_B T} = N < \mu_z > \qquad \text{Eq. 1.23}$$

with:

$$< \mu_z > = \frac{1}{Z}\,\gamma\,\hbar \sum_{I_z} I_z\, e^{-\frac{(-\gamma\,\hbar\, I_z\, B_0)}{K_B T}} \qquad \text{Eq. 1.24}$$

indicating the average statistical value of the single magnetic moment.

Eventually, it is possible to write:

$$\vec{M} \propto \sum_k \vec{\mu}_k \qquad \text{Eq. 1.25}$$

that allows us to apply the motion equation for single spin (Eqs. 1.3-1.5) to this macroscopic magnetic moment:

$$\frac{d\vec{M}}{dt} = \vec{M} \times \gamma \vec{B}_0 \qquad \text{Eq. 1.26}$$

The previous Eq. 1.26, although falling within classical mechanics, holds in quantum mechanics too due to the fact that the expectation value of any physical observable evolves in time according to the classical equations of motion. The macroscopic magnetization, detected during the MRI scan, represents the expectation value of the magnetic moment of the spins system and this is the reason why the Eq. 1.26 (classical mechanics) can describe its temporal evolution (Rigamonti and Carretta, 2009).

1.4 - Bloch equations and relaxation times (T_1 and T_2)

In a real system, there are two important interactions whose effects cannot be neglected: the spin-spin and the spin-lattice interactions. Let's consider the case in which the magnetization $\vec{M}$ is on the xy plane (due to the application of $\vec{H}_1(t)$) and, once $\vec{H}_1(t)$ is switched off, it is returning aligned to $\vec{B}_0$.

Its components M_x, M_y, M_z evolve in time according to the following Bloch equations, accounting for both the Larmor precession and the motion towards the equilibrium condition (Andrew, 1955; Abragam, 1961; Slichter, 1990):

$$\frac{dM_x}{dt} = \gamma \left(\vec{M} \times \vec{B}_0\right)_x - \frac{M_x}{T_2} \qquad \text{Eq. 1.27a}$$

$$\frac{dM_y}{dt} = \gamma \left(\vec{M} \times \vec{B}_0\right)_y - \frac{M_y}{T_2} \qquad \text{Eq. 1.27b}$$

$$\frac{dM_z}{dt} = \gamma \left(\vec{M} \times \vec{B}_0\right)_z + \frac{M_0 - M_z}{T_1} \qquad \text{Eq. 1.27c}$$

The T_1 constant is called either spin-lattice relaxation time or longitudinal relaxation time and T_2 is called either spin-spin relaxation time or transversal relaxation time. They reflect, on macroscopic scale, the microscopic effects of spin-lattice and spin-spin interactions.

Integrating the Bloch's equations (Eqs. 1.27) we obtain:

$$M_z(t) = M_0 \left(1 - e^{-\frac{t}{T_1}}\right) \qquad \text{Eq. 1.28a}$$

and

$$M_{x,y}(t) = M_0 \, e^{-\frac{t}{T_2}} \qquad \text{Eq. 1.28b}$$

Eq. 1.28a shows that the longitudinal component M_z returns exponentially to equilibrium with characteristic time T_1 (Fig. 1.4a). Eq. 1.28b shows instead that both the transversal components of the magnetization M_x and M_y decay exponentially to zero with characteristic time T_2 (Fig. 1.4b).

Let's discuss now qualitatively the mechanisms underlying the relaxation times T_1 and T_2. The T_1 relaxation time indicates how fast the thermal equilibrium of the whole system is attained, *i.e.* how fast the spins system exchanges its magnetic energy with the lattice (energy associated with the interaction between spins and magnetic field). The value of M_z is related to the population

on the Zeeman levels and any change in M_z corresponds to a re-arrangement of the spins between these levels.

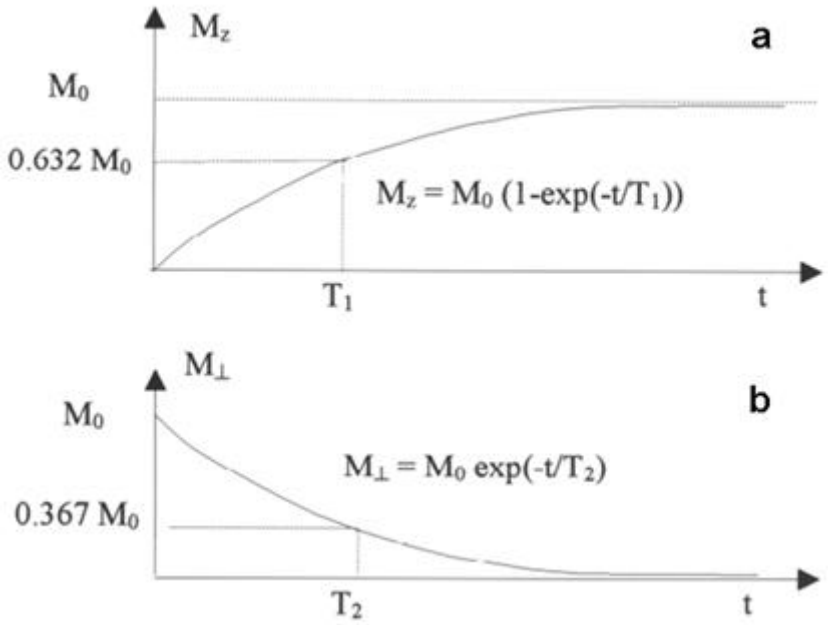

Fig. 1.4: Exponential decay of the longitudinal (a) and transversal (b) components of the magnetization M_0. After a time T_1 the value of the longitudinal component is about 63% of M_0 (a). After a time T_2 the value of the transversal components is about 37% of M_0 (b) [from: Rigamonti and Carretta, 2009].

Such re-arrangement implies that spins change their orientation in the field thus interacting with the surrounding lattice.

The T_2 relaxation time indicates how fast the interaction between spins can dephase their motion. When the magnetic field $\vec{H}_1$ is switched off, the motion of each spin is affected by dipolar interaction with the magnetic moments of the surrounding spins, *i.e.* by a dephasing local magnetic field. A global dephasing of the spins occurs, causing the transversal components $M_{x,y}$ to decay to zero and resulting in the alignment of the magnetization $\vec{M}$ along the direction of $\vec{B}_0$. However, transversal relaxation typically occurs in a time T_2^* shorter than T_2 due to inhomogeneities in the static magnetic field $\vec{B}_0$ mainly caused by: geometrical imperfections of the magnet, perturbation of the magnetic field due to interaction with the sample and possible local field gradients. The relationship between T_2^* and T_2 is expressed by:

$$\frac{1}{T_2^*} = \frac{1}{T_2} + \gamma \Delta B_0 \qquad \text{Eq. 1.29}$$

where $\gamma\Delta B_0$ indicates the frequency range in which the Larmor frequencies of the spins are spread due to field inhomogeneities (Carretta, 2007; Rigamonti and Carretta, 2009).

CHAPTER 2 – SEQUENCES AND PRELIMINARY ASSESSMENT OF ZOOM-EPI TECHNIQUE

Introduction

After having discussed, in the previous chapter, the basic principles of magnetic resonance imaging, in this chapter the main EPI techniques commonly used to perform fMRI studies are briefly discussed and features of the ZOOM-EPI sequence are reported. The ZOOM-EPI sequence is investigated because it is the established sequence for spinal cord diffusion. Features of different image weighting and importance of temporal signal to noise ratio are discussed as well. So far, the ZOOM-EPI sequence using a reduced FOV has never been used to perform fMRI in the spine and for this reason, before applying it in the spine, I opted to test its performance in the brain. In this chapter, a comparison between functional results obtained using ZOOM-EPI with ones obtained using conventional Gradient Echo and Spin Echo EPI sequences is reported. This study is performed in the brain because brain-fMRI is an established technique, used for clinical purposes as well, and the aim of this study is to compare ZOOM-EPI results with 'established' ones.

2.1 - Spin Echo and Gradient Echo sequences

In MRI the decaying signal is not measured immediately after the Radio-Frequency (RF) pulse but it is recovered by refocusing the spreading-out spins with other RF pulses or with magnetic field gradients. The most common sequences used to perform functional scans are Spin-Echo (SE) and Gradient-Echo (GE) Echo Planar Imaging (EPI) sequences. Before discussing EPI technique (see section 2.2), let's introduce SE and GE sequences. The basic SE sequence (Fig. 2.1) is composed by a first $\pi/2$ excitation pulse followed, after a time interval τ, by a second pulse π. The first pulse projects the magnetization into the transverse plane where, due to local field inhomogeneities, the relaxing spins start to dephase (Haacke et al., 1999; Carretta, 2007; Hashemi et al., 2012). The application at the time $\tau = TE/2$ of the π pulse refocuses the spins and, after an interval TE (called Echo Time) from the initial pulse, the magnetization is recovered despite reduced by a factor $\exp(-2\tau/T_2)$ (Fig. 2.2). The π pulse eliminates the dephasing effects due to external magnetic field inhomogeneities and is usually indicated as refocusing or rephasing pulse.

In Fig. 2.1, the timing diagram for SE sequences is depicted, showing the RF pulses, slice-select gradient, phase encoding gradient, frequency encoding (or readout) gradient and echo. The Repetition Time, indicated with TR, is the time between two subsequent $\pi/2$ excitation pulses. During one TR interval, only one phase-encoding step is performed (*i.e.* only one line in the k-space is filled in). The acquisition time of an image instead, is proportional to the number of phase-encoding steps. This statement holds also for GE sequences that are described later in this section. A gradient in the negative direction is applied immediately after the slice selection. Every time a gradient is applied it dephase the spins and thus, after that the slice-select gradient has selected the slice, a negative gradient (opposite direction) must be applied in order to refocus the spins. Moreover, two 'crusher' gradients are applied at each side of the slice slice-select gradient applied during the π pulse in order to achieve more accurate refocusing at time TE. In Fig. 2.1, it is also shown that the frequency encoding gradient has, at the beginning, an initial negative lobe that dephases the spins and that is followed by a positive lobe (gradient reversal) that rephases the spins. If the negative gradient lobe were not applied, the spins would

start to dephase when the frequency encoding gradient is switched on and at the time TE the spins would not be in phase. The application of the negative gradient (dephasing) just before the positive one allows the spins to refocus at the time TE if the area under the negative lobe is half the area under the positive lobe (Fig. 2.3). During data acquisition, the readout gradient rephases the spins in the first half of the readout and then the spins fan out in the second half.

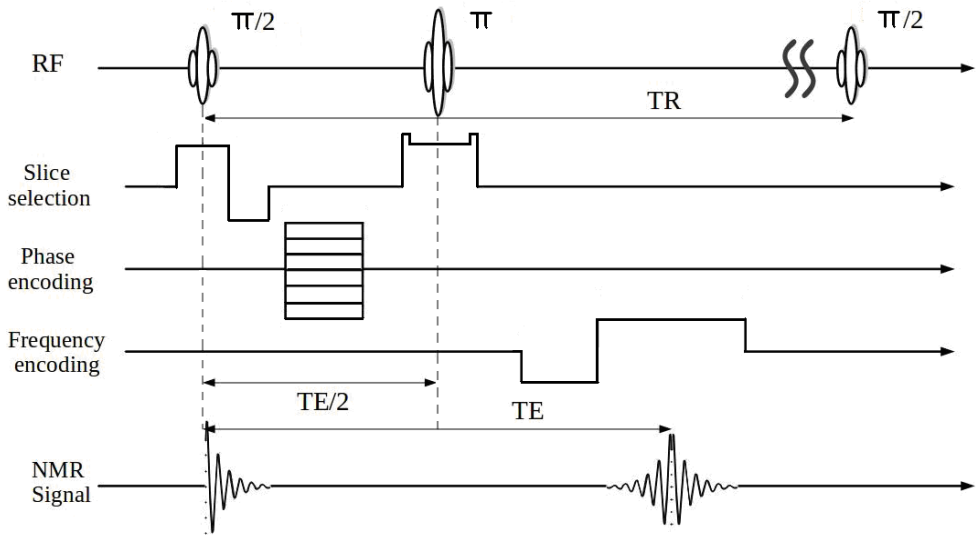

Fig. 2.1: Pulse sequence diagram for SE sequences.

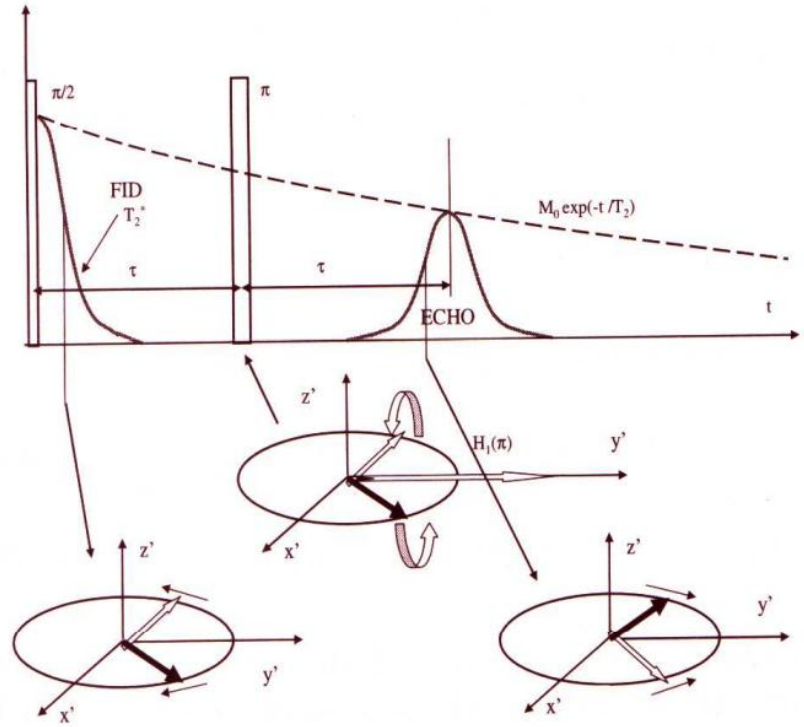

Fig. 2.2: Simplified illustration of the spins motion that generates the echo signal [from: Carretta, 2007].

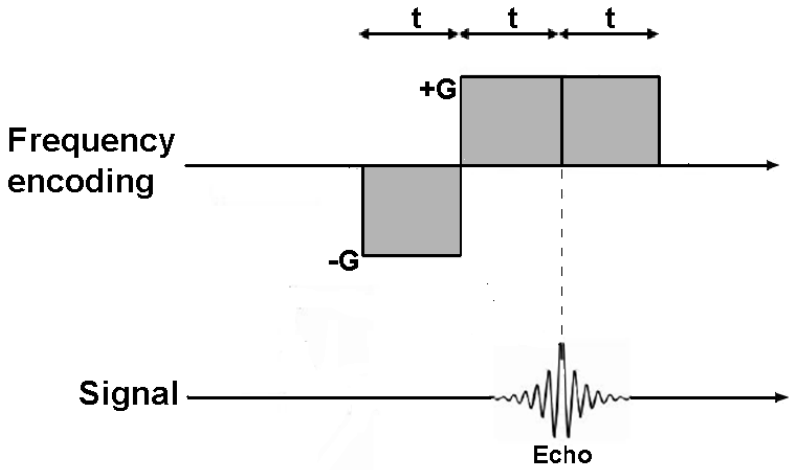

Fig. 2.3: Applying the negative gradient (dephasing) just before the positive one allows the spins to refocus at the time TE (i.e. when the echo is maximum). It is required that the area under the negative lobe is half the area under the positive lobe.

In Fig. 2.4 it is depicted the case of two gradients with the same area, although with different strength and duration, having the same effect on spins. However, the gradient b) has the advantage of being faster, a condition required to perform fast scanning (see section 2.2).

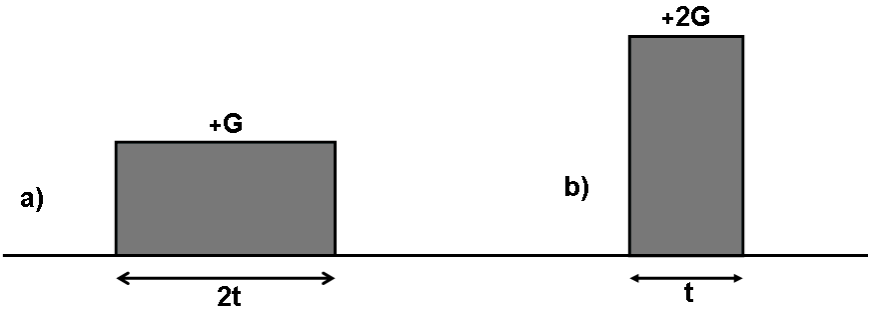

Fig. 2.4: The gradient a) has twice the duration of the gradient b) but half the strength. The two areas (in grey) are identical and identical is their dephasing (or refocusing) effect on spins.

GE sequences differ from SE ones in the way they refocus spins before data acquisition: SE sequences use RF pulses instead GE sequences use gradient reversals (Schmitt et al., 1998; Haacke et al., 1999).

In GE sequences a flip angle smaller than $\pi/2$, causing an incomplete flipping of Mz into the xy plane, is used. In GE imaging, the π refocusing pulse is not used. The signal is dephased and then rephased (or recalled) later using a gradient applied in the readout direction before the frequency encoding (or readout) gradient. The result is to dephase the signal and then recall it at the time TE (Fig. 2.5). As explained above, the area under the negative lobe is half the area

under the positive lobe. Due to lack of the π refocusing pulse, the rate of decay is now given by T_2* instead of T_2.

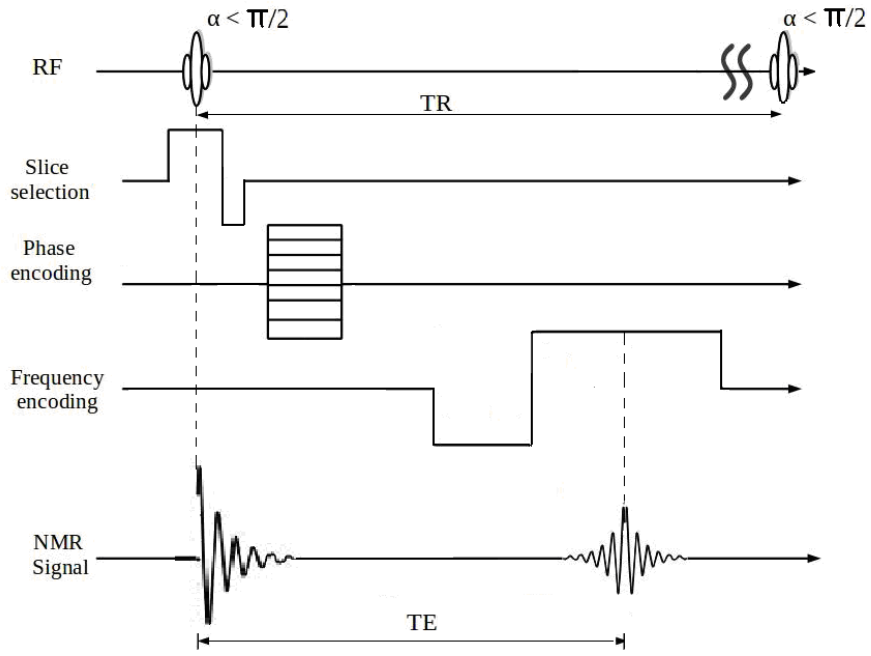

Fig. 2.5: Pulse sequence diagram for GE sequences.

2.2 - Echo Planar Imaging

Echo Planar Imaging (EPI) is particularly suited for functional MRI because it is an ultrafast technique that allows acquiring whole volume images in a few seconds. This is a very important point because fast scanning is required to get a detailed description of neural events that are detected with fMRI. However, the drawback is that EPI sequences are very sensitive to field inhomogeneities and artefacts (Schmitt et al., 1998, Haacke et al., 1999; Hashemi et al., 2012). EPI sequences require high performance gradients, that can be switched on and off very quickly, and advanced hardware allowing fast signal processing. In conventional MRI sequences, a separate RF excitation is required for each data line (each phase encoding step) and thus, as reported in the previous section, the acquisition of an image takes as many TRs as the number of phase encoding steps or lines in the k-space.

In EPI sequences instead, the k-space is covered after a single RF pulse ('shot'). They are called 'single shot EPI' if they fill the k-space in just one shot and 'multishot EPI' if they use multiple excitations. However, this goal is achieved by rapidly reversing the readout gradient from positive to negative for a total of N_y times during a single T_2* decay (lasting around 100msec), with N_y indicating the number of lines in the k-space. The readout gradient has a total of $N_y/2$ positive lobes and $N_y/2$ negative lobes, with each lobe corresponding to a separate k-space line (and thus to a separate phase encoding step).

In Fig. 2.6, the phase-encoding gradient is applied briefly only when the frequency encoding gradient is zero, that is when the k-space position is at either end of the k_x axis (Fig. 2.7). This method is called 'blipped phase encoding'. It is also shown that a series of echoes are produced and each is individually phase encoded (Fig. 2.6), so that the k-space can be covered in a single shot (or multiple shots). The number of echoes produced exploiting a single RF is called 'echo train length'.

Echo Planar Imaging can be applied to both SE and GE sequences. For example, as shown in Fig. 2.6, a $\pi/2$ and a π pulses can be applied before the EPI module, in order to obtain SE contrast.

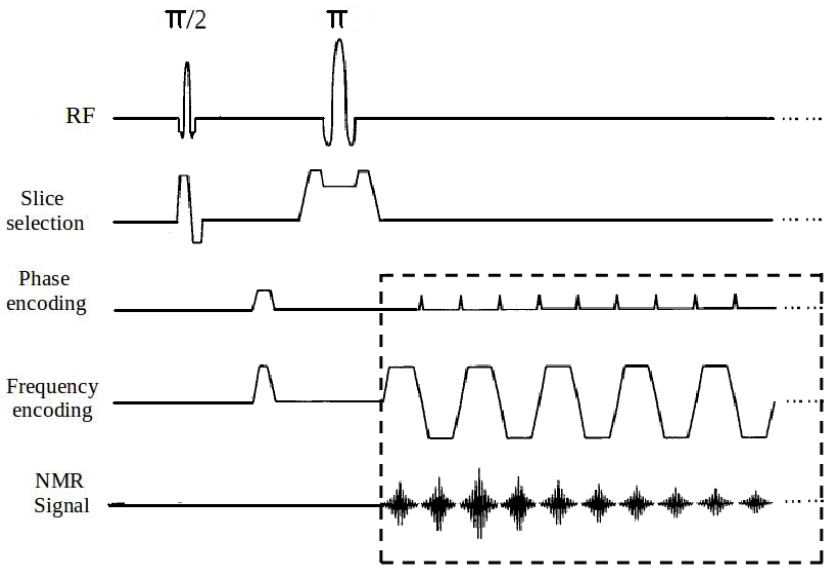

Fig. 2.6: Pulse sequence diagram for a SE EPI sequence. The EPI module is highlighted by the dashed line [adapted from: Bernstein et al., 2004].

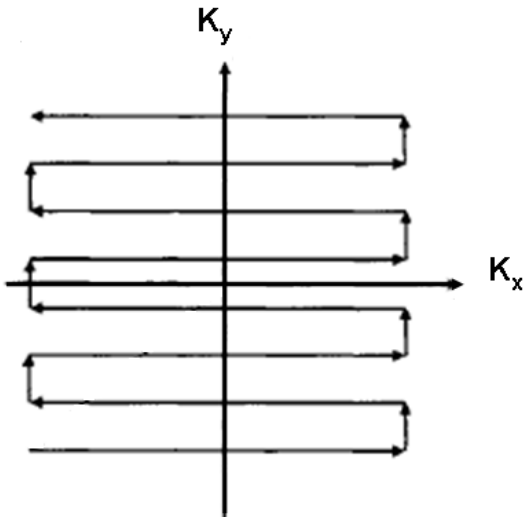

Fig. 2.7: Sketch of the K-space trajectory for blipped EPI. For even echoes the trajectory is the opposite of that for odd echoes [from: Bernstein et al., 2004].

2.3 - Spin Echo ZOOM sequence

All the spinal functional scans in this thesis were performed using the Spin Echo ZOnally-magnified Oblique Multislice EPI (SE-ZOOM-EPI) sequence (Wheeler-Kingshott et al. 2002a, 2002b; Wilm et al., 2009), with a reduced field of view for targeted areas of fMRI activations. A description of the ZOOM sequence follows.

After the $\pi/2$ slice-selective pulse, the π pulse is applied obliquely at an angle β, rather than refocusing the entire plane excited by the $\pi/2$ slice selective pulse (Fig.2.8). A gap is required between the $\pi/2$ excitations to prevent the π pulse from inverting the inner volume of the neighbouring slice. If the distances from isocentre to the centre of the $\pi/2$ slice in the phase and slice directions respectively are y and z, then it can be shown that, to excite the same area, the π pulse must be applied at an offset, d, in the slice direction from isocentre of:

$$d = z\ \sin(\beta)\ -\ y\ \cos(\beta) \qquad \text{Eq. 2.1}$$

The resulting excited parallelogram can be considered as the desired rectangular inner volume (black area in Fig. 2.8) flanked by two triangular regions - the transition bands. Each of these transition bands is signal which would wrap around into the inner volume if the FOV in the phase- encoding direction were to be set equal to the inner volume. Instead, FOV(min), the minimum FOV over which data can be acquired without wrap-around artefacts in the inner volume, is the desired inner volume plus half of each transition band (Symms et al., 2000).

Saturation bands are used to further reduce signal from the transition bands, reducing the size of FOV(min) and decreasing still further the required echo-train length. Tradeoffs can be made between distance to the next slice, size of transition band and inner volume size. A characteristic of ZOOM-EPI is the need for a slice gap between successively acquired slices. Contiguous slices are not possible with this implementation of the ZOOM sequence, but complete coverage can be obtained by separate, spatially interleaved acquisitions. The reduced FOV of our ZOOM-EPI sequence allows high in-plane resolution on axial acquisitions, while maintaining a short EPI echo train that results in a reduction of susceptibility-induced artefacts.

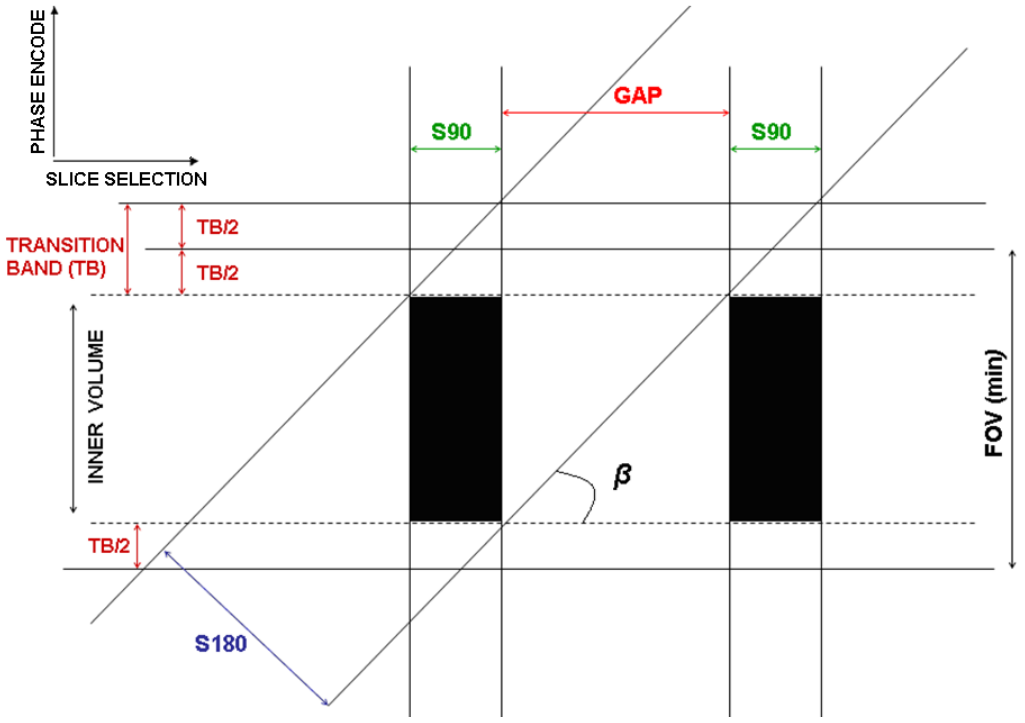

Fig. 2.8: Schematic sketch of the multislice ZOOM sequence. S90 (in green) represents the $\pi/2$ excitation pulse slice thickness and S180 (in blue) the refocusing pulse slice thickness. The gap between acquired slices is indicated with GAP (in red) [adapted from: Wheeler-Kingshott et al., 2002a].

2.4 - T_1, T_2 and PD –weighted images

The contrast of an image depends on both the TE and the TR used in the sequence.

Each tissue is characterized by its own relaxation times and by hydrogen spin density ρ(H). The higher the number of spins per unit volume, the higher the signal that can be detected. Considering that each spin gives the same contribution to M_0 (*i.e.* spin density is proportional to the magnetization) and that time evolution of the components of the magnetization drives the signal intensity, it can be written (Hashemi et al., 2012):

$$S = \rho(H)\left(e^{-\frac{TE}{T_2^*}}\right)\left(1 - e^{-\frac{TR}{T_1}}\right) \qquad \text{Eq. 2.2}$$

The intensity (or contrast) of a tissue can be changed using different TRs and TEs in the sequence according to which kind of 'weighting' we are interested in.

From Eq. 2.2, it follows that:

1- Proton density-weighted (PD-weighted) images can be obtained using a long TR (compared with T_1) and TE as short as possible. Signal dependence from the number of spins per volume unit is strong and the signal only slightly depends on relaxation times;

2- T_1-weighted images have short TR (usually less than $T_1/2$) and TE as short as possible. Signal-dependence from T_1 is strong.

3- T_2-weighted images are featured by long TR (compared with T_1) and long TE (TE ≈ T_2). Signal dependence from T_2 is strong.

2.5 - Temporal signal to noise ratio

Dealing with functional MRI, it is important to aim at obtaining a temporal signal to noise ratio (TSNR) as high as possible because it is an indicator of sensitivity: the higher the TSNR the higher the sensitivity for detecting signal change.

As reported by Murphy et al. (2007), TSNR is defined as:

$$\mathrm{TSNR} = \frac{\mu}{\sigma} = \frac{\mu}{\sqrt{\frac{1}{N}\sum_{k=1}^{N}(x_k - \mu)^2}} \qquad \text{Eq. 2.3}$$

where μ is the mean of the time series, σ is its standard deviation, N is the number of time points and x_k is the measured signal in a voxel.

The theoretical relationship between TSNR and number of time points N needed to detect the size effect Eff (Fig. 2.9) is expressed by the formula (Murphy et al., 2007):

$$N = \frac{2}{R(1-R)}\left[\frac{\mathrm{erfc}^{-1}(\alpha)}{(\mathrm{TSNR})\cdot(\mathrm{Eff})}\right]^2 \qquad \text{Eq. 2.4}$$

where '$\mathrm{erfc}^{-1}(\alpha)$' is the inverse of the complementary error function (that can be calculated using the dedicated MATLAB function 'erfcinv') having as argument the p-value used in the statistics. The letter R stands for the ratio between the number of volumes of stimulation and the total number of volumes acquired during the whole fMRI session. Nevertheless, this theoretical estimation is likely to be conservative, as found in previous results (Cohen-Adad et al., 2010).

Referring to Eq. 2.3 and Eq. 2.4:

1- TSNR is usually calculated during a resting state scan and the lower the signal variance throughout the time series the higher the TSNR (Eq. 2.3). TSNR is strictly related to physiological noise, whose effect is to cause signal fluctuations reducing the TSNR. If physiological noise is smaller, a smaller number of time points (Eq. 2.4) is required to

detect signal changes that are likely to be due to neuronal activity.

2- After choosing a target size effect, Eq. 2.4 can be used to perform power analysis for calculating the number of volumes required to detect that very size effect. The critical role of TSNR for determining success of an experiment is evident (Eq. 2.4).

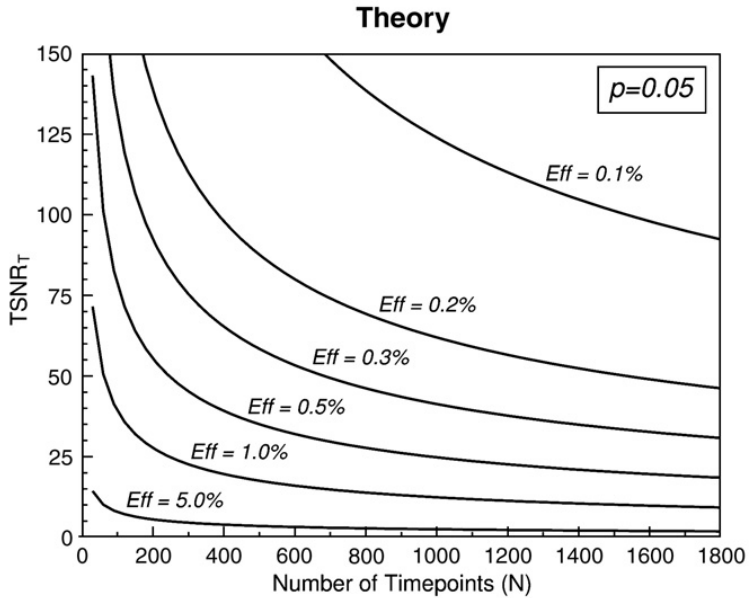

Fig. 2.9: Theoretical relationship between TSNR and number of volumes N for different effect sizes using the threshold p = 0.05 [from: Murphy et al., 2007].

Signal-to-noise ratio (SNR) instead, represents the strength of the single image signal over the noise in the absence of signal and does not give any information about either stability of the images throughout the scanning session or the temporal noise features.

SNR of an MRI image is defined as:

$$\mathrm{SNR} = \frac{S}{\sigma_t} \qquad \text{Eq. 2.5}$$

with S being the mean image signal intensity and σ_t the thermal component of the noise.

Theoretically, SNR could be made very high by enhancing the voxel size, but it would not improve sensitivity whether physiological noise is dominating the signal variance. Moreover, using large voxels would lead to too pronounced partial volume effects (PVE) (Weibull et al.,

2008). As reported in previous studies (Kruger and Glover, 2001; Bodurka et al., 2005; Triantafyllou et al., 2005), the physiological contribution to the noise is proportional to the voxel size and there is a threshold upon which a further gain in TSNR is limited by physiological noise, regardless of the SNR increase:

$$\mathrm{TSNR} = \frac{\mathrm{SNR}}{\sqrt{1 + \lambda^2 \cdot \mathrm{SNR}^2}} \qquad \text{Eq. 2.6}$$

Eq. 2.6 is plotted in Fig. 2.10 and shows that TSNR reaches a plateau with asymptotic limit $1/\lambda$, that depends on the tissue being imaged (Triantafyllou et al., 2005) but not on the magnetic field used (Krueger et al., 2001; Triantafyllou et al., 2005). The value of λ has been evaluated in the brain empirically and resulted: λ=0.011 for GM, λ=0.006 for WM (Kruger and Glover, 2001) and λ=0.021 for CSF (Bodurka et al., 2005). However, at small voxel size, where physiological noise is smaller, the relationship between TSNR and SNR is quite linear and thus an increase in SNR using a higher magnetic field would substantially translate to higher sensitivity to detect signal changes, without PVE drawbacks (Triantafyllou et al., 2005). For a given scanner hardware and using high spatial resolution, the only way to further increase statistical power is to acquire a higher number of volumes (Eq. 2.4).

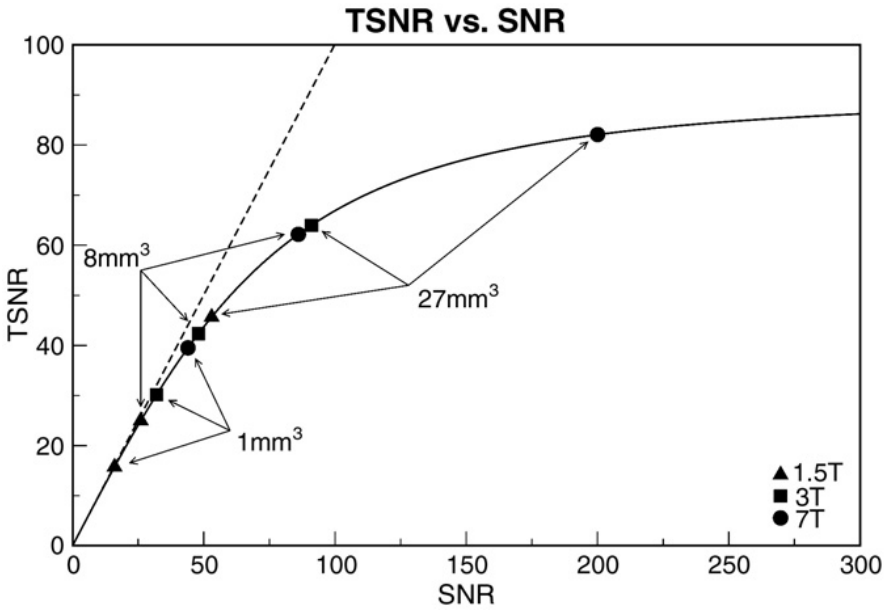

Fig. 2.10: Relationship between TSNR and SNR in grey matter using 1.5T, 3T and 7T scanners for voxel sizes of 1×1×1mm^3, 2×2×2 mm^3 and 3×3×3 mm^3. The dashed line indicates this relationship in the absence of physiological noise [from: Murphy et al., 2007].

2.6 - Brain fMRI: preliminary validation of SE-ZOOM-EPI sequence for fMRI purposes

2.6.1 - Purpose

The purpose of this study was to check the location of activations in the brain using SE-ZOOM EPI sequence. Functional activations in the brain detected using 3 different EPI sequences (GE, SE, SE-ZOOM) are studied.

2.6.2 - Materials and Methods

Subjects – For this study 5 healthy subjects (mean age 30±5 yrs, all right handed) were scanned.

Imaging parameters – All scans were performed using a 3T MRI scanner (Philips Healthcare, Best, Netherlands) with a 32-channel head coil, studying the functional activity in the motor areas of the brain with a finger-tapping task (right hand) at 1Hz speed. The block design comprised 6 alternating epochs of rest and movement, each lasting 18 seconds, for a total of 84 volumes. For each subject we performed the three EPI sequences: GE, SE and SE-ZOOM. The imaging parameters for the GE and SE sequences were: 30 slices per volume, TR=3000ms, TE=30ms, voxel size=1.15x1.17x5mm^3 (reconstructed to 0.96x0.96x5 mm^3), FOV=180x245mm^2, image matrix=156x209. The imaging parameters for the SE-ZOOM sequence were: 9 slices per volume, TR=3000ms, TE=30ms, voxel size=0.94x0.97x5mm^3 (reconstructed to 0.79x0.79x5mm^3), FOV=60x75mm^2, image matrix=64x77. GE and SE were acquired with identical geometrical planning by aligning the axial-oblique slices with the anterior commissural – posterior commissural (ACPC) line. The SE-ZOOM slices were always centred axially around the typical motor areas, with the centre shifted by 30 mm along the X axis and 40 mm along the Z axis from the centre of the ACPC line (Fig. 2.11).

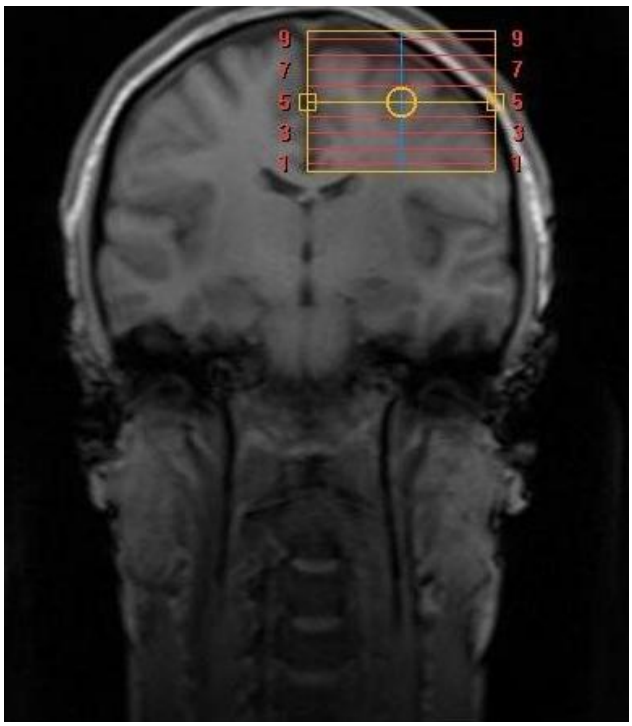

Fig. 2.11: Screenshot of the positioning of the 9 slices for SE-ZOOM sequence.

fMRI analysis – Data were analysed using SPM8 software and statistical maps were obtained after standard geometrical analysis that included slice-timing, realignment and smoothing by three times the dimensions of the voxel with Gaussian kernel. The GE and SE acquisitions were also co-registered, and the corresponding activation maps overlaid using FSLview software for localization comparison. Given the partial brain coverage of the SE-ZOOM sequence, slice correspondence between GE, SE and SE-ZOOM images was visually assessed based on anatomical landmarks. Only the activations with a p-value<0.05 and cluster extent of 20 voxels were accepted.

TSNR calculation – The TSNR for each sequence was calculated with MATLAB, for a resting-state scan of one of the subjects, as the ratio between the mean time course signal throughout the voxel time-series and its standard deviation (Eq. 2.3). Results were obtained considering a sample of 10 voxels deemed within the grey matter.

2.6.3 - Results

For all subjects SE-ZOOM activations were detected in the motor cortex areas and demonstrated good anatomical correspondence with the overlapping activated areas from the more conventional GE and SE sequences (Fig. 2.12). For all subjects the SE-ZOOM showed more localized activation than the other two sequences but with a smaller voxel extent (Table. 2.1). The regions of activation detected by SE-ZOOM remain always smaller than ones detected with both GE and SE.

The TSNR calculated was (mean+/-std): 59.5+/-8.2 for GE, 49.3+/-6.1 for SE and 31.7+/-4.2 for SE-ZOOM.

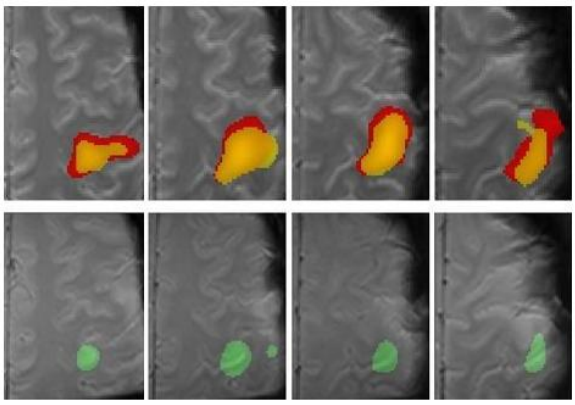

Fig. 2.12: Activations obtained using GE (top in red), SE (top in yellow) and SE-ZOOM sequences (bottom in green) in one subject.

	GE-EPI	SE-EPI	ZOOM-EPI
Subject 1	10555	6862	2963
Subject 2	8847	6929	1495
Subject 3	10085	11780	2015
Subject 4	8335	6357	5626
Subject 5	10387	5422	3050

Table 2.1: Dimensions in mm^3 of the activated motor cortex areas in all subjects using the three different sequences.

2.6.4 - Conclusion and Discussion

Looking at Fig. 2.12, it might seem that SE-ZOOM has got a higher specificity to BOLD but this observation should be carefully examined. The voxel dimensions used for SE-ZOOM were smaller than ones used for GE and SE. We have to consider that higher resolution functional images might appear more localized because of smaller statistically significant areas and not of higher sensitivity. GE sequence has higher TSNR than both SE and SE-ZOOM. However, TSNR decreases using smaller voxels due to a reduction in SNR (see Eq. 2.6) that is proportional to the voxel volume (Triantafyllou et al., 2005). Considering the difference in voxel volume between the SE and SE-ZOOM acquisitions (the ratio is about 1.5), we can conclude that TSNR is comparable between the two sequences. However, a higher number of repetitions are needed to obtain a better signal averaging if smaller voxels are used.

To conclude, this preliminary study confirmed the reliability of SE-ZOOM sequence using a reduced FOV for fMRI purposes.

2.7 - Voxel Size

In spinal fMRI high spatial resolution is required in order to limit partial volume effects (PVE) but using too small voxels doesn't allow to get enough signal. The voxel size used in the experiments included in this thesis, was a trade off between spinal dimensions and required signal and TSNR. Slice thickness of 4 mm was used in order to achieve an adequate amount of signal while allowing a high in-plane resolution of 1.19x1.19 mm^2, suitable for spinal cord studies. The in-plane resolution was enough to discriminate between different tissue types, although the laminated structure of the spinal cord could not be discerned.

Earlier report by Hyde et al. (2001) states that in the brain it would be preferable to use cubic voxels because cortical grey matter exhibits conspicuous tortuosity, and it seems axiomatic that PVE in fMRI can only be minimized by cubic voxels.

For the spinal cord instead, this issue is not a major concern due to the fact that spinal structure is more regular and less variable than other brain structures, e.g. the cortical surfaces (Maieron et al., 2007).

2.8 - Imaging parameters

All spinal data included in this thesis were acquired with a 3T MRI scanner (Philips Achieva TX, Best, Netherlands) using a 16 channel neurovascular coil.

In this section I report the imaging parameters that were used to perform all the spinal functional studies presented in this thesis. Details concerning paradigm, stimulus delivery and slice prescription instead were not consistent between experiments and thus this information is provided later in the specific chapters.

The chosen imaging parameters were:

- TR=3600ms
- TE=30ms
- voxel size=1.19x1.19x4mm^3 with 1mm gap between slices (reconstructed to 1.19x1.19x5mm^3)
- FOV=76x48 mm^2
- acquisition matrix=64x40
- 9 slices
- 200 volumes
- 5 dummy scans

For spinal fMRI scans, a block design was always used and comprised 10 rest epochs alternating with 10 stimulus epochs, each lasting 36 seconds.

The acquisition time was 12:22 min.

CHAPTER 3 – FUNCTIONAL MRI IN THE SPINAL CORD

Introduction

In the previous chapter the ZOOM sequence was tested in the brain and results confirmed its reliability for fMRI purposes.

Before applying it in the spinal cord, let us discuss in depth the metabolic changes that underlie signal changes detected during a functional exam. In this chapter, after an anatomical description of the spinal cord, the BOLD and SEEP effects are introduced and put in context within a wide literature review.

3.1 - The spinal cord and its structure

The spinal cord (SC) and the brain constitute the central nervous system (CNS). The spinal cord connects the brain to the nerves throughout the body and allows the transmission of neural signals. It is located in the vertebral canal and spans from the base of the skull to the upper part of the lower back. It is surrounded by cerebrospinal fluid (CSF) and is protected by the vertebrae, their ligaments and membranes. It has a segmented structure and can be divided into 31 segments, each one characterized by a pair of spinal nerves entering the SC from each side. Its internal structure shows little indication of segmentation and is similar for all segments. From a spinal section it is possible to discern the grey matter (GM), featured by a butterfly or an 'H' outline, surrounded by the white matter (WM). In the centre of the SC there is a small canal containing CSF. The GM is right/left symmetrical and has two posterior horns (PHs), also called dorsal horns, two anterior horns (AHs), also called ventral horns, and an intermediate zone. The PHs are mainly constituted of sensory neurons and the AHs of motor neurons (mainly). Motor neurons receive neural information from the brain and cause muscle to contract, sensory neurons instead, send to the brain neural information concerning stimuli from sensory organs. Other neurons, called interneurons, play an important role in local circuitry, connecting together different neurons within the SC. The neuron is a type of cell specialized in transmitting neural information and made up of a cell body (that includes the nucleus), several dendrites and a long axon. The dendrites are short branches that enter the cell body and receive neural information (electrical impulses) from other neurons. The axon is a single long branch that transmits neural signal to other neurons or muscles and is featured by myelin coating. The GM substance mainly comprises cell bodies, and WM is mainly composed of myelinated axon tracts. The WM contains the ascending (also called afferent) and descending (also called efferent) tracts that carry neural signal either up or down the SC (Standring et al., 2005). Moreover, there are glial cells (another class of cells) surrounding neurons, giving them physical support and specialized in supplying them with oxygen and nutrients. According to somatotopy (Standring et al., 2005), there is correspondence between receptors in an area of the body, usually indicated as 'dermatome', and a specific level of the SC that supply that

dermatome (Fig. 3.1 and Fig. 3.2). The great majority of spinal functional studies focus on the cervical enlargement (Fig. 3.2) that corresponds to the attachments of the nerves supplying the upper limbs and this is the spinal region that has been investigated in this thesis.

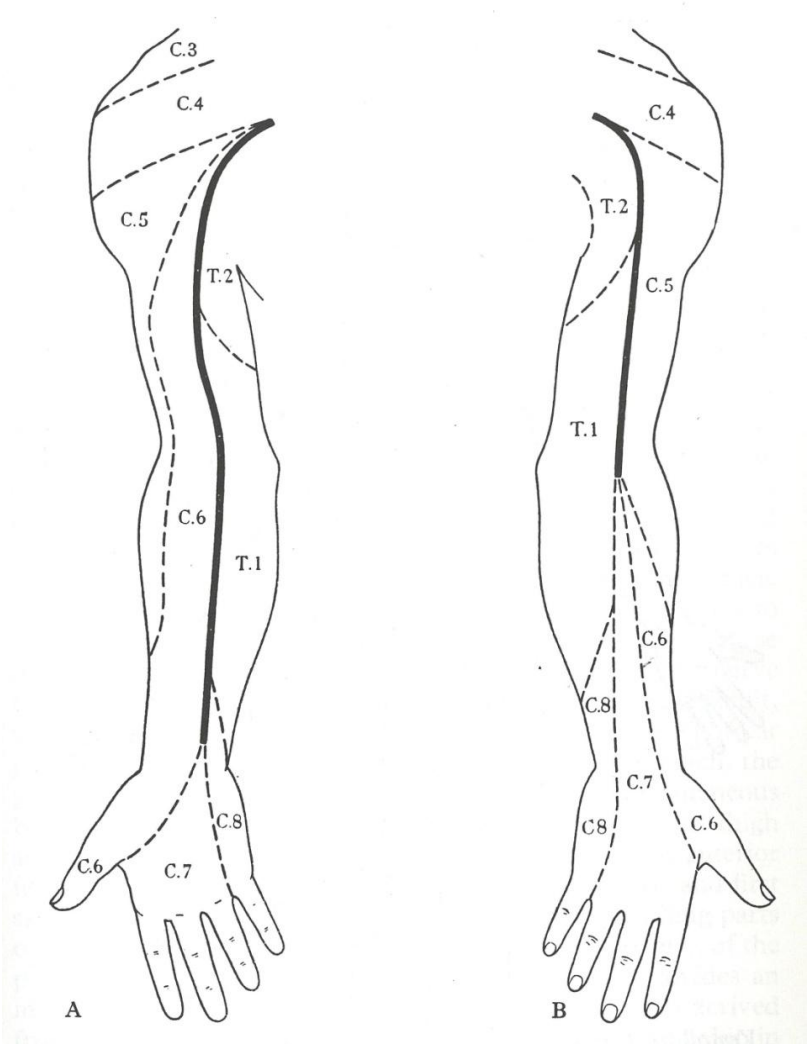

Fig. 3.1: Arrangement of the dermatomes on the anterior (A) and posterior (B) aspect of the upper limbs [from: Standring et al., 2005].

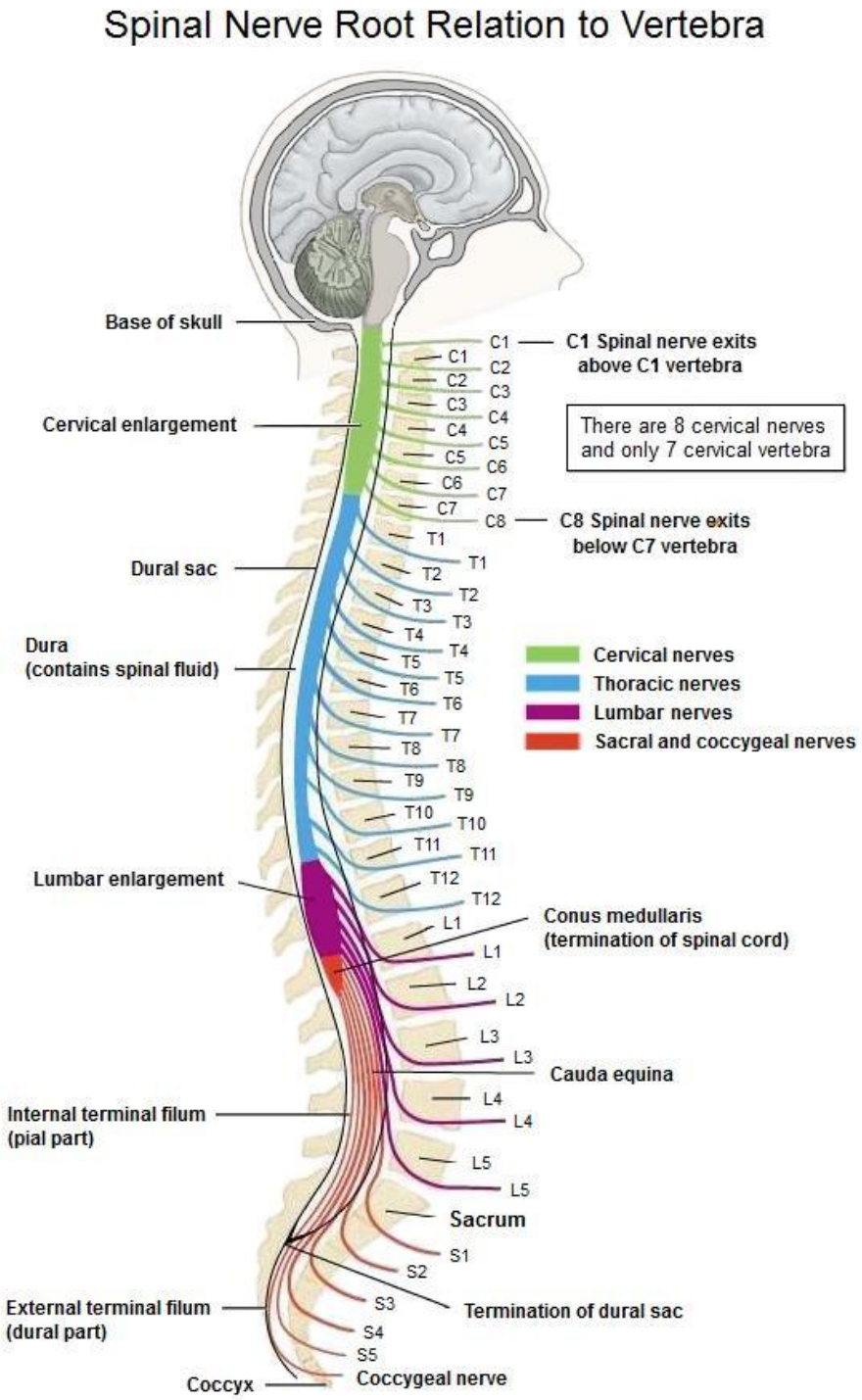

Fig. 3.2: Correspondence between spinal nerves and vertebrae [from: http://www.my-ms.org/].

3.2 - Spinal vasculature

It is important to bear in mind that functional MRI is an indirect measurement of neural activity and it does not represent an absolute measure of metabolic changes, due to the fact that it strongly depends on blood flow, blood volume and oxygenation.

Before introducing in detail the mechanisms that underlie the signal changes investigated with fMRI, let us briefly depict the spinal cord vasculature. The SC contains a network of several and different blood vessels (Fig. 3.3). The network of superficial vessels that supply the spinal cord is made up of arteries, about 0.1 to 0.2 mm in diameter, that run parallel to the axis of the cord. These arteries are connected and form side branches that go through into the spinal cord. The median fissure, dividing left and right hemicords, also contains small arteries. The vessels penetrating deep inside the SC are smaller, with diameters of less than 50 μm. Within the medulla of the cord, veins are mostly radial, have diameters of less than 50 μm and take blood from these small vessels into larger vessels lying at the cord surface and in the anterior median fissure (Thron, 1988).

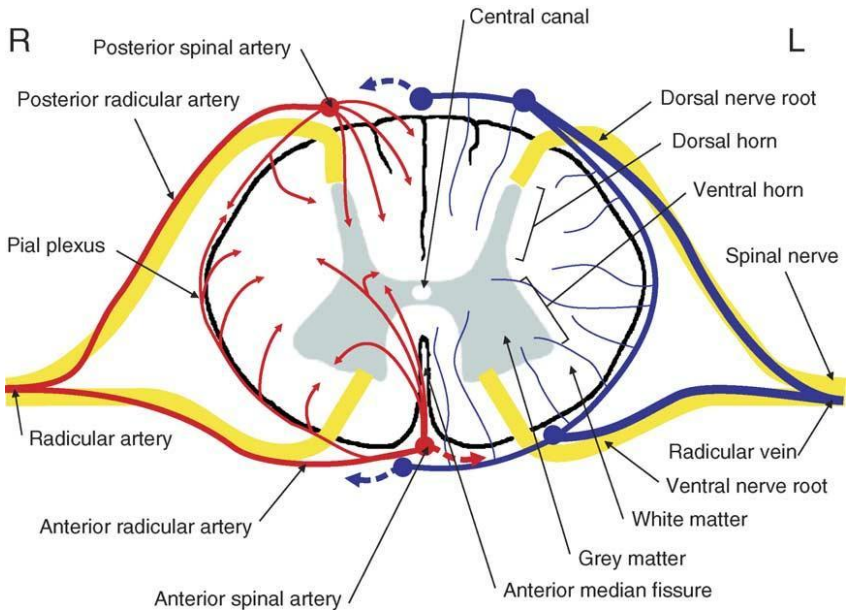

Fig. 3.3: For clarity reasons, veins are drawn only on the left side of the cord, arteries only on the right [from: Giove et al., 2004].

3.3 - BOLD effect mechanism

In 1990 Ogawa et colleagues (Ogawa et al., 1990a; 1990b; 1990c) published three pioneering studies on rats in which it was shown that detection of neuronal activity was possible by measuring change in the MRI signal (T_2* changes) due to change in deoxyhaemoglobin concentration of cerebral vessels. This effect was called BOLD contrast (Blood Oxygen Level-Dependent).

Two years later, three independent research groups tested feasibility and reliability of the BOLD technique translating it from anaesthetized rats to awake humans and results demonstrated task-related changes in the BOLD contrast (Bandettini et al, 1992; Kwong et al., 1992; Ogawa et al., 1992) in the brain of all subjects. BOLD-contrast imaging, also called susceptibility-weighted functional MRI or, more commonly, functional MRI (fMRI), is currently a mainstay of neuroscience. Thousands of papers applying fMRI technique to investigate functional changes in vivo in a non-invasive way have been published ever since, although the complexity of the exact relationship between BOLD signal and the related neural activity is still a debated issue (Logothetis, 2008; Ekstrom, 2010; Kim and Ogawa, 2012).

However, the BOLD theory relies on the following tenets:

1- **Metabolic changes, due to neural activity in response to an applied stimulus, give rise to an alteration of signal at voxel level that can be detected.**

2- **Specific functions are localized at different areas of the brain and can be mapped at high spatial resolution exploiting the stimulus-induced signal change.**

The BOLD effect is related to a mismatch between an increase in local blood flow and an enhancement of oxygen consumption subsequent to neuronal firing. The haemodynamic response can be described as comprising three phases (Logothetis, 2008; Ekstrom, 2010; Kim and Ogawa, 2012). At the beginning there is a small decrease in image intensity called ‘initial dip’ due to the initial consumption of oxygen (immediately after neuronal activation) that is

followed by a large increase of signal intensity (the oversupply of oxygen is only partially balanced by an increase of deoxygenated blood) and finally there is an 'undershoot', that is a decrease of BOLD response before it slowly returns back to baseline (the blood volume takes still a little time to go back to normality after the oversupply of oxygen has ceased). The physical/chemical origin of the BOLD response can be explained in terms of magnetic properties of deoxygenated and oxygenated blood. Oxyhaemoglobin (Hb) contained in oxygenated blood is diamagnetic, like water, and doesn't affect the surrounding magnetic field. On the contrary, deoxyhaemoglobin (dHb) is paramagnetic and causes a clearly measurable changing in the magnetic field reflected in a T_2* reduction in the MRI signal.

Inside a macromolecule of dHb there is iron (Fe2+) in a paramagnetic high-spin state (S = 2), due to the fact that four of its six outer electrons are not coupled, and the global effect is to make dHb a paramagnetic indogenous contrast. When dHb combines with oxygen, iron receives electrons that switch it to a low spin state (S = 0) that make Hb diamagnetic (Pauling and Coryell, 1936). Neuronal activity elicits a reduction in dHb concentration in the venous blood in the surroundings of the activated areas. Due to dHb paramagnetic properties, its reduction corresponds to a smaller distortion of the local magnetic field, resulting in a slower dephasing of local protons. As a consequence of that, there is an increase in T_2* that means higher T_2-weighted MR signal. In the next paragraph the haemodynamic-metabolic changes underpinning the signal enhancement are commented in detail and, furthermore, it is discussed how BOLD effect is driven by a non-intuitive decrease of dHb concentration in the activated areas.

3.4 - Metabolic response to neural activity

As stated in the previous paragraph, the physiological basis of the BOLD effect relies on an uncoupling between local increase of blood flow and oxygen consumption due to neural firing. The oxygen extraction fraction (OEF) is the ratio of oxygen consumed to oxygen delivered by

flowing blood. During resting state OEF does not vary, but if it was constant even during neural activation it wouldn't be possible to detect the BOLD signal (Raichle et al., 2001).

Since the 1980s, experiments in the brain performed using positron emission tomography (PET) confirmed that during resting state the values of cerebral blood flow (CBF, that is also called perfusion, indicates the millilitres of blood that are delivered to each gram of tissue in a second) and of metabolic rate of oxygen consumption ($CMRO_2$, that indicates the number of moles of oxygen consumed per gram of tissue per second) are proportional to each other. During neural activity instead, there is a mismatch between flow and oxidative metabolism (Fox and Raichle, 1986). Fick's principle, relying on the conservation of mass, states that the oxygen consumption of the body is given by the rate of blood flow through the lungs multiplied by the difference in oxygen concentration between arterial and venous blood. Applying the Fick's principle to the spine, $CMRO_2$ and CBF are connected by the following formula (Tofts, 2005):

$$CMRO_2 = Y_A\,[CBF \times 4(Hb^{TOT})] - Y_V\,[CBF \times 4(Hb^{TOT})] = (Y_A - Y_V)\,[CBF \times 4(Hb^{TOT})] \qquad \text{Eq. 3.1}$$

$CMRO_2$ is given by the blood flow multiplied by the total (oxygenated plus deoxygenated) concentration of haemoglobin (Hb^{TOT}, measured in moles per millilitre of blood) and by the difference between the oxygen saturation levels for arterial (Y_A) and venous (Y_V) blood. With oxygen saturation is meant the percentage of haemoglobin molecules that are in the oxygenated state. The factor 4 in the previous formula (Eq. 3.1) takes into account the fact that each haemoglobin molecule can transport 4 oxygen molecules. As reported by Tofts (2005), during resting state (in the brain): $Y_A \approx 1$ and $Y_A \approx 0.6$. The difference $(Y_A - Y_V) = (1 - Y_V)$ represents the oxygen extraction fraction (OEF). The Fick's principle yields important information about physiological change in CBF or blood oxygenation once that Hb^{TOT} and Y_A are constant.

Differentiating equation (Eq. 3.1) it results (Tofts, 2005):

$$\frac{\Delta CMRO_2}{CMRO_2} = \frac{\Delta CBF}{CBF} - \frac{\Delta Y_V}{1 - Y_V} = \frac{\Delta CBF}{CBF} + \frac{\Delta OEF}{OEF} \qquad \text{Eq. 3.2}$$

During neural activation an increase of $CMRO_2$ occurs together with an increase of CBF and a decrease of OEF (that is Y_V has increased). The increase of the oxygenation level of the venous blood is the effect detected by BOLD functional technique. Similar calculations are performed by Kim and Ogawa (2012) as well. Fox and Raichle (1986) reported, during a somatosensory task, an increase in CBF (and glucose consumption) of about 30% and an increase of only 5% in oxygen consumption in the brain. Studies performed on animals assessed as well significant localized haemodynamic-metabolic changes in the spinal cord elicited by stimulation (Marcus et al., 1977; Sasaki et al., 2002; Brieu et al., 2010).

A hypothesis to explain this uncoupling between blood flow and oxygen metabolism was suggested by Buxton and Frank (1997) that proposed a model in which a large flow enhancement is needed in order to create an oxygen concentration gradient between capillaries and mitochondria that finally leads to an increase in oxygen flux from capillaries to neurons.

Buxton and Frank (1997) derived the following formula relating OEF and CBF:

$$\mathrm{OEF} = 1 - (1 - \mathrm{OEF}_0)^{\mathrm{CBF}_0/\mathrm{CBF}} \qquad \text{Eq. 3.3}$$

where CBF_0 and OEF_0 stand for the resting values, while CBF and OEF for the values during activation. Assuming that Hb^{TOT} and Y_A don't vary and substituting Eq. 3.3 into Fick's equation, it yields:

$$\frac{\mathrm{CMRO}_2}{\mathrm{CMRO}_2|_0} = \frac{\mathrm{CBF}}{\mathrm{CBF}_0} \cdot \frac{1 - (1 - \mathrm{OEF}_0)^{\mathrm{CBF}_0/\mathrm{CBF}}}{\mathrm{OEF}_0} \qquad \text{Eq. 3.4}$$

Eq. 3.4, that is plotted in Fig. 3.4, shows that a large flow increase is required in order to allow a little increase in oxygen metabolism. Although this model is a simplified version of what really happens, it is useful to explain the changes in blood flow and oxygen consumption that give rise to the BOLD effect. It is worth pointing out once more that, although in the original papers the mechanisms underlying the BOLD response referred to the brain, those very same mechanisms are valid in the spine as well. Notwithstanding the literature about spinal cord blood flow

(SCBF) is extremely limited compared with CBF, since the BOLD contrast depends on changes in blood flow and on magnetic properties of haemoglobin, the method is applicable both to brain and spinal cord (Yoshizawa et al.; 1996).

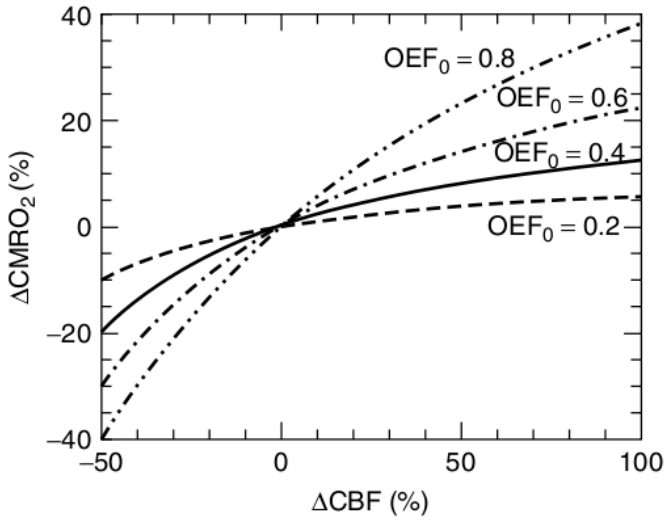

Fig. 3.4: Percentage change in oxygen metabolism vs the required percentage change in cerebral blood flow for a variety of resting oxygen extraction fraction values [from: Tofts, 2005].

3.5 - Anomalies in the spinal BOLD effect: SEEP effect

According to results obtained stimulating femoral and sciatic nerves in dogs, sheep and lambs (Marcus et al., 1977), there is an increase (up to 50%) in blood flow delivery in the ipsilateral grey matter of the spine. Moreover, in ipsilateral white matter and contralateral spine no significant increase in blood flow was detected. These findings were commented by the authors hypothesizing a high localized metabolic response elicited by spinal neural activity. Other studies performed in the cervical (Sasaki et al., 2002) and lumbar (Brieu et al., 2010) spinal cords of rats using intrinsic optical imaging techniques confirmed the localization of neural activity and of haemodynamic response elicited by peripheral nerve stimulation. Accordingly, applying and extending the principles of brain fMRI to the spinal cord seems a logical step. The first functional study assessing the feasibility of this technique applied to human spinal cord was performed in 1996 by Yoshizawa and colleagues. Ever since, SC fMRI has been used as a

research tool to investigate spinal function in healthy controls and patients undertaking different kinds of sensory and motor tasks, but much more research is required to translate it to clinical use (Wheeler-Kingshott et al., 2014; Stroman et al., 2014). The literature about spinal fMRI is still very limited compared to that in the brain, due to low reproducibility and several technical challenges that must be tackled (Giove et al., 2004; Stroman, 2005; Wheeler-Kingshott et al., 2014). The classic model of the BOLD contrast in the brain as described by Bandettini et al. (1994) predicts that fractional signal intensity change ΔS, in T_2^*-weighted data, can be approximated by the formula:

$$\frac{\Delta S}{S} \sim -\mathrm{TE} \cdot \Delta\left(\frac{1}{T_2^*}\right) \qquad \text{Eq. 3.5}$$

TE being the Echo Time, $\Delta\ (1/T_2^*)$ the change in relaxation rate and with T_2 replacing T_2^* for Spin Echo imaging. This model relies on the assumptions that the signal change is small and its decay is characterized by a unique transverse relaxation rate. It has also been described as the signal changes detected from blood vessels are larger and do not follow this linear model. Anatomically, most of the vessels which penetrate into the spinal cord have sub-millimetric diameters and the larger vessels lie just on the surface and within the anterior median fissure. In grey matter of the spinal cord there are only tissues and small vessels, therefore the BOLD changes should follow this linear model.

In 2001 Stroman et al. (2001a) carried out an fMRI study in the brain on 12 healthy volunteers with a visual paradigm at 1.5 T and 3 T using SE and GE (EPI) sequences. They found that fractional signal changes are similar in magnitude with SE and GE data at relatively short echo times. They reported that the intercept values extrapolated to TE=0 were 0.66% to 1.0% with SE-EPI, and 0.11% to 0.35% with GE-EPI. They hypothesized that the non-zero intercept values that deviate significantly from the accepted BOLD model, might be the result of a non-BOLD component of the signal change during neuronal activity. They proposed a Signal Enhancement by Extravascular water Protons that was named SEEP effect. Other studies followed (Stroman et al. 2001b, 2002a, 2002b, 2003a, 2003b, 2005a, 2005b; Figley et al. 2010),

supporting the SEEP hypothesis. For example, Stroman et al. (2001b, 2002a) investigated contrast changes in the cervical spine of healthy controls over a range of echo times using a single-shot fast SE sequence. They found that fractional signal change extrapolated to TE=0 was roughly 2.5% (Fig. 3.5). They hypothesized that in addition to the BOLD effect there is a baseline signal change which occurs together with neuronal activation. The other option would be that BOLD response in the spinal cord is a non-linear function of TE and the intensity change diminishes rapidly at lower TEs.

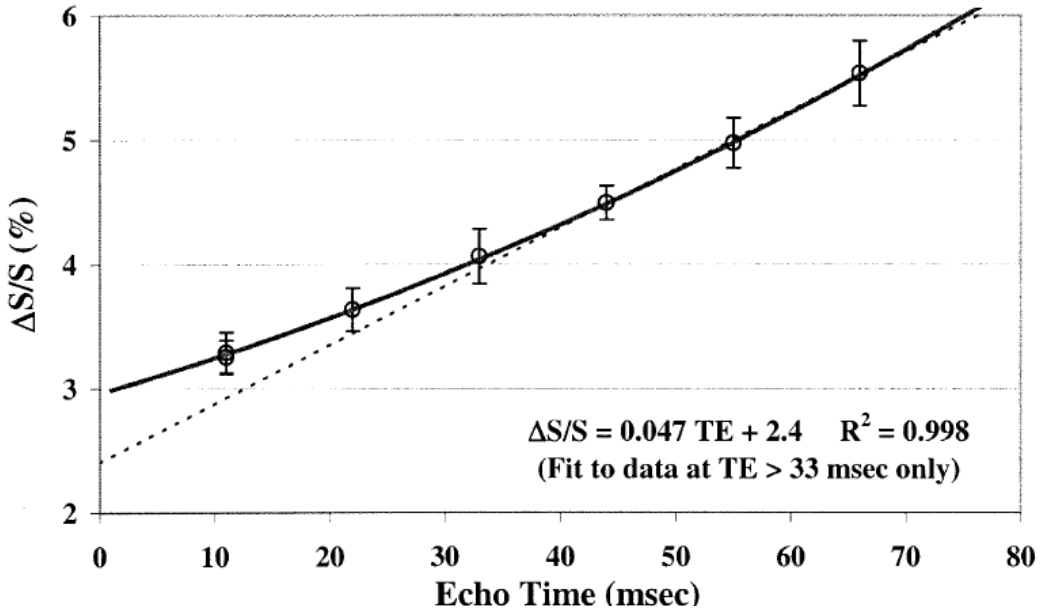

Fig. 3.5: Fractional signal changes observed in the cervical spinal cord as a function of TE. Data are average values from 15 healthy volunteers scanned at 1.5T using a SE sequence. The solid line demonstrates the result of fitting with a nonlinear model, whereas the dashed line demonstrates a linear fit to data with TE=33ms only [from: Stroman et al., 2002a].

The BOLD effect is an established technique used to detect neuronal firing and it is usually studied (in the brain) using T_2^*-weighted Gradient Echo pulse sequences with Echo-Planar Imaging readouts (GE-EPI). The BOLD effect can be detected using T_2-weighted Spin Echo (TSE and SE-EPI) sequences as well but with less sensitivity. As reported by Menon et al. (1993) and by Bandettini et al. (1994) in their studies in the brain, SE sequences are 2 times less sensitive than GE sequences at the optimal TEs (TE= T_2^* and TE=T_2) in detecting the BOLD contrast. If TE is different from T_2^* or T_2, SE sequences can be 3.5 times less sensitive than GE sequences.

In the spinal cord the ratio of signal changes with GE data to those with SE data is about 1 to 1 and it is not in agreement with the BOLD theory (Stroman, 2005). Stroman et al. (2003a, 2003b, 2005b) performed studies in the brain using PD-weighted sequences at short TE (21, 23ms) and found that in each experiment the signal enhancement was always around 2%, even using different magnetic fields (B=0.2T, 1.5T, 3T). He concluded that this intensity enhancement was not dependent on the field strength and therefore could not be due to the BOLD effect (Gati et al., 1997).

Moreover, Stroman et al. (2003b, 2005b) compared the regions of neuronal activation obtained with GE sequences and with SE sequences and found that areas of SEEP activity are immediately adjacent to areas of BOLD activity, with very little overlap. These studies seemed to confirm a non-BOLD contribution to signal enhancement due to neuronal activity.

Adding a few more details about Eq. 3.5, let us refer to Eq. 2.2 and rewrite it as:

$$S = \rho(H)\left(e^{-\frac{TE}{T_2^*}}\right)\left(1 - e^{-\frac{TR}{T_1}}\right) = S_0\, e^{-\frac{TE}{T_2^*}} \qquad \text{Eq. 3.6}$$

being $\rho\,(H)$ the proton density, TR the repetition time, T_1 the longitudinal relaxation time, S_0 the signal at the echo time TE=0 (T_1 dependent term) with T_2 replacing T_2^* for Spin Echo imaging. The fractional signal change during activation can be expressed as:

$$\frac{\Delta S}{S} = \frac{\Delta S_0}{S_0} - TE \cdot \Delta\left(\frac{1}{T_2^*}\right) \qquad \text{Eq. 3.7}$$

In Eq. 3.7 the signal enhancement is due to the term in Eq. 3.6 plus a TE-independent term that depends on spin density changes and includes contribution from inflow effects (T_1). However, in the BOLD theory, spin density can be considered constant and inflow effects, more evident for T_1-weighted imaging, can safely be neglected for typical EPI-acquisition with TR >1 sec (Gao and Liu, 2012).

3.6 - Criticism about SEEP effect

Early studies concerning the characterization of functional MRI in the spine were carried out on healthy volunteers by Yoshizawa et al. (1996), Stroman et al. (1999), Madi et al. (2001), Backes et al. (2001). They all used a hand motor task to look for activated voxels in the cervical spinal cord. They used GE sequences with TE between 40-50msec at 1.5T and TE around 30msec at 3T because these are the ones typically used in the brain. They concluded that fMRI in the spinal cord is feasible even if there are many difficulties that this technique implies.

The SEEP effect was first hypothesized by Stroman et al. (2001a, 2001b) and relies on proton-density weighted imaging (see section 2.4). Worldwide there are just a few groups investigating spinal fMRI and there are controversies concerning different methodological approaches. At present, the blood-oxygen-level-dependent (BOLD) contrast is the mainstay of fMRI neuroimaging and the SEEP effect has been viewed more recently with scepticism. Jochimsen et al. (2005), for example, argued about the correlation between the increase of water proton density and neuronal activity. They performed fMRI experiments in the brain using a SE-EPI sequence with short TEs on a 3T scanner and their results did not confirm the hypothesis of a significant increase in extravascular proton density at TE=0. They found that the fMRI signal change vanishes if extrapolated to TE=0 and concluded that the SEEP effect is negligible. They proposed an alternative explanation of the results that Stroman et al. (2001a, 2003a, 2003b) obtained using SE sequences with short TEs. They suggested an artificial offset in functional contrast due to the inclusion of false positives generated by the low threshold used to detect the activated voxels. They claimed the SEEP effect was generated purely by the particular strategy of evaluating fMRI data and did not reflect any physical effect. Nonetheless, this study cannot explain the ability to measure changes in proton density at very low magnetic field strengths (0.2 Tesla) as reported by Stroman et al. (2003a), Geng Li et al. (2005), and Man Cheuk Ng et al. (2006). Furthermore, it does not preclude the possibility of proton density changes in different areas from ones where neuronal activity is detected with the BOLD contrast. Stroman et al. (2005b) in a further study replied to Jochimsen's experiment, questioning the accuracy of the applied methods. In Jochimsen's study, fMRI scans in the brain were carried out on 8

healthy volunteers. Each subject was scanned at 4 different TEs (9, 19, 29, 39msec) during different sessions using a visual paradigm. An fMRI scan with TE=80 msec was acquired as a reference to create a fixed mask of activated voxels to compute signal changes for the fMRI scans performed with the shorter TEs. Stroman's group pointed out that those masked voxels activated at TE=80msec and more sensitive to the BOLD effect, wouldn't be activated at short TEs because the SEEP effect (more important at small TEs because of the proton-density weighting) is elicited in different areas. Stroman et al. (2005b) confirmed a previous finding by his own group (Stroman et al., 2003b): areas of SEEP activity are immediately adjacent to areas of BOLD activity, with very little overlap. Moreover, Jochimsen's group results were derived from masks consisting of all activated voxels with $p<0.005$ at TE=9msec and reported an average signal enhancement of about 0.75% on an average over 65 activated voxels in the visual cortex of 6 out of 8 volunteers. If all the voxels activated at the different TEs were included in the analysis, the extrapolation value at TE=0 was 0.82+/-0.07% that is consistent with the value of 1.03+/-0.19% reported by Stroman et al. (2001a) using a 3T scanner.

Figley et al. (2010) contested Jochimsen's study applied Bonferroni correction on about 1700 voxels which was too harsh. They concluded that Jochimsen's experiment relied on assumptions that reduced the sensitivity of data to non-BOLD effects.

Other criticisms about SEEP effect were directed by Yacoub et al. (2003) and Jin et al. (2006) that, using SE sequences, investigated the non-linear TE-dependency of signal changes and found results similar to Stroman's findings. Yacoub et al. (2003) performed a functional study at 4T and 7T in the brain of healthy controls and Jin et al. (2006) at 9.4T in the brain of cats. Both studies found that the application of flow-crushing gradients, removing vascular signal contributions, could make linear the TE-dependent signal change. Eventually, they both claimed that the non-linearity behaviour was due to a change in blood vascularity rather than to an increase in extravascular spin density.

The terms 'BOLD signal' and 'fMRI signal' are often used synonymously, although there are other functional methods that do not rely on changes in deoxyhaemoglobin concentration in blood vessels, and SEEP effect is one of these. SEEP effect has been suggested to be a non-haemodynamic fMRI method that exploits the signal from the fluid that is pushed out of the

cells during cellular swelling related to neural activity. Another non-haemodynamic method was reported in the brain by Le Bihan and colleagues (Le Bihan et al., 2006; Le Bihan, 2007) that, using high b-value diffusion-weighted fMRI, claimed to detect changes in activity-related cellular swelling. There are other functional haemodynamic techniques used to detect neurovascular and neurometabolic changes correlating with neuronal activity, such as VASO (VAscular-Space-Occupancy) fMRI (Lu et al., 2003, 2012, 2013) and ASL perfusion (Detre et al., 2002; Borogovac et al., 2012) and investigate changes in blood volume and blood flow.

However, Stroman et al. (2014) suggested that, depending on the way a spinal functional study is performed, neuronal activity is detected as a combination of BOLD and SEEP contrasts whose contributions vary according to the used MRI parameters. Nevertheless, the optimal combination of parameters to obtain the best combination of sensitivity, localization, contrast and reliability is not known.

The SEEP effect is still debated in literature, and not completely accepted by the scientific community. Although there are studies performed with different techniques (Hennig et al., 1995; Ohta et al., 1996; Fujita et al., 1997; Darquié et al., 2000) that seem not to deny the possibility of an increase in water concentration (due to an increase in cells size) elicited by neuronal activation, there are others (Kim and Ogawa, 2012) that report that there is no clear evidence whether this phenomenon can be exploited to map neuronal activity and, in particular, if it provides a valid alternative to BOLD effect in the spinal cord.

CHAPTER 4 – PREPROCESSING

Introduction

Functional MRI of the spinal cord has shown to be technically feasible using different methods (Yoshizawa et al., 1996; Stroman, 2005; Brooks et al., 2008; Bouwman et al., 2008; Cohen-Adad et al., 2010). Nevertheless, performing fMRI in the spinal cord requires appropriate modifications of standard brain fMRI protocols and obtaining good results is not straightforward due to several issues, such as: small cross-sectional size of the spinal cord grey matter, susceptibility artefacts, lack of dedicated software, physiological noise (Giove et al., 2004; Stroman, 2005, 2014; Leitch et al., 2010; Wheeler-Kingshott et al., 2013). Considering spinal fMRI just an extension of fMRI in the brain and thus applying the same pre-processing steps performed in the brain might not be correct. This issue should not be underestimated because results may be biased by how data are analyzed. Regrettably, there is no standard pipeline (Cadotte et al., 2012; Wheeler-Kingshott et al., 2014) for analysing functional spinal data and this causes several limitations in comparing results from studies that use different analysis methods.

This chapter focuses on work that I performed on developing pre-processing steps of spinal fMRI data: realignment, slice-timing and smoothing. The aim was to evaluate the most suitable analysis pipeline for functional datasets in the spine, giving a critical opinion (based on in-vivo results) of both advantages and drawbacks of each step.

4.1 - Effects of realignment

This is the first of 3 sections (4.1 - 4.3) in which different studies are reported, aiming at evaluating the best strategy to be adopted in the analysis pipeline.

The first pre-processing step that I am going to deal with is realignment. Changes in signal intensity over time in any voxel can be caused by motion and this is a serious confound for fMRI. Despite cooperative subjects and restraints on their movements, it is not possible to keep subjects perfectly still. There will always be displacements of up to several millimetres. In the spine, movement is an important issue, more than in the brain, due to the fact that the spine is located close to lungs and heart and so it can be easily affected by their movements. The time evolution of each activated voxel, represented by a time-series, is related to neuronal activity underlying the blood oxygen-level-dependent response. Realignment is needed in order to study how signal changes throughout the acquisition of different volumes but, regrettably, there is not any standardized method to realign spinal cord volumes. Without considering the inter-subject realignment that is hindered by lack of commercial software including a spinal template, even the intra-modality intra-subject realignment is questionable.

4.1.1 - Purpose

To assess the best way to realign a functional dataset acquired in the spine.

4.1.2 - Materials and Methods

Aiming at finding the best way to realign the volumes of a functional dataset I measured the TSNR in 20 voxels in the spinal cord of 5 subjects that undertook a resting-state scan. ZOOM sequence was used and the imaging parameters were those reported in section 2.8.

The slices were prescribed transverse to the cord and the central slice was always placed in the middle of the C6 spinal segment. The TSNR was calculated using 3 different realigning

methods that can be found in published papers:

1) 3D rigid-body realignment with 6 degrees of freedom using SPM software (Valsasina et al., 2008, 2010; Agosta et al., 2009a, 2009b; Nejad et al., 2014).

2) 3D rigid-body realignment of cropped images with 6 degrees of freedom using SPM software (Nash et al., 2013).

3) 2D slice-wise realignment with FSL (flirt) software (Brooks et al., 2008, 2012; Cohen-Adad et al., 2010; Cohen Adad and Wheeler-Kingshott, 2014; Stroman et al., 2014) allowing corrections for translations in the x,y plane and rotations along the z axis.

In developing 3) I implemented a 2D-realignment procedure using FSL software (FLIRT) commands wrapped together using MATLAB (or, in an equivalent way, using C++). Only translations in the x,y plane and rotations along the z axis were allowed, as suggested by Cohen-Adad et al. (2009b).

4.1.3 - Results

I have reported results from the different realignment methods in Table 4.1. These measurements were obtained from voxels of grey matter (spotted on the mean images) and averaged over the five subjects.

Within each method, TSNR results were similar between the subjects. The best way to realign images was the 2D-realignment that guaranteed an average TSNR of 12.4 (+/-1.0). Cropping images resulted the worst way to realign images, with an average TSNR of 7.3 (+/-0.6) and the 3D full-image realignment had an average TSNR of 8.2 (+/-0.6).

	Realign_3D	Cropped_3D	Realign_2D
Subject 1	8.5 +/- 2.2	7.1 +/- 1.5	13.5 +/- 3.0
Subject 2	8.1 +/- 2.5	7.5 +/- 2.4	12.3 +/- 2.0
Subject 3	7.7 +/- 1.7	7.0 +/- 1.5	11.5 +/- 2.2
Subject 4	9.0 +/- 2.8	8.2 +/- 2.1	13.4 +/- 2.4
Subject 5	7.5 +/- 2.4	6.8 +/- 1.8	11.5 +/- 2.8
Mean +/- std	8.2 +/- 0.6	7.3 +/- 0.6	12.4 +/- 1.0

Table 4.1: TSNR obtained in the subjects using the 3 different realigning methods. Mean values and standard deviations are reported as well.

4.1.4 - Conclusion and Discussion

2D-realignment optimized the motion-correction for axial spinal cord image series.

3D-realignment instead, visually checked, didn't look good: there was a loss of data at edges of the volumes and the slice at the top and the one at the bottom appeared incomplete (Fig. 4.1). At the beginning, I opted to discard these slices and to consider in the analysis only the central ones, but then I deemed the possibility that these ones also might be realigned incorrectly. Results in Table 4.1 refer to the analysis with SPM8, as done in previous papers (Valsasina et al., 2008, 2010; Agosta et al., 2009a, 2009b; Nejad et al., 2014), however, I performed TSNR calculations in one subject using both SPM8 and FSL and results showed negligible differences.

Recently, there is a trend toward performing slice-by-slice realignment in the spine (Brooks et al., 2008, 2012; Cohen-Adad et al., 2010; Cohen Adad and Wheeler-Kingshott, 2014; Stroman et al., 2014) although 3D-realignment is still accepted (Valsasina et al., 2008, 2010; Agosta et al., 2009a, 2009b; Nash et al., 2013; Nejad et al., 2014).

In particular, in a recent paper by Nash et al. (2013), 3D rigid-body motion correction was performed after cropping the images and accounting only for the area included within the spinal cord. A criticism might be that realignment algorithms usually exploit spatial information from distinguishable structures (bones, muscles, tissues) included in the FOV but lying outside the cord. Due to the subtle contrast in functional images between different tissues within the cord and to the small area of it, masking the cord might hinder the realigning process and this

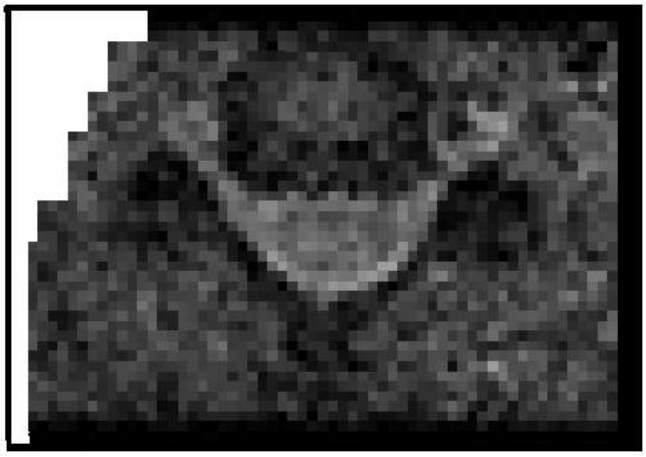

Fig. 4.1: Incomplete image of a slice at the bottom of a volume after applying 3D realignment using SPM8.

procedure might not be correct. Furthermore, functional scans were masked using an anatomical scan as reference but it was not reported whether the anatomical scan was only used as visual reference or it was included into an automatic processing. However, in the pilot study I performed, images were cropped in such a way to include a slightly larger region, comprising spinal canal and bones too (Fig. 4.2). This was made in order to facilitate the detection of the spine by the realigning algorithms that work minimizing the sum of squares of the image difference between a pair of images (Woods et al., 1992; Friston et al., 1995). Nevertheless, results were inadequate.

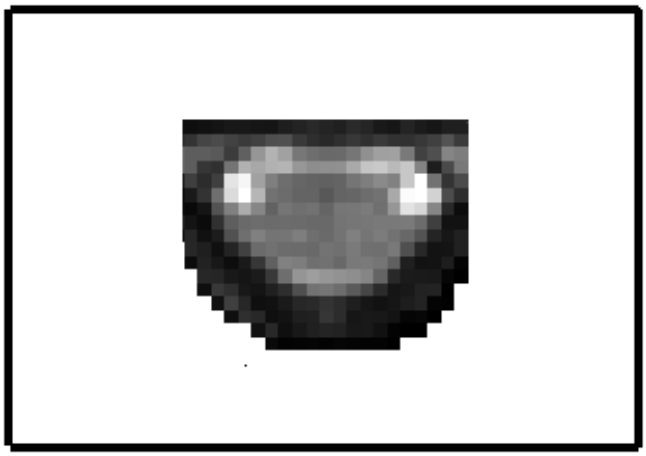

Fig. 4.2: Example of cropped image used for testing the 3D realignment.

Slice-by-slice realignment is recommended because it takes into account non-rigid motion of structures through the slices and thus it is more suitable than a 3D rigid-body motion-correction.

Theoretically, slice-wise realignment could be performed using SPM8 too, modifying a MATLAB file called 'SPM_realign.m' included in the SPM8 package. The 2D-realignment option resulted to be the most suitable in the spine and will be applied to all functional datasets analysed in the following of this thesis. Nevertheless, it is important to underline that too large movements might invalidate the realignment, because of the local spatial distortions in the spinal shape due to the change in location within the magnetic field (Jezzard and Clare, 1999).

4.2 - Effects of slice-timing

Slice-timing correction involves the correction of differences in timing across different slices acquired at different times within the same volume. It is usually considered optional and not a main issue of the pre-processing analysis, in fact, there are spinal functional studies:

1- Performing slice-timing correction (STC) as the first step of the analysis (Cohen-Adad et al., 2009a).

2- Not performing slice-timing but adding time-derivatives (TD) in the GLM instead (Cohen-Adad et al., 2010).

3- Not mentioning about slice-timing at all (Govers et al., 2007; Brooks et al., 2008).

4.2.1 - Purpose

To assess the influence of timing corrections comparing results from the GLM analyses in terms of the t-values.

4.2.2 - Materials and Methods

Five volunteers were scanned using the ZOOM sequence and the imaging parameters were those reported in section 2.8. Functional scans were performed with sensory stimulation of the palm of the left hand of each subject with a pointed object at the rate of about 5 Hz. The block design comprised 10 rest epochs alternating with 10 stimulus epochs, each lasting 36 seconds. The 9 slices were prescribed transverse to the cord and the central slice was always placed in the middle of the C6 spinal segment (Fig. 4.3). I have tested each of the 3 approaches mentioned above, *i.e.*: using slice-timing correction (STC), adding time-derivatives (TD) to the GLM and applying no corrections to the data (UN). 2D-realignment was applied to all datasets and movement parameters were included in the GLM analyses. Only the activated voxels deemed inside the spinal cord were considered in the results. Results were evaluated comparing the t-values: the best method gave the largest t-values, reflecting the best fit of the model to the experimental data.

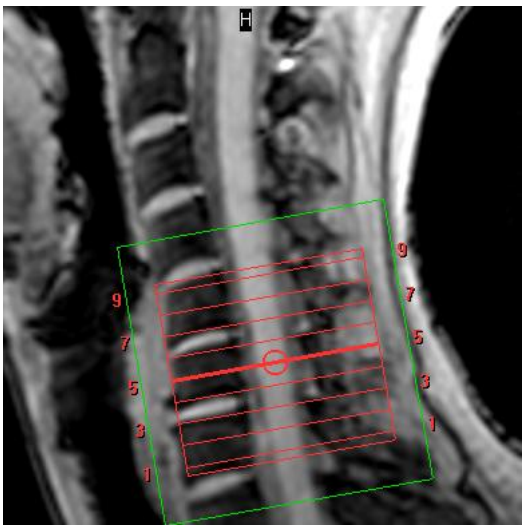

Fig. 4.3: Localization of the slices.

4.2.3 - Results

Most of the activated voxels found using the different methods overlapped.

Using STC, in all subjects the number of activated voxels inside the spinal cord was very close to one obtained not applying any corrections (Fig. 4.4). For 3 subjects, the mean t-values obtained with these two approaches (STC and UN) were identical within the error bars of one

standard deviation (Fig. 4.5). In two cases instead, the mean t-values obtained applying STC were slightly higher.

For 4 subjects, activated voxels obtained applying TD were the same as the case in which no correction was performed (Fig. 4.4) and the mean t-values were very similar for all subjects (Fig. 4.5).

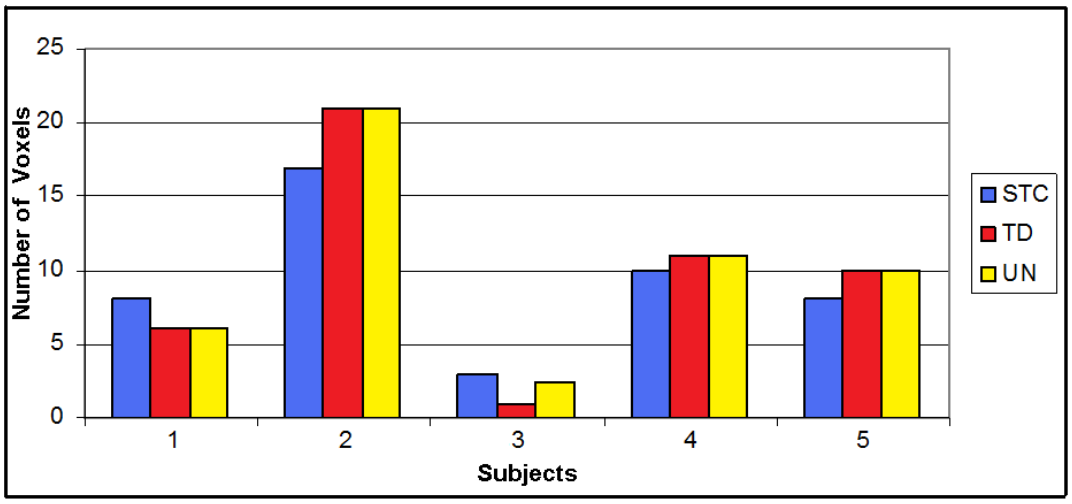

Fig. 4.4: Number of activated voxels within the SC of the 5 subjects obtained using Slice Timing Correction (STC), Temporal Derivatives (TD) and not applying any correction (UN).

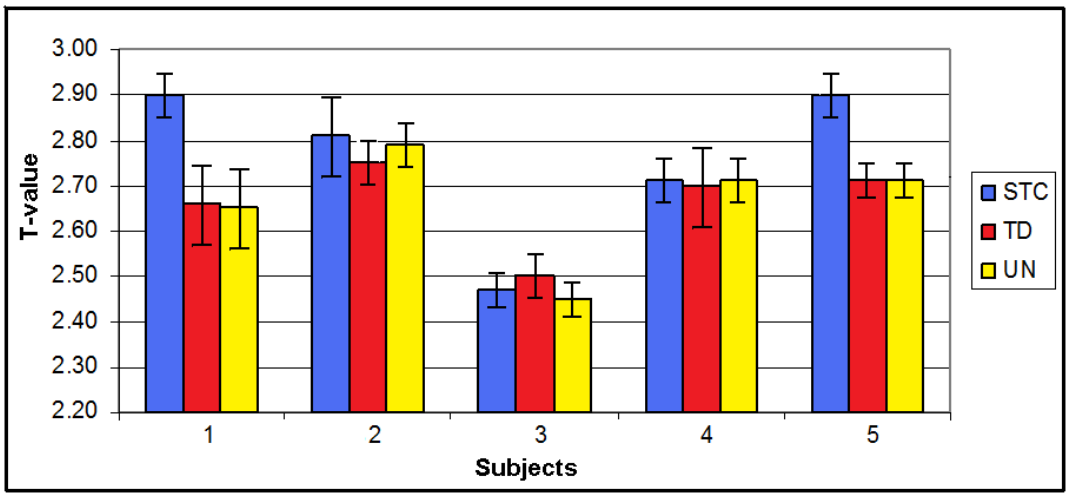

Fig. 4.5: Histograms of the mean t-values for the activated voxels within the SC of the 5 subjects obtained using Slice Timing Correction (STC), Temporal Derivatives (TD) and not applying any correction (UN).

4.2.4 - Conclusion and Discussion

At this stage of the analysis we are not really interested in the spatial localization of the activated voxels. Any comments about it are postponed to the next chapters, where a more complete pre-processing pipeline will be performed.

Both STC and TD had a negligible influence on the final results. Neither using STC nor TD changed meaningfully the number of activated voxels (and their location) and their significance.

In conclusion, I opted to not perform any time correction to the datasets acquired in this thesis due to the fact that this pre-processing step does not offer any advantage.

In a similar study performed in the brain (Sladky et al., 2011), at both single-subject and group levels, a few TRs and paradigm designs have been tested. In this paper the authors suggest to perform slice-timing correction (at single-subject level) because 'it can suppress bias in quantitative parameter estimates (β values)'. Moreover, they report that choice to use derivatives is arguable and does not have a significant influence on the results.

In the study I performed instead, only the TR and paradigm design that I would use in the rest of my thesis were considered. Although I have discussed the results in terms of t-values (t) instead of β values, the underlying idea is the same as in Sladky's et al. paper (2011). The role of the parameter estimate in the statistics, also called the estimated β value, will be discussed in detail later in this thesis (section 5.1).

However, it is possible to obtain t from a parameter estimate considering the uncertainty in its estimation (standard error, SE):

$$t = \frac{\beta}{SE(\beta)} \qquad \text{Eq. 4.1}$$

In conclusion: β, t and p-value give information about how well the model fits the data for a certain voxel. If a voxel does not present activation, the β value is not significantly different from zero. In such a case, the evaluated t is lower than the significance threshold. In other words, probability that the time course of that voxel is driven by neural activity is lower than the

threshold. For the present study: t=2.35 corresponding to p-value<0.01 (uncorrected) threshold was considered.

4.3 - Effects of smoothing

In the literature, there are several studies reporting the effect of smoothing on functional datasets, pointing out at both advantages and drawbacks (Geissler et al., 2005; Friston et al., 2006; Triantafyllou et al., 2006; Jo et al., 2007; Weibull et al., 2008).

Smoothing involves a convolution of the fMRI data with a 3D Gaussian kernel of specified full-width at half-maximum (FWHM) and its effect is to replace the value of each voxel with the weighted average over its surrounding region. It results in a blurring of the image and in a more pronounced spatial correlation within the data.

Smoothing is commonly used for several reasons: to increase the SNR (signal-to-noise ratio), to make the error distribution more normal to comply with the GLM (General Linear Model) assumption, to improve spatial overlap by blurring over minor anatomical differences and registration errors (Worsely and Friston, 1995; Friston et al., 2006).

In general, smoothing is highly recommended (Friston et al., 2006) in group studies because it reduces the variation between different subjects, increasing the overlap of activated areas across subjects. Dealing with single subject studies in the spinal cord instead, usefulness of smoothing is still debated. Some researchers prefer to smooth spinal datasets, although using different Gaussian kernel sizes (Madi et al., 2001; Cohen-Adad et al., 2007; Kong et al., 2012), others do not apply any smoothing instead (Stracke et al., 2005; Valsasina et al., 2008, 2010; Agosta et al., 2009a, 2009b; Summers et al., 2010; Xie et al., 2012).

4.3.1 - Purpose

To show the effect on the statistical maps of smoothing the spinal functional data.

4.3.2 - Materials and Methods

This study, including 5 subjects, was performed using the ZOOM sequence with the imaging parameters reported in section 2.8. Functional paradigm and slices prescription were the same as in section 4.2. 2D-realignment was applied to all datasets and movement parameters were included in the GLM analyses.

4.3.3 - Results

A comparison between results obtained applying 2 mm FWHM smoothing and no-smoothing is shown in Fig. 4.6.

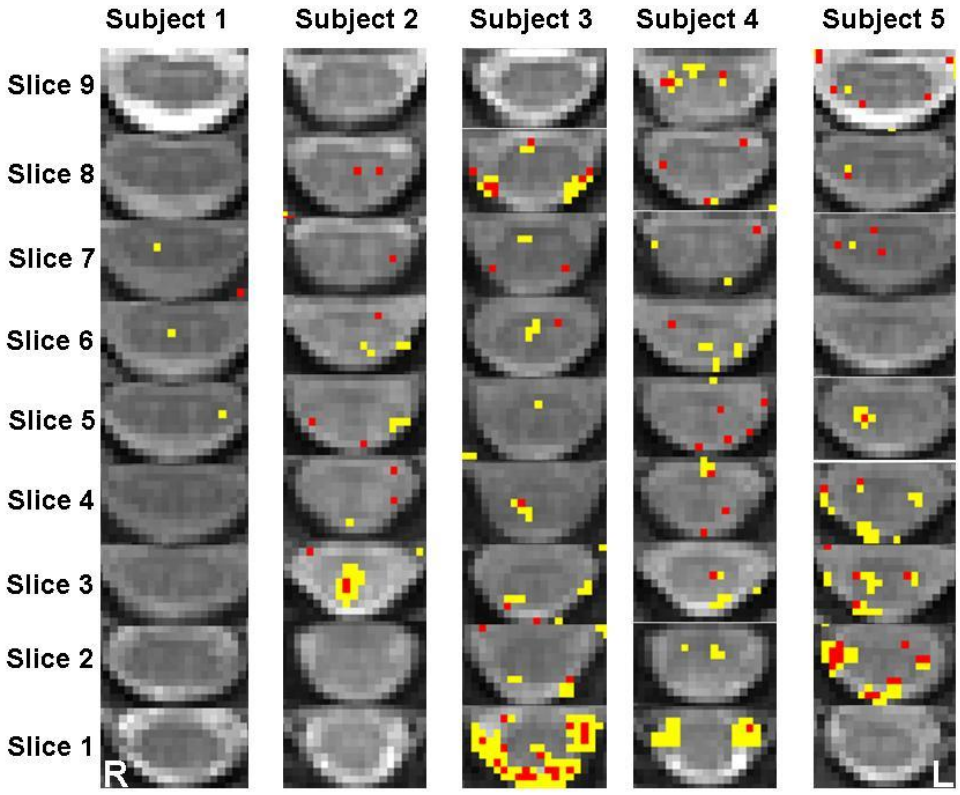

Fig. 4.6: Activations detected in the 5 subjects applying 2 mm FWHM smoothing (in yellow) and no-smoothing (in red) overlaid on the mean image. The slice number refers to Fig. 4.3.

4.3.4 - Conclusion and Discussion

As underlined in the previous subsection 4.2.4, a deeper analysis of the elicited neuronal activity will be discussed later, after introducing physiological regressors to model the structured noise.
The main drawback about smoothing the images is the reduction of spatial resolution.
I chose to report only the results obtained applying a small amount of smoothing because a larger amount would make the activation blobs too large to be deemed real on anatomical basis (see below).
The images from the proposed pilot study suggest that smoothing spinal images may be a disadvantage. This statement is supported both experimentally and theoretically by the following reasons. Smoothing might cause activation blobs to spread both in and through the spine, making really difficult to draw any conclusion about reliability of neuronal activity. Due to the small size of the spine, the location of activated voxels needs to be as much accurate as possible, as false activations in the CSF might be only a few voxels far from plausible neuronal activity in the grey matter. Furthermore, considering an axial spinal image, neuronal activity is expected to have an extent of about 3-4 mm^2 (Standring et al., 2005) and thus, using voxels with in-plane dimensions of 1.19 x 1.19 mm^2 (the one that I used), only 2 or 3 voxels would be expected to be activated. Blurring images makes the dataset prone to partial volume effects and may result in shifting of activation and merging of distinct blobs of activation (Lindeberg et al., 1999; Mikl et al., 2008). Reasonably, the approach that I would suggest is to apply smoothing small enough that it doesn't reach across the white matter to incorporate CSF signal in the grey matter signal, and big enough that you should get a slight SNR improvement. Unfortunately, spatial specificity in the spinal cord is easily lost, even applying a small amount of smoothing (Fig. 4.6). Two activated voxels (or two distinct blobs of activation) will merge into one if their distance is less than twice the FWHM of the Gaussian kernel used. It should be also noted that an increase in SNR might have a negligible benefit if spatial specificity is lost, especially when there are such small regions to be investigated. Moreover, if the filter width is set too small, there is practically no positive effect on the SNR while the spatial resolution is reduced.
For all these reasons, I have opted not to smooth the datasets analysed in the next chapters.

CHAPTER 5 - PHYSIOLOGICAL NOISE

Introduction

Another important aspect of signal fluctuations is given by the cardiac- and respiration-related physiological noise. After having discussed preprocessing steps in chapter 4, here physiological noise is tackled. A theoretical basis is introduced and different methods aiming at reducing structured noise are discussed. To begin with, a discussion upon the general linear model and its usefulness in the functional analysis is reported. Two studies are presented in this chapter. The first one includes a comparison between results obtained applying a RETROICOR-like method and the DRIFTER algorithm. The second one is a test-retest reliability study analysed with the pipeline developed in chapter 4 and including both CSF regressors and physiological (cardiac and respiratory) denoising. The literature concerning the topics investigated in each study is revised before presenting the study.

5.1 - General Linear Model

The general linear model (GLM) has been used for over 20 years to analyse functional datasets and, because of its simplicity, it is still pivotal in fMRI statistical analysis.

A GLM is used to fit a model to the experimental data. A good fit means a high probability for the activation to be stimulus-induced. The model is a pattern that data are expected to follow and, in case of block design, this model is given by the convolution of an input function, mimicking the spike of synaptic activity, and a boxcar function that is different from zero during the stimulation periods. The maths behind the convolution will be dealt with more in detail in section 6.2.

The GLM theory relies on the assumption that experimental data can be expressed by additions and subtractions of known data (independent variables), that are weighted with appropriate coefficients, and an error function. The error function is characterized by a zero mean Gaussian distribution (Friston et al., 2006; Poline and Brett, 2012) and contains the variability of the experimental data that is not explained by the independent variables.

The GLM is usually reported using its elegant matrix formulation:

$$\mathbf{Y} = \mathbf{X}\boldsymbol{\beta} + \mathbf{e} \qquad \text{Eq. 5.1}$$

In Eq. 5.1 the data matrix **Y** (that represents the observed response) is given by the product of the design matrix **X** (also called independent variables, including all the explanatory variables) and the matrix **β** (containing all the scalar parameters) plus an error matrix. The response (also called dependent variable) can thus be described in terms of a linear combination of explanatory variables weighted with the **β** coefficients (plus an error term). These explanatory variables, represented by the columns of the design matrix, are often referred to as regressors or covariates and each of them models a cause of the data (Smith, 2004; Friston et al., 2006; Poline and Brett, 2012).

After having described the variables embedded in the GLM, let's now consider a specific example that allows us to rewrite Eq. 5.1 in terms of a system of equations and to better

understand the matrix notation used. The voxels in the images are statistically processed by SPM8 software using a univariate approach (*i.e.* the model is applied to each voxel in the same way) and this allows us to refer to just one voxel. Considering a certain voxel denoted by the index j (with j=1, ... , J), let us suppose to measure the value of a response variable Y related to that voxel (*e.g.* the signal) in all the scanned volumes.

Let us indicate with $Y_j(t)$ the function corresponding to the variable throughout all the time points:

$$Y_j(t) = x_j(t)\beta + e_j(t) \qquad \text{Eq. 5.2}$$

where $x_j(t)$ stands for the model, β for a coefficient and $e_j(t)$ is the error function.

Eq. 5.2 is a very simple case, but if the model is made up of k =1, ... , K (K<J) explanatory variables, at a generic time point it is possible to write:

$$Y_j = x_{j1}\beta_1 + \cdots + x_{jk}\beta_k + \cdots + x_{jK}\beta_K + e_j \qquad \text{Eq. 5.3}$$

The previous Eq. 5.3 refers to just one observation, however, considering all J indices, it follows:

$$\begin{aligned} Y_1 &= x_{11}\beta_1 + \cdots + x_{1k}\beta_k + \cdots + x_{1K}\beta_K + e_1 \\ \vdots &= \vdots \\ Y_j &= x_{j1}\beta_1 + \cdots + x_{jk}\beta_k + \cdots + x_{jK}\beta_K + e_j \\ \vdots &= \vdots \\ Y_J &= x_{J1}\beta_1 + \cdots + x_{Jk}\beta_k + \cdots + x_{JK}\beta_K + e_J \end{aligned} \qquad \text{Eq. 5.4}$$

The system of equations above (Eq. 5.4) can be written in the equivalent matrix form:

$$\begin{pmatrix} Y_1 \\ \vdots \\ Y_j \\ \vdots \\ Y_J \end{pmatrix} = \begin{pmatrix} x_{11} & \cdots & x_{1k} & \cdots & x_{1K} \\ \vdots & \ddots & \vdots & \ddots & \vdots \\ x_{j1} & \cdots & x_{jk} & \cdots & x_{jK} \\ \vdots & \ddots & \vdots & \ddots & \vdots \\ x_{J1} & \cdots & x_{Jk} & \cdots & x_{JK} \end{pmatrix} \begin{pmatrix} \beta_1 \\ \vdots \\ \beta_k \\ \vdots \\ \beta_K \end{pmatrix} + \begin{pmatrix} e_1 \\ \vdots \\ e_j \\ \vdots \\ e_J \end{pmatrix} \qquad \text{Eq. 5.5}$$

that is the expanded expression for Eq. 5.1, showing explicitly that each of the K columns of the model represents a regressor and each row refers to a different observable. The error functions are independent and Gaussian distributed.

The GLM can be used to regress out the covariate corresponding to a confounding variable (also called extraneous variable, confound or confounder) that correlates with both dependent and independent variables and whose effect is misleading for the purposes of detecting stimulus-induced neuronal activity. Time evolution of functional signal in an activated voxel throughout all the volumes can be affected by sources of noise whose effects cannot be neglected. A GLM allows us to rule out, or at least reduce, these unwanted effects. This is the case of physiological noise or movement that can be accounted for introducing appropriate regressors into the experimental design (*i.e.* the paradigm convolved with a HRF).

5.2 - Upon the cardiac-gated technique

As reported in previous studies (Dagli et al., 1999; Piche et al., 2009), the main contribution to physiological noise has got cardiac origins and for this reason, such contribution cannot be neglected in the analysis. Cardiac-gating consists of acquiring a slice a few hundred milliseconds after a heart peak but before the following peak, in such a way to reduce the cardiac-related signal variability.

However, it introduces additional signal variance due to T_1-effects and implies further corrections not easy to work out using available software for functional analysis. Furthermore, heart rate could correlate with the experimental paradigm giving false statistical activations (Tousignant-Laflamme et al., 2005).

Guimaraes et al. (1998) and Malinen et al. (2006) performed studies employing cardiac-gating techniques that resulted in a longer acquisition time because of the dependence of the duration of scanning session on subjects' heart pace instead of on the TR.

They suggested a formula to correct (in each voxel) for the different amount of recovered longitudinal relaxation related to different TRs, that is usually referred to as T_1-effect(s) or partial saturation effect(s).

The proposed formula is:

$$S_{i,n} = A_{i,n}\left[1 - e^{-\left(\frac{t_n}{T_{1,n}}\right)}\right] \qquad \text{Eq. 5.6}$$

where: $S_{i,n}$ is the measured signal for the i-*th* voxel and the n-*th* acquisition, $A_{i,n}$ is the maximum signal in the absence of T_1 relaxation, t_n is the time between the volumes n-*th* and (n-1)-*th*, $T_{1,n}$ is the longitudinal relaxation time for the tissue included in the n-*th* voxel. However, this approach is tricky and has limitations in the assumption of a single T_1 value for each voxel, neglecting possible partial volume effects. Moreover, this issue might be worsened by a not accurate realignment. In most functional studies a constant TR is used and cardiac-induced variations of the signal are minimized by incorporating an appropriate physiological regressor into the GLM analysis. The basic idea underpinning the cardiac regressor (Hu et al., 1995) relies on the possibility to associate a unique cardiac phase to each slice and thus, to relate the cardiac pulse to the signal variability. This method will be discussed in detail in section 5.6.

5.3 - Upon the breath-holding technique

In early papers breath-holding technique has been used (Stroman et al., 1999; Stroman and Ryner, 2001), however, it is wiser trying to model the signal fluctuations caused by respiration rather than asking subjects to hold the breath many times within a scanning session. Firstly, not all the subjects undertaking breath-holding, and especially patients, are able to perform it correctly, *i.e.* keeping always the same volume of air during the repeated breath-holdings. Secondly, another issue concerns variations of depth and rate of breathing that result in blood flow and oxygenation changes. As reported by Van den Aardweg et al. (2002), changes in respiration are related to fluctuations in the level of CO_2 that, having vasodilator properties, may cause either vasodilation or vasoconstriction, depending on concentration. Moreover, it has been assessed that respiration elicits motion of the chest, causing magnetic field inhomogeneities (Raj et al., 2001; Brosch et al., 2002) and thus signal changes.

As reported in the next section 5.4, different techniques aiming at reducing the physiological fluctuations of MRI signal due to respiration have been developed, however, most of them rely on the histogram-based method (Glover et al., 2000) that will be discussed in detail in the sections 5.6 and 5.8.

5.4 - Literature: overview of physiological denoising

As previously mentioned, results obtained in the spinal cord fMRI have often been controversial. The reason can be sought in the way the different experiments were performed. The choice of the sequence and imaging parameters used is of primary importance but there are also other important aspects that cannot be neglected, such as the type of stimulus and its duration, frequency, interstimulus interval, stimulus intensity and the number and timing of rest/activation epochs (Cadotte et al., 2012). All of these factors can affect the activity of spinal neurons, as reported in classical electrophysiology experiments by Wall et al. (1979). The post-

processing of functional data is another issue that is still controversial. It has been demonstrated that applying physiological regressors that model the effect of physiological noise aids the identification of neuronal activation improving discrimination of activation and reducing false-positive detection. Such a technique was developed by Glover et al. (2000) and further on implemented via a general linear model (GLM) approach by Restom et al. (2006). This technique that allows the correction of physiological motion effects was named RETROICOR (RETROspective Images CORrection). The correction method assumes that the time series in a pixel is corrupted by additive physiological noise. Respiration effects and cardiac pulsatility can induce signal modulations in functional MR image time series that increase noise and degrade the statistical significance of activation signals (Glover et al., 2000). RETROICOR-like methods aim at reducing these physiological additive noise components fitting with low-order Fourier series expansions the cardiac and respiratory traces recorded during the fMRI acquisition and removing their effects from images. In order to achieve this purpose the cardiac and respiratory phases associated to each slice within the respective cardiac and respiratory cycles have to be computed.

So far, different approaches have been studied independently by different groups, each one developing the method in a slightly different way. I quote, for example, the studies by Lund et al. (2006), Stroman (2006), Brooks et al. (2008), Deckers et al. (2006), Särkkä et al. (2012).

Lund et al. (2006), assuming that the cardiac cycles do not change dramatically over a TR, computed the physiological regressors within a RETROICOR-like framework using the acquisition time of the first slice in a volume and applying the same parameters to all slices in the volume. They found that this method allowed a substantial reduction in the structured noise in fMRI residuals. Nonetheless, it does not take into account the rate-changing in heart beat that is a source of phase variation.

Stroman (2006) decomposed recorded physiological data into their constituent signals by principal component analysis (PCA) and afterwards included them in a GLM. The phases of the cardiac and respiratory cycles were different at the time of acquisition of each slice. Results of this study showed that no specific improvements were detected including respiratory regressors in the GLM and they concluded that cardiac effects are the main source of physiological noise

in spinal cord imaging. It might be that the Turbo Spin Echo sequence that they used enabled them to obtain images that were less sensitive than Gradient-Echo sequences to respiration-related susceptibility differences. This method was further optimized by Figley and Stroman (2009) with Turbo Spin Echo sequences mainly for cardiac-related noise. A database of 100 spinal fMRI datasets was analysed with and without adding the regressors in the GLM. Results obtained regressing out the cardiac-related noise showed an increase in specificity (5–6%) and sensitivity (15–20%) to neuronal activity.

Brooks et al. (2008) presented a RETROICOR-based method comprising a total of 37 regressors. They modelled the cardiac effects using the sine/cosine values of the principal frequency and the next two harmonics. The respiratory trace was instead modelled using just the fundamental and the first harmonic frequency. Moreover, additional multiplicative sine/cosine terms were added to the Fourier expansion accounting for interactions between cardiac and respiratory effects. As reported in a previous study by Friese et al. (2004), spinal EPI data might present a structured noise due to interaction of cardiac and respiratory effects. Finally, they added three further regressors to account for: CSF effects, rate and depth of breathing (RVT-Respiration Volume per unit Time) and temporal derivative of RTV (for small variations of the haemodynamic response function). All regressors were then used in the GLM included in the FSL package. Results confirmed the capability of this method to remove physiological noise. Nonetheless, as noted by the authors themselves, the inclusion of a large number of regressors in the GLM reduces statistical power for potentially limited advantages in terms of additional noise modelling. Furthermore, each regressor will not be totally independent from stimulus-derived regressors and this might affect the sensitivity to detect activations. In a paper by Deckers et al. (2006) a selective averaging filter (SAF) method is presented. The method was applied to 6 healthy volunteers to regress out cardiac and respiratory noise using Gradient-Echo EPI sequences in the brain. Performance was found to be at least equivalent to the previously published RETROICOR methods. Physiological signals are expanded in terms of a finite impulse response (FIR) basis set of the phase values (similar to what RETROICOR does with Fourier series). Imaging data are averaged according to their acquisition time relative to the nearest respiratory and cardiac event; that is all MRI data that are in the same interval of

acquisition time relative to, for example a cardiac peak or an end-inspiration, are averaged. This selective averaging results in a suppression of signals whose timing does not correlate with the event (including random noise). Recently, Kong et al. (2012) reviewed different model-based physiological noise correction techniques for spinal cord fMRI in the framework of the GLM. They applied thermal pain and punctate stimuli to elicit spinal cord activations with Gradient-Echo-based BOLD acquisitions. Results pointed out that:

- Using 32 nuisance regressors obtained modelling the cardiac and respiratory trace by the RETROICOR-like approach presented by Brooks et al. (2008) gave best results in terms of residuals after model fitting, number of activated voxels inside the cord and F-test results, if compared with the selective averaging filter (SAF) method.
- CSF regressor could explain a significant amount of unmodelled signal variance and increase activation statistics.
- Including motion correction parameters from 2D realignment as nuisance regressors increased the number of activated voxels inside the spinal cord.
- Including regressors that accounted for variations in heart beat (HR) and the rate and depth of respiration (RVT) reduced the number of activated voxels inside the cord due to non-zero correlation with the task.

It was also suggested using pre-whitening in addition to physiological noise correction in order to remove additional non-white noise from the data.

All studies quoted above confirm that there is not a standardized way in applying physiological regressors, anyway results always seem to confirm the utility of regressing out physiological noise.

5.5 - The DRIFTER software

Recently, Särkkä et al. (2012) introduced a model-based Bayesian method for estimating and removing cardiac-related and respiratory-induced effects from functional MRI images presenting it as a practical SPM8 toolbox called DRIFTER. The idea underlying this method is to separate the original signal into the following components:

1) the BOLD component (the cleaned activation-related signal) that is a slowly varying signal

2) the physiological (cardiac and respiratory) noise components that are considered as stochastic resonators with multiple harmonics

3) white noise

This separation is done for each voxel in the image and the 'cleaned' fMRI volumes can be analysed with the GLM in SPM8 software.

This method uses the interactive multiple models (IMM) algorithm to estimate frequency trajectories of physiological noise components. The estimated frequency trajectories are then used together with a Kalman Filter and RTS (Rauch-Tung-Striebel) smoother algorithms to get a separation of the fMRI signal into its aforementioned components (Särkkä et al., 2012).

This method has been tested on simulated and experimental data in the brain, and results have been compared with ones obtained using the RETROICOR method. It is shown that DRIFTER algorithm can fit the physiological data better than a RETROICOR-like method, coping with rapidly varying signals, especially in the case of time-varying amplitude and give better signal-to-noise-ratio. Nevertheless, the DRIFTER toolbox has not been tested in the spinal cord yet.

In the section 5.9, the performance of a RETROICOR-like method and of the DRIFTER algorithm are compared and discussed, but before that, let’s explain in detail how to obtain the regressors from the physiological traces recorded during the fMRI scan.

5.6 - Cardiac and respiratory slice-wise regressors

As mentioned in sections 5.2 and 5.3, most of the techniques used to deal with physiological noise account for cardiac and respiratory effects and rely on the fact that a unique cardiac and a unique respiratory phases can be associated to each slice (Glover et al., 2000). The theory relies on the assumption that any physiological process can be considered quasi-periodic, *i.e.* it is characterized by a finite number of (incommensurable) frequencies that are determined by a cardiac and a respiratory phase for each slice (Hu et al., 1995; Glover et al., 2000). The term 'phase' is used to indicate the position of a slice within a cardiac or respiratory cycle.

The cardiac phase associated to the slice acquired at the time τ is defined as:

$$\varphi_c(\tau) = 2\pi \frac{(\tau - t_1)}{(t_2 - t_1)} \qquad \text{Eq. 5.7}$$

where t_1 is the time of the R-wave peak preceding τ and t_2 is the time of the following R-wave peak. The cardiac phase varies from 0 to 2π in the interval between two subsequent R peaks and goes back to 0 with the next cardiac cycle, assigning a unique value to each slice (Fig. 5.1).

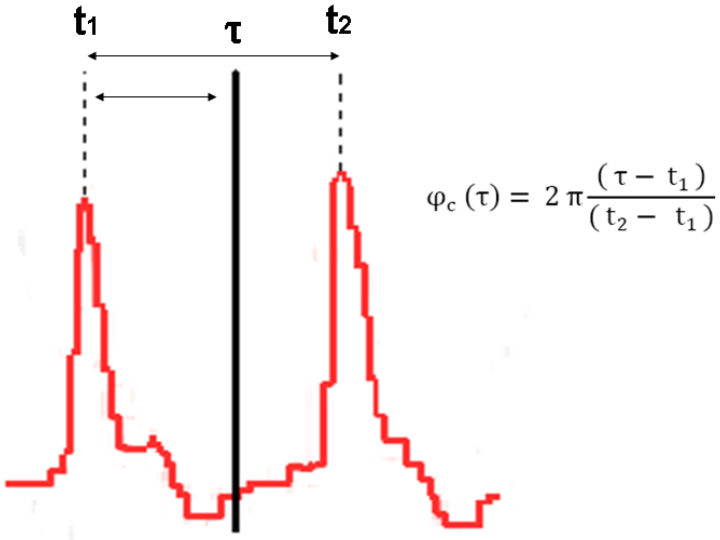

Fig. 5.1: Schematic illustration of the cardiac phase φ_c for the slice acquired at the time τ (vertical black line) between the two R-wave peaks t_1 and t_2. The cardiac trace is shown in red.

This approach was developed to deal with the cardiac component of the physiological noise and, in the early papers (Hu et al, 1995; Le and Hu, 1996), the same method was used to find the

respiratory phase as well. A few years later, Glover et al. (2000) suggested a more complex histogram-based approach to calculate respiratory phases that accounts not only for the timing of the slice acquisition during the inhalation or exhalation events, but also for the depth of breathing. If R(t) is the amplitude of the respiratory trace normalized to $(0,R_{max})$, then a histogram-equalized transfer function between R(t) and the respiratory phase $\varphi_r(t)$ can be defined as :

$$\varphi_r(\tau) = \pi \frac{\sum_{b=1}^{\text{integer}(\frac{R(\tau)}{Rmax})} H(b)}{\sum_{b=1}^{100} H(b)} \operatorname{sgn}(\frac{dR}{dt}) \qquad \text{Eq. 5.8}$$

where τ indicates the time corresponding to the acquisition of the slice, the term 'sgn $(\frac{dR}{dt})$' is the sign function distinguishing inspiration (dR/dt > 0) from expiration (dR/dt < 0) and 'H(b)' indicates a histogram that considers the amplitude of the respiratory trace and each of the 100 bins that the interval $(0,R_{max})$ is divided into. The term 'integer $(\frac{R(\tau)}{Rmax})$' on the numerator of Eq. 5.8 stands for an integer-rounding operation.

Let's now refer to Fig. 5.2 and let's describe in more detail the steps that need to be done for obtaining the respiratory phases. The respiratory trace needs to be recorded during the whole experiment and the time corresponding to each slice acquisition must be evaluated from the traces of the gradients that are recorded as well and included in the physiological file (for more details about the physiological file, see section 5.8). The respiratory trace needs then to be normalized and the interval $(0,R_{max})$ is divided into 100 regular intervals (bins). A histogram H(b) can now be created. The b-th bar of this histogram contains the number of recorded points of the respiratory trace that are included in the b-th bin. In Fig. 5.2 the recorded points of the respiratory trace corresponding to the b-th bin are shown in red and indicated by red arrows. This picture shows also a slice that was acquired at the time τ, while the respiratory trace had an amplitude that was included in the b-th bin. The respiratory phase $\varphi_r(\tau)$ corresponding to this slice can be calculated summing up all the bars of the histogram H(b) up to the bin

corresponding to the acquisition time of the slice, and then dividing by the sum of all histogram values (Fig. 5.3).

This ratio indicates a phase varying from 0 to π whose sign depends on the inspiratory (+) or expiratory (-) modality of the subjects' breathing at the time τ.

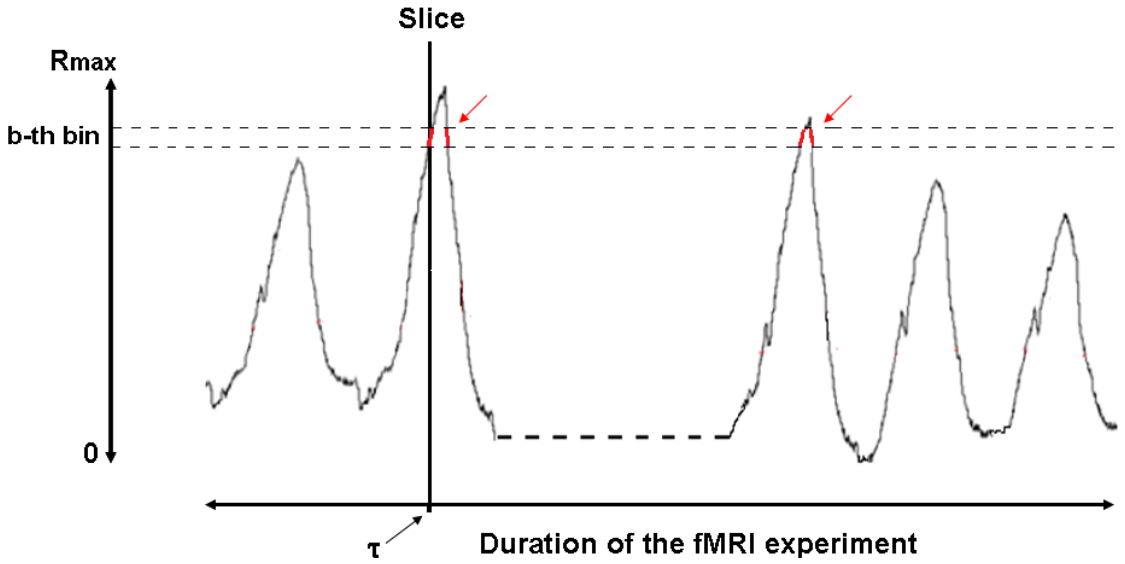

Fig. 5.2: Schematic illustration explaining how to obtain the H(b) histogram. Respiratory peaks, slice acquired at the time τ and normalised respiratory amplitude are depicted. The recorded points of the respiratory trace corresponding to the b-th bin are shown in red and indicated by red arrows.

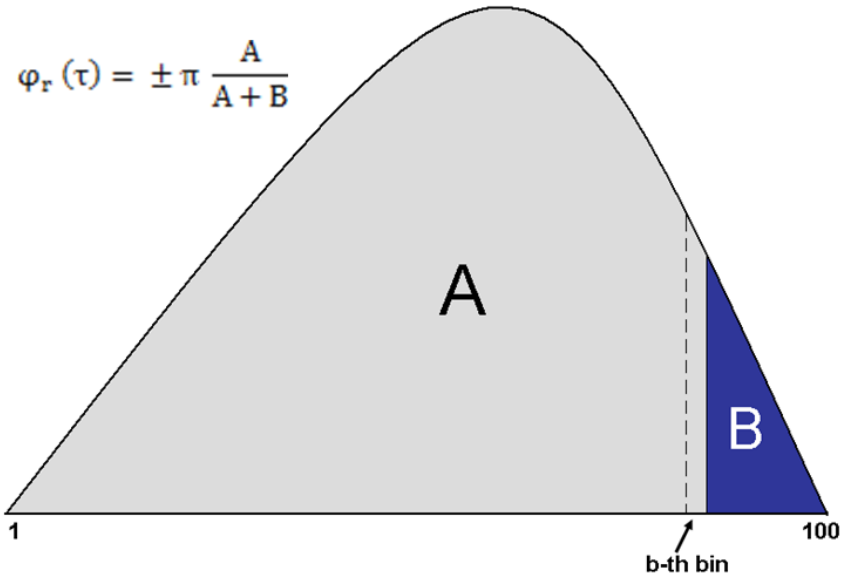

Fig. 5.3: Schematic illustration of the histogram H(b). The respiratory phase of the slice acquired at the time corresponding to the b-th bin can be represented as the ratio between two regions of the histogram, as indicated in the formula reported in the picture.

Once that both $\varphi_c(\tau)$ and $\varphi_r(\tau)$ have been calculated for the slice, the physiological noise '$Y(t)_{\mathbf{Phys}}$' can be expanded in terms of a low-order Fourier series:

$$Y(t)_{\mathbf{Phys}} = \sum_{m=1}^{M} \left(a_m^c \cos(m\,\varphi_c) + b_m^c \sin(m\,\varphi_c) + a_m^r \cos(m\,\varphi_r) + b_m^r \sin(m\,\varphi_r) \right)$$

Eq. 5.9

where M is the number of harmonics used in the series and the indices c and r indicate the cardiac and respiratory components. Glover et al. (2000) reported that it is not useful to take M>2. To summarize, using the physiological data, accurately recorded in synchrony with the fMRI scan, it is possible to regress out cardiac and respiratory noise by including the corresponding slice-wise regressors in the GLM.

5.7 - The CSF regressor

I added also a CSF regressor in the GLM as the number of false positives can be further reduced implementing a regressor that accounts for noise arising from CSF pulsatility (Brooks et al., 2008; Cohen-Adad and Wheeler-Kingshott, 2014). A CSF mask was drawn using FSLview on the mean image obtained from the realigned volumes of each dataset and then applied to all realigned volumes. Custom-made MATLAB codes were then used to extract mean values of the CSF time course to use as the CSF regressors. Each mask was accurately drawn in order to include only voxels that were deemed CSF. In the count of activated voxels, only those in the spinal cord within the CSF mask were taken into account.

5.8 - How to obtain the cardiac and respiratory regressors from the physiological traces

Once downloaded, the physiological file (called 'SCANPHYSLOG.log') can be read so that the columns corresponding to the cardiac and the respiratory traces are plotted using MATLAB (Fig. 5.4) together with the traces corresponding to the 3 gradients waveforms (Gx, Gy, Gz).

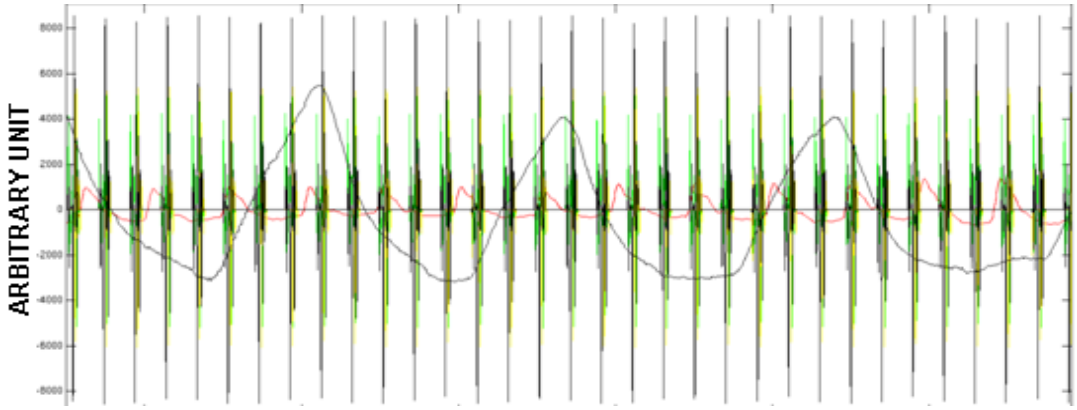

Fig. 5.4: Example of plot of the physiological file downloaded from the scanner showing the patterns of the gradients (vertical lines in green and black) and the physiological traces (the black curve is the respiratory trace and the red one, smaller, is the cardiac trace; see Fig. 5.6).

Every 2msec a point is acquired (500 Hz is the sampling frequency) and when the three gradients work simultaneously a slice is acquired in about 140ms. All the slices are featured by the same pattern that is due to the gradients (Fig. 5.5).

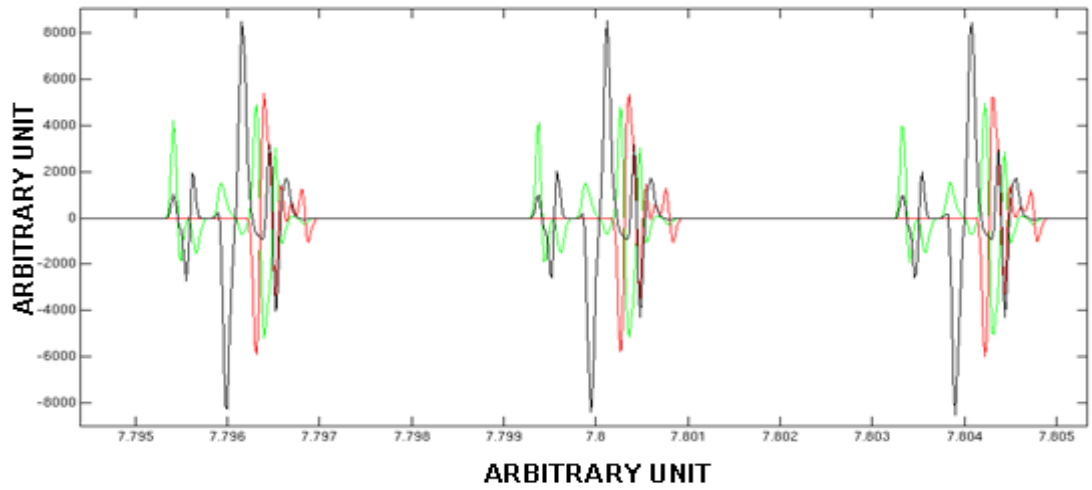

Fig. 5.5: Plot of the traces of the gradients during the acquisition of 3 slices. Different colours are used for each gradient (G_x in green, G_y in red, G_z in black).

Plotting the traces is important in order to check out if they are correctly recorded as it is essential for modelling physiological noise. Good traces look quite regular, with heart rate varying from 50 to 70 beats per minute and the average respiratory cycle taking between 3 and 4 seconds (depending on the subject). If movement-related peaks or sudden spikes appear in the traces (Fig. 5.6), it might be a good idea to apply one of the following suggestions.

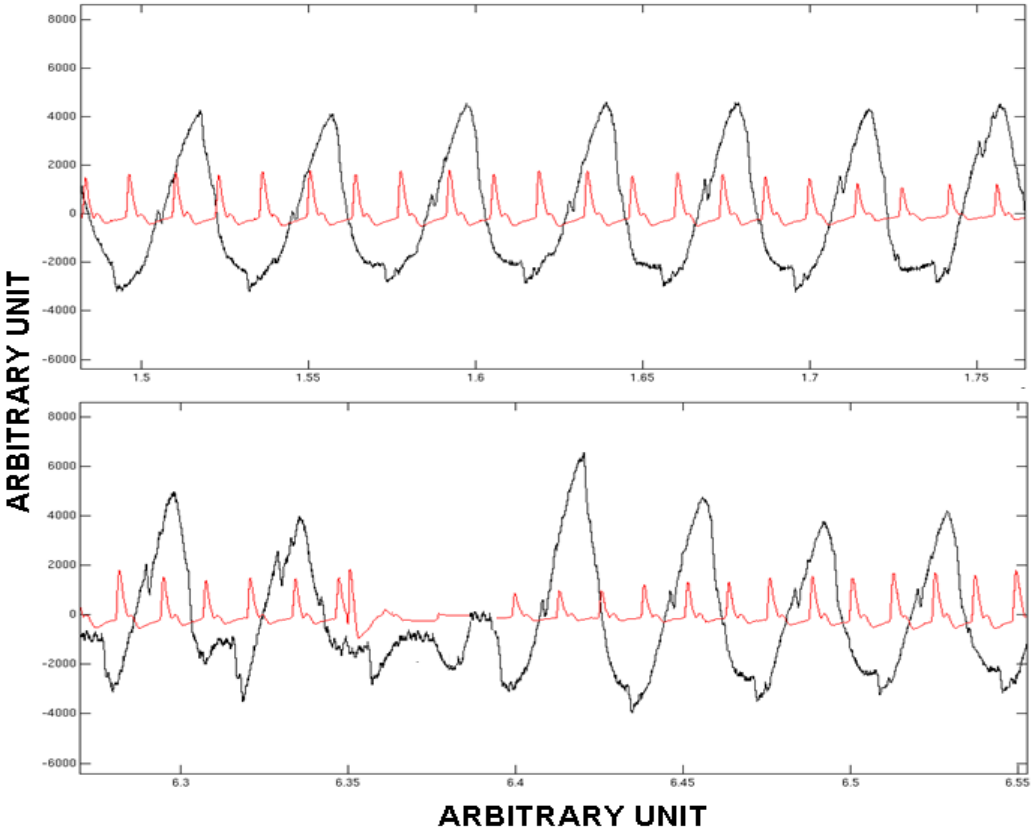

Fig. 5.6: Plots of the cardiac (in red) and respiratory (in black) traces from the physiological file downloaded from the scanner. Regular recording is displayed in the figure at the top and irregular recording is shown in the figure at the bottom.

Firstly, some sort of smoothing to the data might be used. For instance, I have applied the Savitzky-Golay filter (sliding polynomial fit) using the MATLAB function 'sgolayfilt' and results were good. A Savitzky-Golay filter (Savitzky and Golay, 1964) minimizes the least-squares error in fitting a polynomial to frames of data, preserving the shape of the peaks. A local polynomial regression around each point is performed and a new smoothed value replaces each data point. The Savitzky-Golay filter was successfully employed by Glover et al. (2000) as well.

Secondly, one can tweak the parameters in the toolbox. The dynamic noise spectral densities for the IMM model can help the signal adopting, and the drift term noise dynamics parameter can account for movement drift.

Lastly, one can try to tweak the noisy parts of the reference signal manually, because the frequency estimate at those points will not play any major role. However, the fMRI data will probably be bad too if the subject has been moving a lot at some point of the recording. Thus, as a rule of thumb, in case an adjustment to the traces is required: on one side, I would make sure that the reference signal is of some quality (smoothing or tweaking), and on the other, I would modify the DRIFTER parameters to better account for the case.

Recording of physiological traces must be synchronized to the acquisition of the images in such a way to be able to determine when, within the scanning session, a certain slice has been acquired. It is useful to monitor live the traces while the scanner is working in order to stop it whenever something goes wrong with the recording and to restart to scan after fixing the issue.

Going through the traces it is clear that the slices start to be acquired after the initial warming up of the gradients (that are recorded as well) and the dummy scans. Every single pulse from the scanner is recorded, it does not matter what it is, and looking at the trace it is not straightforward to determinate when the first slice in the first volume is acquired.

Noticing that the scanner stops immediately after the acquisition of the last slice (in the last volume), it is better to start counting the slices backward from the very last one. In the sequence I used, 9 slices and 200 volumes were acquired, corresponding to a total of 1800 slices. Each slice was counted using a custom-made mat-file that spotted the maximum of the Gz gradient (Fig. 5.5) occurring always at the same time within the interval (about 140 ms) during which the slice was acquired (*i.e.* about in the middle of it, although different choices are acceptable).

A cardiac regressor relies on the detection of the heart peaks within the cardiac trace and on the possibility to locate the acquisition of each slice within the corresponding heart cycle. Working with well-shaped peaks makes things easier, otherwise it is possible to smooth the trace in an appropriate way. However, if the cardiac trace is irreparably corrupted, for example due to abrupt movements of the subject's hand/finger, the cardiac information concerning the slices acquired during the 'corrupted' time interval is lost. DRIFTER software instead, is more

flexible due to the fact that its algorithm is based on cardiac frequency-detection and thus the accurate peak-detection of any RETROICOR-like method is no more required.

Analogous considerations stand for the respiratory trace.

Following the information from Glover's paper (2000), I created MATLAB codes based on the steps below:

1) Plotting the cardiac trace and checking it visually

2) Smoothing the trace in order to make peak detection easier

3) Applying Eq. 5.7

4) Collecting sines of the calculated cardiac phases into a column and cosines into another

5) Collecting sines and cosines concerning the second harmonic in the same way

The resulting columns are the regressors we were looking for, ready to be entered into the GLM. Referring to cardiac noise and considering the matrix expression of the GLM (Eq. 5.5) each slice is associated with a column of cosines and one of sines for each harmonic of the Fourier expansion that is applied. If the terms up to the second order are considered, it results into 4 columns of regressors for each slice. In the GLM one can fit as many lines as the number N of volumes and thus each regressor must have N lines, however, regressors concerning different slices can be used simultaneously in the GLM without interfering with each other in case they are orthogonal. Usually this is not a big issue, however, orthogonality between vectors may be checked with SPM and, if needed, obtained with MATLAB.

Similar considerations stand for respiratory phases that, although obtained by a different procedure and applying Eq. 5.8 instead of Eq. 5.7, yield analogous regressors made up of N

lines each and containing cosines and sines of the respiratory phases up to the desired term of the Fourier expansion.

Nevertheless, as reported by Brooks et al. (2008), including a large number of terms in the GLM reduces the degrees of freedom that is reflected by a reduced statistical power without significant gain in terms of noise modelling.

5.9 - Performance of the different methods

5.9.1 - Purpose

To investigate the application of physiological denoising on three fMRI spinal datasets.

5.9.2 - Materials and Methods

Cardiac and respiratory traces were recorded during each fMRI scan using a pulse oximeter applied on the index finger (of the resting hand) and a respiratory belt fastened around the abdomen of the subject. Sequence and imaging parameters have already been described in section 2.8. A sensory stimulus was delivered over the palmar surface of the thenar eminence of the left hand (C6 dermatome; see Fig. 3.1) using a custom made MR-compatible electric rotating brush (see section 7.2 for more details). The block design comprised 10 epochs of rest alternating with 10 epochs of stimulation, lasting 36 seconds each (see section 2.8). The 9 slices were prescribed transverse to the cord and the central slice was always placed in the middle of the C6 spinal segment (Fig. 5.7), however, due to specificity of the stimulated dermatome, only the 6 central slices have been analysed for each volunteer (see section 7.2 for more details). 2D-realignment was applied to all datasets and a CSF regressor was always added in the GLM included in SPM8. Results were obtained with $p<0.01$ (uncorrected) threshold.

Three different methods were tested:

1) Including cardiac and respiratory slice-wise regressors (RETROICOR method) in the GLM

2) Including the cardiac and respiratory traces in the DRIFTER software

3) Applying neither DRIFTER software nor the RETROICOR method to the data

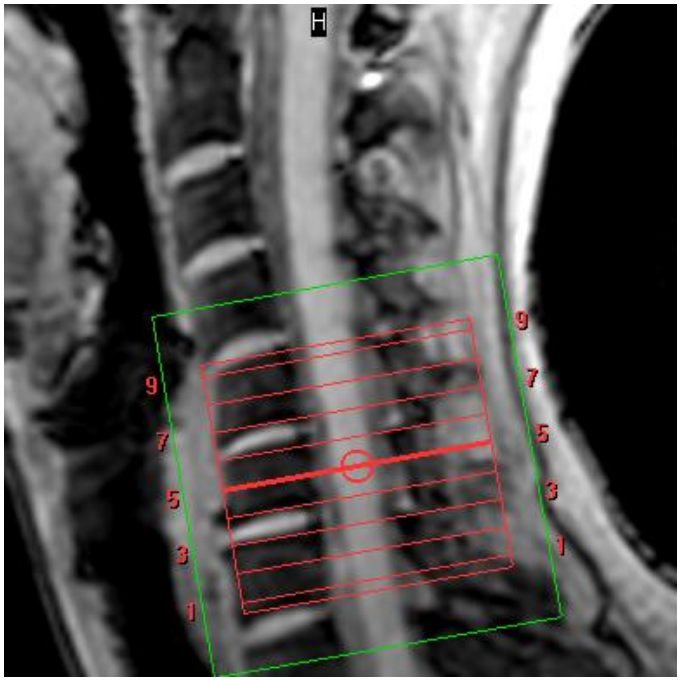

Fig. 5.7: Localization of the slices. Only activations localized in the 6 central slices (from slice 3 to slice 8) covering the whole C6 segment were considered.

In 2), realignment has been applied after applying DRIFTER software. As suggested in previous studies (Birn et al., 2006; Brooks et al, 2008; Cohen-Adad et al., 2010), the best correction increases significance of activations, reflecting the best fit of the model to the experimental data and reducing the physiological variance of the residuals.

5.9.3 - Results

Results are reported in Fig. 5.8. When no physiological correction was applied to the data, random activations were found outside the SC, especially in the CSF (subjects 1 and 3). Only in one case (in slice 7 for subject 3), one activated voxel was detected within the SC. For one subject (subject 2), activated voxels were detected neither inside nor outside the SC. For all subjects, applying physiological corrections increased the number of activated voxels within the SC and decreased the number of activated voxels outside the SC. A larger number of activated voxels inside the SC was detected for all subjects using DRIFTER software. Activations were found both ipsilaterally and contralaterally for both the DRIFTER and RETROICOR methods. The activated voxels, obtained with the two methods, never overlapped except for 1 case (in slice 8 for subject 3). For all subjects, the t-values of the activated voxels detected with the two correction methods were comparable. However, for all subjects, the t-values obtained using DRIFTER software were slightly bigger, on average, than those obtained using the RETROICOR method (about 5%).

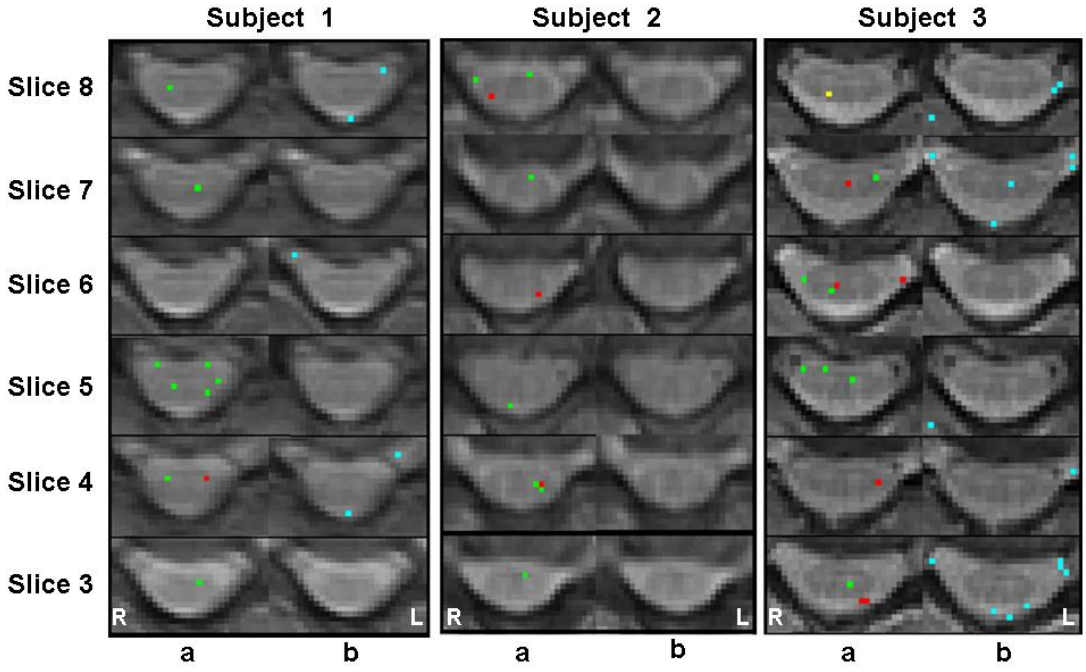

Fig. 5.8: Activations in the 3 subjects obtained using the RETROICOR method (a; in red) and the DRIFTER software (a; in green) corrections. Yellow voxels (a) indicate overlapping between results obtained with the two different approaches. Activations obtained without applying any physiological correction are displayed for each subject as well (b; in light-blue). Activations are overlaid on the mean image. Slice numbers refer to Fig. 5.7.

5.9.4 - Conclusion and Discussion

The following criteria were used to evaluate the outcome:

1- number of activated voxels detected within and outside the SC;

2- laterality of neural activity;

3- t-values of the activated voxels within the SC.

The worst results were obtained without applying any physiological correction. No reliable neural activity was detected for any subject because activated voxels were always located outside the SC (except for 1 voxel in slice 7 for subject 3). Results obtained using the DRIFTER software were better than those obtained with the RETROICOR method.

Using DRIFTER a larger number of activated voxels inside the SC and a smaller number outside the SC were found. Assuming that activated voxels outside the SC are false positives, the reduction of their number corresponds to a reduction of false positives. Moreover, an increase of the number of activated voxels detected inside the SC, induce to think that DRIFTER software allowed the detection of neural activity better than the RETROICOR method.

Let's now discuss about variability of neural activity detected applying the two different physiological denoising methods. Activated voxels obtained with the 2 methods never overlapped (except for 1 voxel in slice 8 for subject 3), although in a few cases the activated voxels detected with the 2 methods were neighbouring or very close. However, bearing in mind that we are comparing single voxels locations and not large clusters of activation as it is done in the brain, we can deem that regions of neural activity were spotted using both the methods.

Nonetheless, several activated voxels detected with the two methods were located in different regions of the SC, both ipsilaterally and contralaterally. Using both the methods, however, a larger ipsi- than contra-lateral activity was found for all subjects, as it was expected. About the reliability of a single activated voxel instead, we cannot draw any definitive conclusion due to the fact that, in different subjects, the spinal nerves may enter the spinal cord in slightly different areas (within the same vertebral segment) due to slight anatomical differences between the subjects (Standring et al., 2005). Lastly, higher (on average) t-values for the activated voxels

obtained using DRIFTER were evaluated, indicating a better fit of the model to the experimental data.

To conclude, results suggest that DRIFTER software might be better than the RETROICOR method for reducing physiological noise.

However, it must be noted that in the paper where the DRIFTER software is introduced (Särkkä et al., 2012), DRIFTER performance is tested on just one brain and no realignment is applied to the images. In Särkkä's paper, images are not registered and this might not be a serious issue in the brain, considering that the extent of the activation areas is usually much bigger than one or two voxel-width (there might be any issues with activated voxels that lie on the edge of the activated areas). In the spine instead, just a few voxels are activated and realignment is recommended. A questionable issue might be whether to realign before or after applying DRIFTER software. Realignment 'destroys' information contained in the data due to linear interpolation and so it might be better to realign after filtering. Conversely, supposing that the images move forward by one voxel width, temporal filtering on the original data might cause large signal change due to movement filtered out. The contrast that should have been used for motion correction has been changed. I decided to apply DRIFTER before realigning because I calculated that, analysing images in this way, the temporal standard deviation was always reduced. However, from a critical point of view, the importance of being able to model a physiological signal is that when you have a regressor or filter that hopefully captures the temporal dynamics of the phenomenon, it will pull out even the bit of noise that was added to a voxel time-course during motion correction.

5.10 - The analysis pipeline

After having tested different kinds of preprocessing steps, I optimized the analysis pipeline for functional datasets in the spinal cord. This pipeline was applied to all the functional studies presented in the following chapters of this thesis.

This pipeline can be summarized as follows:

1) Applying DRIFTER software to clean up the signal from cardiac and respiratory related noise on the fMRI time series

2) Applying 2D slice-wise realignment with FSL software to the output of DRIFTER

3) Drawing a CSF mask on the mean image and applying this mask to all the realigned volumes in the dataset, aiming at obtaining a CSF regressor

4) Performing statistical analysis with SPM8 using p=0.01(uncorrected) threshold and including in the GLM both CSF regressor and movement regressors (3 for each slice which is considered).

MATLAB files were created for developing and optimizing each of the previous steps.

5.11.1 - Literature upon test-retest reliability

In the literature, many spinal functional studies use different motor and sensory tasks and perform different data analyses to infer neural activation. However, there is still an important issue that hasn't been dealt with in an adequate way: reproducibility of functional activations.

Repeated studies give information about the extent at which two measurements are in agreement and quantify how reliable results are. They are performed to assess the variability of measures, aiming at investigating the feasibility of a method or technique.

Although there are several papers mentioning low reproducibility in terms of both amplitude and location of BOLD signal (Backes et al., 2001; Brooks et al., 2008; Giove et al., 2004; Govers et al., 2007; Stroman, 2005; Wheeler-Kingshott et al., 2013; Zhao et al., 2008), to date, the literature lacks reporting test-retest reliability results. As a general rule, it would be really useful if research groups would produce information about reproducibility of their methods because this would promote faster progress in functional MRI in the spine. Although it is not possible to claim exactly the same pattern of activation for different subjects, due to the fact that nerve roots and dermatomes too can vary from subject to subject (Standring et al., 2005), one would expect to find consistent areas of neuronal activity within the spinal cord of the same subject undertaking the same exam twice under the same conditions.

In functional studies in the brain, reproducibility has been investigated and reported in many papers but results, depending on the task and brain region, are still controversial. Just to quote a few of them, Vul et al. (2009) stated that brain fMRI results have a reliability around 0.7, Lieberman and al. (2009) around 0.9 and Jabbi et al. (2009) wrote that it could be as high as 0.98. Other studies were more critical about this topic instead. Duncan et al. (2009) reported that the percentage of overlapping between activated voxels in 45 volunteers scanned twice, varies between 25% and 65% depending on the statistical threshold used.

Brannen et al. (2001) reported an overlapping of only 37% of activated voxels (phonologic generation task) and Rutten et al. (2002) reported even slower percentage of common voxels performing a verb generation (24%) and a naming task (21%).

Spinal fMRI reproducibility has not been addressed in the literature. In my experience, it is a quite troublesome topic of conversation as well and, for most researchers, it is not clear how reliable their results are. Low reliability is basically due to difficulty in distinguishing true task-related neural activations from noise.

Only two spinal fMRI papers mention the reproducibility of their study. As a metric of spinal fMRI activation, Bouwman et al. (2008) measured the amplitude of BOLD signal change, Stroman et al. (2005a) instead, visually checked the activated areas in the spine (although with arguable results). These two different approaches aimed at investigating different aspects of reproducibility, depending on the variability over time of a certain feature. Recent work (in the brain) showed that activation volume is a more robust measure than BOLD signal change as a metric for neuronal activation (Bhattacharyya et al., 2014) and I opted to test the reproducibility of spinal fMRI following this approach.

5.11.2 - Methods to evaluate test-retest reliability

To quantify neuronal activity (in the brain), two common metrics are the Dice coefficient and the Jaccard index. Their main limitation is the high dependence on the statistical threshold used in the analysis (Duncan et al., 2009). For both the metrics: the value 1 corresponds to a total overlapping of the activated areas in the first and second scans and the value 0 to a total separation of the activated areas in the two scans.

The Dice coefficient is given by:

$$\mathbf{R}_{\mathrm{Dice}} = 2\,\frac{\mathrm{V}_{\mathrm{overlap}}}{\mathrm{V}_1 + \mathrm{V}_2} \qquad \text{Eq. 5.10}$$

and the Jaccard index is calculated as:

$$\mathbf{R}_{\text{Jaccard}} = \frac{V_{\text{overlap}}}{V_1 + V_2 - V_{\text{overlap}}} \qquad \text{Eq. 5.11}$$

Where V_{overlap} indicates the overlapping cluster and V_1 and V_2 stand for the clusters that are activated during the first and the second scan.

The Dice coefficient can be imagined as the number of overlapping voxels divided by the average number of activated voxels across both sessions.

The Jaccard index instead, gives the percent of the total number of activated voxels that are shared between the two scans. These methods rely on the exact overlapping of clusters of activation, but in the spinal cord this approach seems to be too conservative due to the fact that only a few voxels are usually activated. Although smoothing the images might enhance the reproducibility of a study, drawbacks in terms of loss of spatial specificity would be important to consider (see section 4.3).

A further method of reproducibility, used only in the first papers (in the brain) but then disregarded, was counting the total number of significant voxels in the first and the second scans. A misleading event would be that different activated areas might produce the same number of activated voxels (Cohen et DuBois, 1999). As a matter of curiosity, I report that Bennet and Miller (2010), reviewing the literature about cognitive tasks (the less reproducible ones in the brain), found an average cluster overlap of 29%, corresponding to $\mathbf{R}_{\text{Dice}}$=0.45 and $\mathbf{R}_{\text{Jaccard}}$=0.29.

Regrettably, so far there is no overview of functional reliability in the spine and so researchers do not know what to expect from it, therefore my contribution to the field has been to assess the single subject reproducibility in a small pilot study.

5.12 - Test-retest reliability study

5.12.1 - Purpose

The purpose of this study was to discuss the localization of those voxels that showed activation (p=0.01, uncorrected) in both the first and the second scans. Results from a test-retest reliability study involving 3 healthy volunteers scanned twice are reported.

5.12.2 - Materials and Methods

The first and the second scans were performed on each volunteer in different days. A localized sensory stimulus was delivered using an MR-compatible custom-built rotating brush and applied to the C6 dermatome over the palmar surface of the thenar eminence of the left hand. Sequence and imaging parameters have already been described in section 2.8. The 9 slices were prescribed transverse to the cord and the central slice was always placed in the middle of the C6 spinal segment (Fig. 5.7). Only the six central slices were analysed for each volunteer (see section 7.2). Physiological traces were recorded and the analysis pipeline described in section 5.10 was applied.

For each subject, due to the very limited number of activated voxels per slice, it is more practical and reliable to visually compare the activations between the two scans instead of using the Dice coefficient or the Jaccard index that are supposed to evaluate any overlaps between blobs of activation. It should be reminded that in the brain thousands of voxels are taken into account, within the spinal cord instead, there are about 70 voxels per slice.

Due to the issues mentioned before, counting only overlapping clusters of activation seemed to be a too restrictive approach and thus I opted to compare, for each subject, the activated voxels included in each hemicord.

5.12.3 - Results

Activations were found inside the spinal cord in all subjects and, in particular, each subject presented a similar ipsilateral activity in the slice 5 during both the first and the second scans (Fig. 5.9). It is worth mentioning that this slice was acquired in the middle of C6 segment (Fig. 5.7). Comparing the test and re-test scans of each subject, other quite similar activations can be individuated:

1) Subject 1: in the slices 3 and 4 (contralaterally), in the slice 8 (ipsilaterally)

2) Subject 2: in the slices 4 and 7 (contralaterally)

3) Subject 3: in the slices 4 and 8 (ipsilaterally), in the slices 3 and 7 (contralaterally)

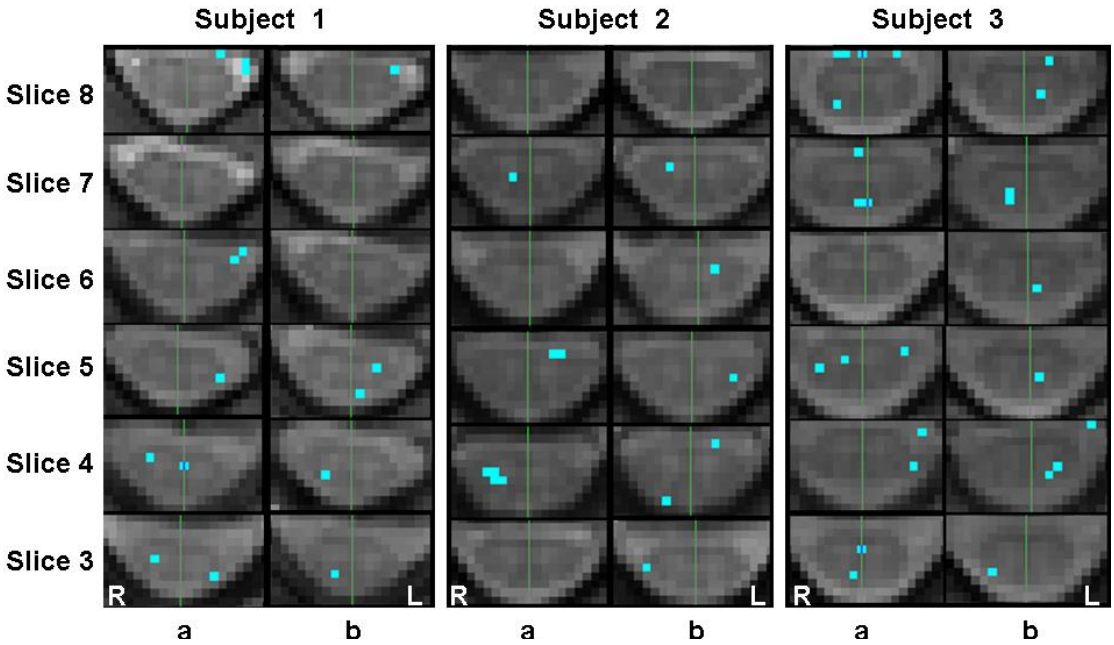

Fig. 5.9: Activated voxels found in the 3 subjects during the first (a) and the second (b) scans. Left and right hemicords are divided by a central line. In subject 1 (a) two voxels in the slice 8 and one in the slice 6 are deemed in the CSF. In subject 3 (a and b) one voxel in the slice 4 is deemed in the CSF. Slice numbers refer to Fig. 5.7.

5.12.4 - Conclusion and Discussion

To summarize, although it is not easy to quantify the reproducibility of a functional study performed in the spinal cord, results from this study showed a few interesting conclusions:

1) For each subject, common patterns of activation were found both ipsilaterally and contralaterally during the test and re-test scans.

2) Ipsilateral activity was confirmed in the middle of C6 segment in all the subjects.

CHAPTER 6 - HAEMODYNAMIC RESPONSE FUNCTION(s)

Introduction

The relationship between local neural activity and subsequent changes in the blood flow is called neurovascular coupling (NC). Apart from the technical issues (susceptibily artefacts, low signal, physiological movements, lack of dedicated software), NC also may be a factor contributing to reduce sensitivity to detect neuronal changes task related. The magnitude, extension and localization of blood flow changes depend on changes in neural activity through a complex sequence of events associated with both neurons and vascularity. Functional MRI is a vascular-based technique that relies on the NC to infer neural activity and modelling neural activity in different ways might lead to different results. So far, there are not so many studies investigating this issue, however, there are a few works that might suggest the need for a deeper investigation about NC in the spine.

In this chapter, importance of Haemodynamic Response Function (HRF) is explained in detail and a HRF, different from that commonly used in both the brain and spine, is tested.

6.1 - Neurovascular coupling as a confound in fMRI

The physiological process that triggers signal changes linked to neural activity (Logothetis and Wandell, 2004) presents the same features in the brain and the spine (Giove et al., 2004; Stroman, 2005). However, neurovascular coupling (NC) in the spinal cord might differ from the brain, due to differences in vascularity that might give rise to different blood flow, different blood volume and different oxygen supply, resulting in a different functional response. The exact features of functional response are still unclear. Marcus et al. (1977) reported that measurements of spinal cord flow in dogs, sheep and lambs showed blood flow to the cervical and lumbosacral spinal segments to be 40% higher than flow to the thoracic cord. Futhermore, a local blood flow enhancement around 50% was detected in the ipsilateral grey matter while no significant changes in blood flow were detected neither in the white matter nor in the contralateral side. The localization of the spinal vascular response was confirmed in rats too (Brieu et al., 2010). Nix et al. (1976) reported that the vascular response in the cord in rats was 'brisker' than in the brain, while the responses to hypoxia were similar. From all these studies it can be inferred that physiological regulation of blood flow in the brain and in the spine might be only qualitatively similar to each other and a deeper investigation would be required. Furthermore, it is well known that functional response depends on factors such as age (Richter and Richter, 2003) and vascular health (D'Esposito et al., 2003). Coffee consumption implies vascular changes too, being caffeine a vasoconstrictor (Chen and Parrish, 2009). Moreover, neurovascular coupling can also depend on the duration of the performed task. In fact, due to habituation, there is a decrease in neural firing although the coupling mechanism doesn't change (Bandettini et al., 1997). Generally, being fMRI an indirect effect of neural activity, effects should be compared between different groups only if the NC can be considered identical across those groups. On the other hand, difference between responses may reflect differences in NC or oxygen consumption rather than in neuronal activity (Reynell and Harris, 2013).

6.2 - The Haemodynamic Response Function

Literature about the SEEP effect in the spinal cord is very limited, hence this section focuses on the BOLD effect. As already discussed in chapter 3, during neural activity there is an increase in oxygen and nutrients demand supplied by the blood flow. This delivery of blood, named Haemodynamic Response (HR), can be modelled using a function called Haemodynamic Response Function (HRF). Generally, in standard fMRI analysis, a model is fitted to the data in order to detect the effect we are interested in, for example, the task that has been performed. The aim of statistical analysis is to identify those voxels whose time-varying signal matches the predicted response, obtained convolving the HRF with the predicted neural activity. The HRF can be evaluated from event-related experiments (Josephs et al., 1997; Friston et al., 1998) and the predicted neural activity is usually a boxcar function that equals zero over the resting periods. The convolution, assumed to be linear and time-invariant, is the transformation that mediates between neural firing and BOLD response and constitutes the cornerstone for inferring neural activity using the GLM (see section 5.1).

In a nutshell, the vascular system can be depicted as a kind of 'machine' that has neural activation as input and the corresponding BOLD response B(t) as output. Considering neural activity featured by a stimulus function $s_j(t)$ (with each j indicating a single stimulus), we can write:

$$B\,[s_1(t) + s_2(t)] = B\,[s_1(t)] + B\,[s_2(t)] \qquad \text{Eq. 6.1}$$

Due to the linearity, the BOLD response can be expressed as:

$$B(t) = \int_0^t s(t-\tau)\, h(t)\, d\tau \qquad \text{Eq. 6.2}$$

Eq. 6.2 is a convolution integral that characterizes the BOLD response in the linear and time-invariant assumptions. The function h(t) is the aforementioned HRF representing the BOLD

response elicited by neural activity. Let's now consider a more rigorous mathematical approach that allows us to explain the fMRI response in terms of the GLM.

Let us now consider another equation, that follows from Eq. 6.2 (Josephs et al., 1997):

$$y_i(t) = \int_0^t s(t-\tau)\, h_i(t)\, d\tau + e_i(t) = s(t) * h_i(t) + e_i(t) \qquad \text{Eq. 6.3}$$

Eq. 6.3 explains that, taking a single voxel within the spine, the response $y_i(t)$ in that voxel is given by the convolution of the stimulus function s(t) with a specific HRF that is indicated by $h_i(t)$, plus a residual $e_i(t)$ that includes any other source of variability in the signal in that voxel. Let's write $h_i(t)$ in terms of a basis function expansion:

$$h_i(t) = \sum_{b=1}^{N} x_b(t)\beta_{i,b} \qquad \text{Eq. 6.4}$$

where N is the number of the $x_b(t)$ functions and $\beta_{i,b}$ are the weighting coefficients.

Eq. 6.3 and Eq. 6.4 can be combined and it yields:

$$y_i(t) = \sum_{b=1}^{N} \left(\int_0^t s(t-\tau)\, x_b(t) d\tau \right) \beta_{i,b} + e_i(t) \qquad \text{Eq. 6.5}$$

that is the result we were looking for, *i.e.* the BOLD effect expressed in terms of a GLM. To show it in the common matrix form, let's substitute into eq. 6.5 the stimulus function s(t) that can be any generic function of time, for example, considering a delta-like function it results:

$$y_i(t) = \sum_{b=1}^{N} x_b(t)\, \beta_{i,b} + e_i(t) \qquad \text{Eq. 6.6}$$

that corresponds to the following matrix for the GLM:

$$\mathbf{Y} = \mathbf{X}\boldsymbol{\beta} + \mathbf{e} \qquad \text{Eq. 6.7}$$

Eq. 6.7 has already been dealt with in section 5.1.

The choice of an appropriate HRF is important because the right model would correctly predict the outcome of the experiment, a wrong one instead would lead to misleading results. The theory relies on the assumptions that the functional BOLD response changes slowly compared with the neural activity that drives it and that the signal increases with the enhancement of the ratio oxy-/deoxy- haemoglobin (Friston et al., 2006). In the brain, the canonical HRF is usually used and the parameters that model it have been experimentally evaluated using event-related designs (Josephs et al., 1997). After a small initial dip lasting 1-2 sec (not always detected), the canonical HRF reaches its maximum about 6 seconds after the onset of the stimulation (Buxton, 2001; Lindauer et al, 2001). When the oxygen surplus is no more needed, blood flow returns slowly to the baseline with a characteristic undershoot.

However, in the literature there are several papers reporting that the BOLD signal in the brain can vary between subjects and even within the same subject when anatomically different areas are involved in neuronal activity (Aguirre et al., 1998; Huettel and McCarthy, 2001; Handwerker et al., 2004; Ances et al., 2008). There are a few examples of parametric functions with a plausible shape (Boynton et al., 1996; Clark et al., 1998; Cohen, 1997; Dale and Buckner, 1997; Friston et al., 2006) whose parameters can be chosen in such a way to adjust the HRF according to specific brain regions. Nevertheless, the canonical HRF (implemented for example in the matfile 'spm_hrf.m' in the SPM toolbox) is usually employed. The literature on spinal fMRI is much more limited than that in the brain and spinal studies are usually performed using the canonical HRF (Fig. 6.1). This HRF is a two-gamma parametric function that can be written in the following mathematical form:

$$h(t) = \left(\frac{t}{d_1}\right)^{a_1} e^{-\left[\frac{t-d_1}{b_1}\right]} - \frac{1}{c}\left(\frac{t}{d_2}\right)^{a_2} e^{-\left[\frac{t-d_2}{b_2}\right]} \qquad \text{Eq. 6.8}$$

with 0<t<T. In Eq. 6.8 there are two contributions: the first one models the peak that is reached in the time $d_1 = a_1 + b_1$, and the other models the delay of the undershoot with $d_2 = a_2 + b_2$.

In the SPM software the following default parameters are used:

$a_1 = 6$, delay of response relative to onset (in seconds);

$a_2 = 16$, delay of undershoot relative to onset (in seconds);

$b_1 = 1$, dispersion of response;

$b_2 = 1$, dispersion of undershoot;

$c = 6$, ratio of response to undershoot;

And the length of the HRF is set to 32 seconds since the onset.

6.3 - The spinal HRF

In the literature, only a few papers report an estimate of a HRF suited for the spinal cord (Stroman and Ryner, 2001b; Brown et al., 2007; Giulietti et al. 2008).

Stroman and Ryner (2001b) found that in the cervical spinal cord the functional response is slower than in the brain. They reported that the maximum was attained between 20-30sec using a motor and proprioceptive task (squeezing ball) and after 15sec from the onset using a sensory stimulus (repeated air-puffs).

Brown et al. (2007) used both a thermal nociceptive stimulus and a motor stimulus (fist clenching) to evaluate the HRF and optimize their functional protocol. Using the thermal stimulus they could not obtain clear results and they did not report any parameters. Using the motor task instead, they reported: a time to response peak of 8sec, a time to undershoot peak of

25 sec and a ratio of response to undershoot of 6sec. The length of the HRF is shown to be approximately 30 seconds since the onset.

Giulietti et al. (2008) assessed the linearity of the response for motor stimuli (squeezing ball) lasting from 15 to 42 sec and reported that the peak of the signal was attained after 9sec from the onset. Furthermore, they found a ratio of response to undershoot of 8.7 and they reported that 30 sec sampling was just adequate to follow the whole evolution of the HRF.

Although the aforementioned results are not exactly in agreement with each other, they suggest that the spinal functional response might be slower than in the brain, with a larger ratio of response to undershoot. The duration of the HRF instead, seems to be similar to that in the brain.

6.3.1 - Purpose

To compare activations obtained with the classical HRF and a spinal HRF (SC-HRF) whose parameters have been chosen in agreement with the available spinal literature.

6.3.2 - Materials and Methods

An fMRI scan was performed using the same sensory paradigm, imaging parameters and prescription described in section 5.12. The analysis pipeline described in section 5.10 was applied. The sensory stimulus was applied on the right hand of 3 healthy controls. The parameters in the HRF were chosen according to an average between results reported in the papers mentioned above (Stroman and Ryner, 2001; Brown et al., 2007; Giulietti et al. 2008).

The following parameters were used (see Fig. 6.1):

- $a_1 = 10$, delay of response in seconds [average between the results found by: Stroman and Ryner, 2001; Brown et al., 2007; Giulietti et al., 2008)
- $a_2 = 25$, delay of undershoot in seconds (Brown et al., 2007)

- $b_1 = 1$, dispersion of response
- $b_2 = 1$, dispersion of undershoot
- $c = 7.4$, ratio of response to undershoot (average between the results from Giulietti et al., 2008 and the results from Brown et al., 2007)

The length of the HRF used in the brain was kept because deemed adequate (32 seconds). The parameters b_1 and b_2 were kept as in the brain because they are not mentioned in any paper. The best model should fit the date in such a way to produce higher t-values (Handwerker et al., 2004) and more somatotopically appropriate activations.

6.3.3 - Results

In each subject, only a few voxels within the SC were activated in both cases using the two HRFs: three voxels in subject 1 and one voxel each for subjects 2 and 3. For these voxels, the corresponding t-values did not change significantly but in one case it resulted higher using the SC-HRF (t-value=3.39) instead of the canonical HRF (t-value= 2.63). Notwithstanding, for each subject, the number of activated voxels within the SC remained very similar using the two HRFs, changing at most of one voxel, and there is no evident improvement in activation specificity using one HRF in particular. Considering all subjects, the overall number of activated voxels outside the SC is reduced using the SC-HRF, indicating a possible corresponding reduction of false activations (Fig. 6.2).

The t-values resulted on average higher using the SC-HRF for all subjects, in detail:

1- For subject 1 there was a mean t-value increase of 4% (2.75 vs 2.86)
2- For subject 2 there was a mean t-value increase of 2% (2.66 vs 2.72)
3- For subject 3 there was a mean t-value increase of 8% (2.50 vs 2.70)

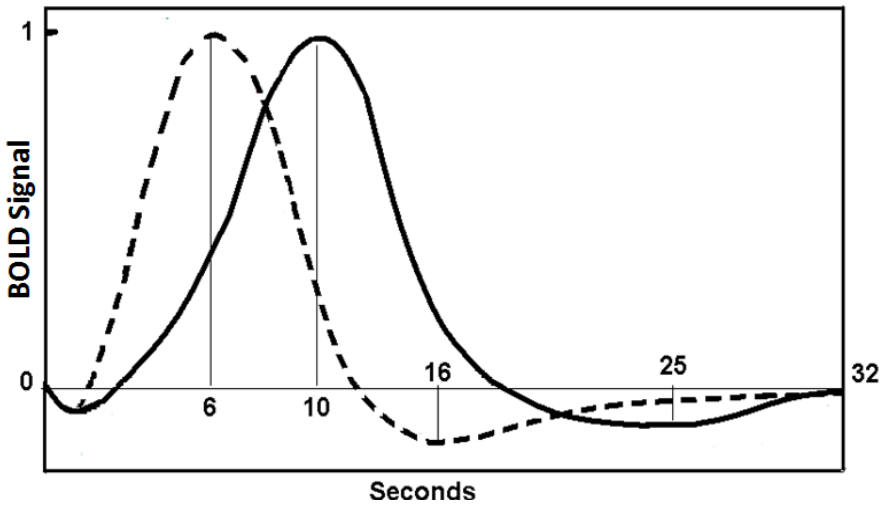

Fig. 6.1: Canonical HRF (dashed line) and spinal HRF used in this study.

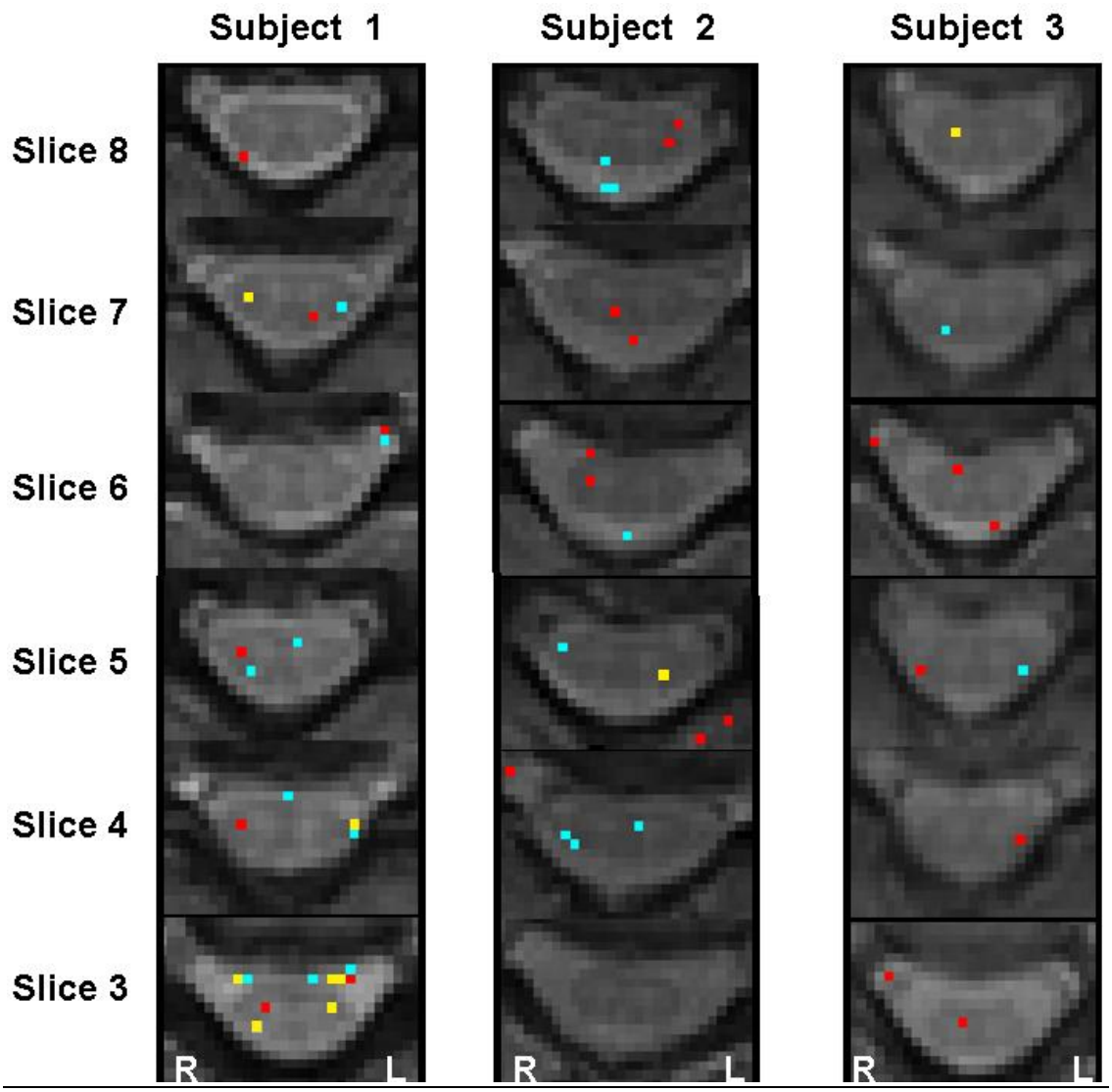

Fig. 6.2: Activations in the 3 subjects using the canonical HRF (in red) and the spinal HRF (in light-blue). Yellow voxels indicate overlapping between results obtained with the two different HRFs.

6.3.4 - Conclusion and Discussion

The proposed spinal HRF, obtained with the mean values published in 3 dedicated papers, demonstrated to be a possible alternative to the classical HRF for spinal fMRI. Although the limited number of subjects of this study, an average increase in t-values of activated voxels and a reduction of false activations, despite small, are useful to improve the feasibility of functional MRI. Results of this study seem to confirm that in the spine, as reported in the aforementioned papers (Stroman and Ryner, 2001; Brown et al., 2007; Giulietti et al. 2008), functional response might be slower than in the brain and featured by a larger ratio of response to undershoot (Fig. 6.1). Therefore, results suggest that spinal HRF is a topic that would be worth to investigate in more detail, however, given the limited number of papers that characterize the spinal HRF, the datasets in the following chapters will be analysed using the canonical HRF, also in line with most of the spinal fMRI literature.

Chapter 7 - SPINAL FMRI WITH MOTOR AND SENSORY STIMULI

Introduction

Spinal fMRI studies use a number of stimuli and there is not a strong preference for motor or sensory paradigms. In this chapter I therefore assess the spinal functional response in two settings: a motor paradigm (finger-tapping) and a sensory paradigm (brushing).

In the first part of this chapter motor-related activity using a finger-tapping paradigm is investigated on healthy controls. In the second part instead, a similar study developing a sensory paradigm is reported. In both studies, analysis is performed according to the methods described in section 5.10 and the imaging parameters are the same reported in section 2.8. Features of the signal, such as TSNR and average signal change, are evaluated. Results are reported as single subjects study and not as group study due to lack of a standardized spinal template.

7.1 - Spinal functional study with motor paradigm

7.1.1 - Purpose

The purpose of this study was to investigate motor-related activity in the spinal cord using a finger-tapping paradigm.

7.1.2 - Materials and Methods

Subjects – For this study 8 healthy volunteers were scanned but 2 datasets were discarded because the subjects moved too much and the corresponding physiological traces were not usable. Therefore, only 6 volunteers were analysed. All subjects were right-handed, 3 women and 3 men (mean age +/- std = 36.3 +/- 8.2).

Imaging parameters – All scans were performed with the 3T scanner using the 16-channel neurovascular coil. The imaging parameters were those reported in 2.8, *i.e.*: TR=3600ms, TE=30ms, voxel size=1.19x1.19x4mm^3 with 1mm gap between slices (reconstructed to 1.19x1.19x5mm^3), with a FOV=76x48 mm^2 and an acquisition matrix=64x40, 9 slices, 5 dummy scans, 200 volumes. Scan coverage extended from the upper limit of C6 to the lower limit of T1 vertebral segments. The slices were always centred transverse to the cord and the central slice was always placed in the middle of the C7 spinal segment (Fig. 7.1). For each subject, left (L-H) and right (R-H) hands performed the finger-tapping task in separate, consecutive fMRI sessions, the order being randomized between subjects. The block design comprised 10 epochs of rest alternated with 10 epochs of activation, each lasting 36 seconds. Flow compensation was used in order to reduce artefacts from cerebrospinal fluid (CSF) flow. For each subject, the cardiac trace was recorded using a pulse oximeter applied to the index finger and the respiratory trace using a pneumatic belt placed on the abdomen (diaphragm).

TSNR calculation – The TSNR was calculated with MATLAB, for a resting-state scan of one of the subjects, as the ratio between the mean time course signal throughout the voxel time-series and its standard deviation. Drifter and 2D-realignment were applied to the images. Results were obtained considering a sample of 20 voxels within the spinal cord that was identified on the mean image. TSNR was then used for power calculations (see section 2.5) to determine the required number of volumes to detect a target size effect of 2.5%.

Average signal enhancement – Average signal enhancement was calculated as [Weibull et al., 2008; Cohen-Adad and Wheeler-Kingshott, 2014]:

$$\%\text{Signal Enhancement} = \left(\frac{\text{Signal during activity}}{\text{Signal at rest}} - 1\right) \times 100 \qquad \text{Eq. 7.1}$$

fMRI analysis – Analysis was performed according to the methods described in section 5.10:

Physiological noise correction: The DRIFTER toolbox was applied to clean up the time-series from physiological noise due to cardiac pulsation and respiration (Särkkä et al., 2012).

Motion correction: Slice-by-slice motion correction was performed using FSL software as discussed previously (see section 4.1), allowing 3 degrees of freedom. Only translations along the $\hat{x}$ and the $\hat{y}$ axis and rotations in the xy plane were considered, it resulted in 3 movement regressors for each slice (translation in x and y and rotation along the z axis). Custom-made MATLAB codes were created in order to obtain slice-wise movement regressors from rototranslation matrixes to be included in the GLM implemented in SPM8.

CSF pulsation: A CSF mask was drawn using FSLview on the mean image obtained from the realigned volumes of each dataset and then applied to all realigned volumes. Custom-made MATLAB codes were then used to get a CSF regressor out of the mean values of the CSF time-course.

Statistical analysis: SPM8 software was used to perform statistical analysis (GLM) and results are reported with $p<0.01$(uncorrected) threshold significance.

For the activated voxels, signal changes and mean time-series course have been calculated using MATLAB. Furthermore, the ipsi- or contra-lateral location of neural activity was assessed for C6, C7 and T1 spinal segments. Results are reported as single subjects study and not as group study due to lack of a standardized spinal template.

7.1.3 - Results

Quality of cervical cord images was good and without any distortions.

The calculated TSNR was 15+/-3.

Using Drifter software the mean TSNR increased about 25% if compared with its average value calculated over 5 subjects without applying any physiological correction (subsection 4.1.3).

The number of volumes acquired was chosen according to Eq. 2.4. It has been calculated that with a mean TSNR of 15, a p-value of 0.01 and the block design that was used in this study, the number of volumes required to allow the detection of size effect (eff) as small as 2.5% (or larger) was 189.

Mean signal enhancements and associated standard deviations were evaluated for R-H: 3.17 +/- 1.05, and L-H: 2.99 +/- 0.90. For activated voxels inside the SC, the average time series course is reported in Fig.7.4. Fig. 7.2 shows the overall number of activated voxels found both ipsi- and contra- laterally in the C6, C7 and T1spinal segments, *i.e.* where the involved nerves enter the spinal cord (see Fig. 3.1 and Fig. 3.2). Slices 1, 2 and 3 were included in T1 vertebral level; slices 4, 5 and 6 in C7; slices 7, 8 and 9 in C6 (Fig. 7.1). Activations were detected on both ipsilateral and contralateral sides of the SC for all subjects at all levels (Fig. 7.3), however, ipsilateral activity was larger than contralateral in each spinal segment considering all subjects (Fig. 7.2). Activated voxels that were not located within the SC (but in the CSF) were neglected in the analysis.

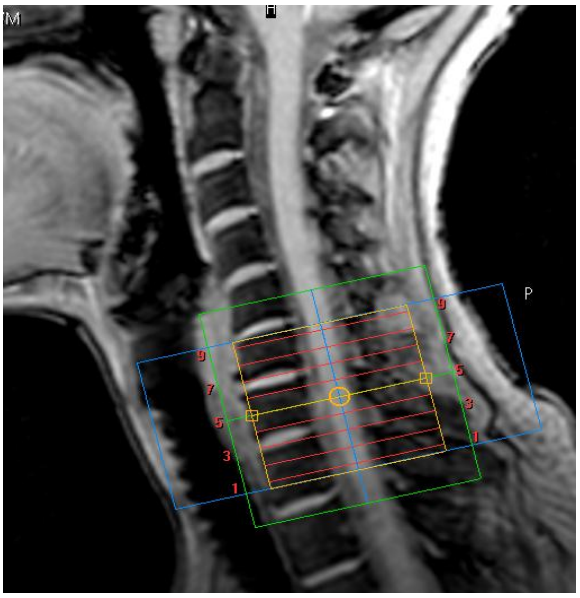

Fig. 7.1: Localization of the slices. Slices 1,2 and 3 were included in T1 vertebral level; slices 4,5 and 6 in C7; slices 7,8 and 9 in C6.

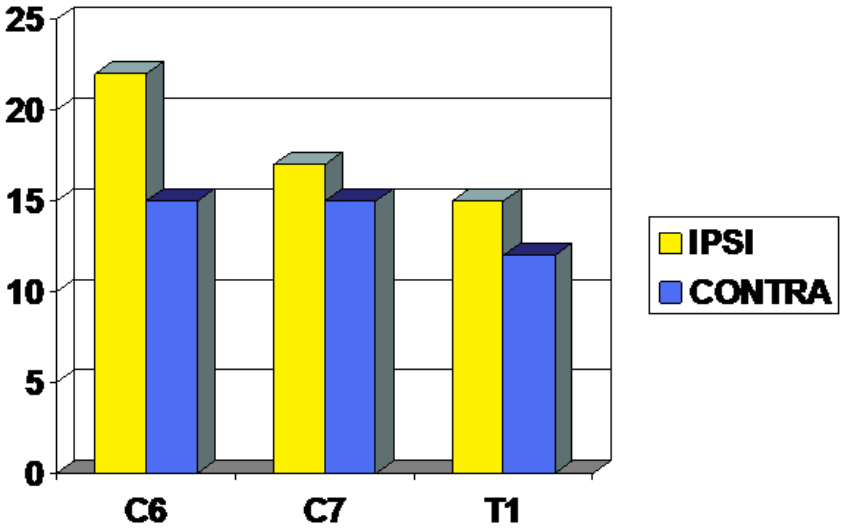

Fig. 7.2: Total number of ipsilateral (in yellow) and contralateral (in blue) activated voxels over all subjects in C6, C7 and T1 spinal segments, considering both right and left stimulation.

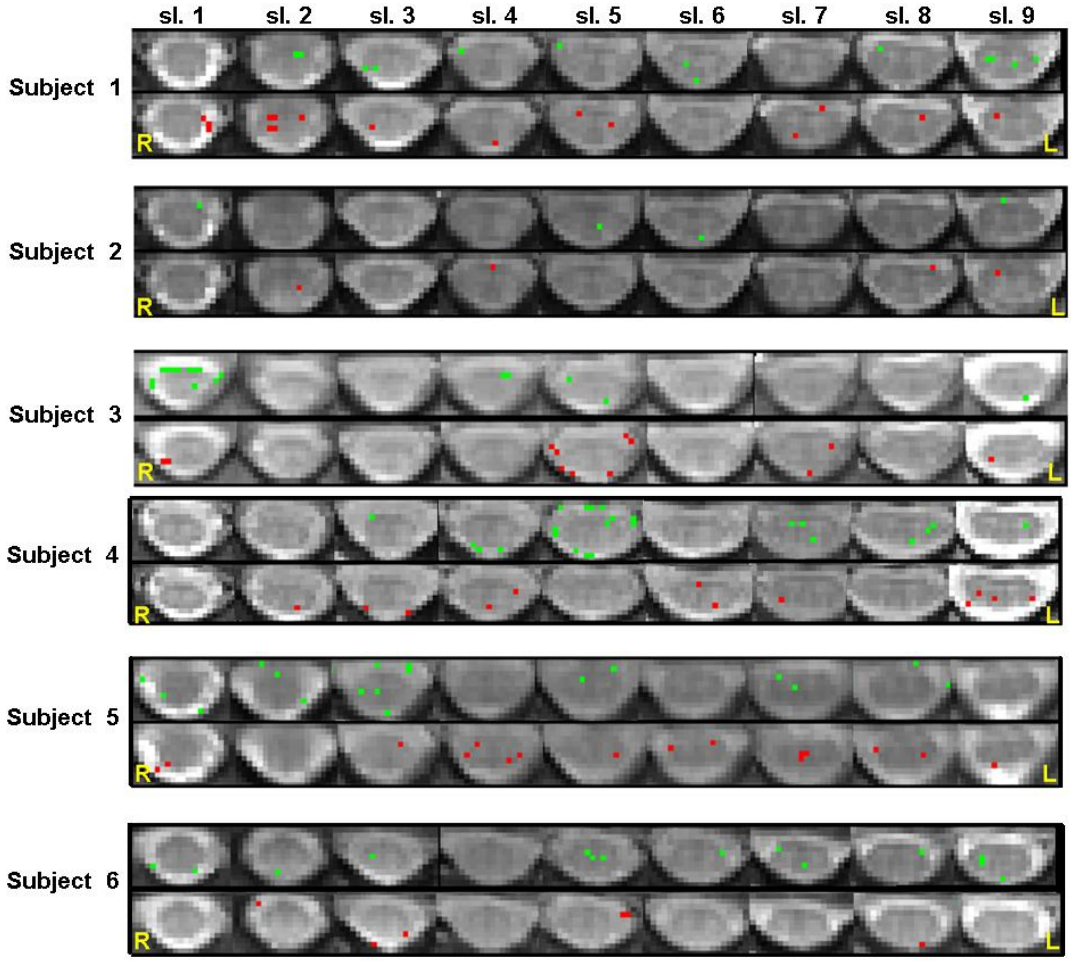

Fig. 7.3: Activations in the 9 slices for all subjects for right (in red) and left (in green) hand finger-tapping. Activated voxels are overlaid on the mean image. Slice order refers to that shown in Fig. 7.1.

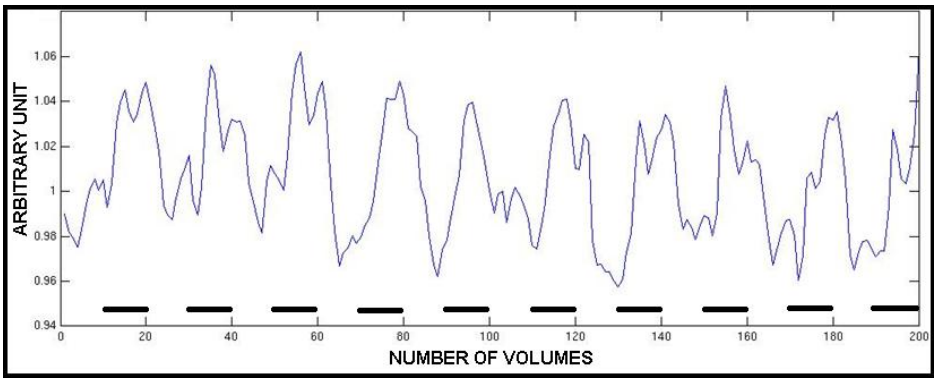

Fig. 7.4: Average signal time course for the activated voxels inside the SC for both right and left hand stimulus.

7.1.4 - Discussion

The target size effect (2.5%) was chosen by looking through the literature (Giove et al., 2004; Stroman, 2005; Govers et al., 2007; Summers et al., 2010; Stroman et al., 2014).

Sometimes the calculated signal was lower than what expected applying Eq. 2.4. A possible reason might be a size effect underestimation due to partial volume contributions throughout the time-series and, however, the theoretical estimation in Eq. 2.4 is likely to be conservative as found in previous results (Cohen-Adad et al., 2010).

The average time course evaluated for the activated voxels inside the SC fits the predicted neural activity (Fig.7.4), confirming the neuronal origin of the detected signal.

Uncorrected p-value thresholds were used, as performed in previous studies (Moffitt et al., 2005; Brooks et al., 2008; Cohen-Adad et al., 2009a, 2010).

From Fig. 7.3 it is not straightforward to locate activated voxels in either the dorsal or the ventral horns of the spinal cord, however, results show that finger-tapping task triggers both motor and sensory neurons. This may be due to sensory feedback, however, the majority of ipsilateral activations in the grey matter was expected. Activity was detected at different levels of the spinal cord reflecting the fact that a wide range of neurons was involved in the task (Backes et al., 2001; Govers et al., 2007). The signal enhancement detected during activity is in agreement with results reported in a previous study using the same task (Govers et al., 2007). Also (Govers et al., 2007), it was not possible to spot a reliable pattern of task-related activity by comparing activations in different subjects. There are a few possible causes of the different distribution of neuronal activity between subjects, for example, variations in performing the task (despite immobilization of the arm and the request to stay as still as possible). Furthermore, finger-tapping could elicit an additional slight flexion of the wrist or even an activation of certain muscles without movement (Govers et al., 2007). Lastly, rhythm and extension of the movement might have affected results too. However, the location of the detected neuronal activity (spinal cord segment C6, C7 and T1) is in agreement with the anatomical location of the neurons that activate the muscles in use.

7.2 - Spinal functional study with sensory paradigm

7.2.1 - Purpose

The purpose of this study was to assess how a tactile stimulation at specific dermatome can trigger fMRI activity in corresponding neuronal regions of the spine.

7.2.2 - Materials and Methods

Subjects – Ten healthy controls, 3 women and 7 men (mean age = 34.9+/-6.8), participated in this study. They were all right-handed.

Imaging parameters – Sequence and imaging parameters were the same described in subsection 7.1.2. The only differences were the applied stimulus and the positioning of the slices. All volunteers were scanned with a paradigm that involved localized sensory stimulation of the C6 dermatome (see Fig. 3.1) over the palmar surface of the thenar eminence, using a custom made MR-compatible electric rotating brush. The surface area of stimulation was about 1x1 cm^2 and, for each subject, left (L-H) and right (R-H) hands were stimulated in separate, consecutive fMRI sessions. The slices were always centred transverse to the cord and the central slice was always placed in the middle of the C6 spinal segment (Fig. 7.5). Flow compensation was used in order to reduce artefacts from cerebrospinal fluid (CSF) flow. Pulse oximeter was used to gather heart cycle data. A pneumatic belt placed on the abdomen (diaphragm) was used to record the respiratory trace.

TSNR calculation – TSNR was calculated, as explained in subsection 7.1.2, on one volunteer.

Average signal enhancement – Signal changes were evaluated as described in subsection 7.1.2 (see Eq. 7.1).

fMRI analysis – Analysis was performed according to the methods described in section 5.10 and already applied in section 7.1. In the current study, due to the specific dermatome that was stimulated, only activations localized in the 6 central slices (from slice 3 to slice 8; Fig. 7.5) covering the whole C6 segment (with the upper slice at the bottom of C5 segment and the lower slice at the top of C7 segment) were considered. A larger number of slices was acquired to make sure to include the whole C6 segment for all subjects, despite different spinal lengths.

7.2.3 - Results

Quality of cervical cord images was good and without any distortions. The TSNR calculated was 16+/-3. Although in Fig. 7.6 all the activated voxels are displayed, only those deemed inside the SC have been included in the analysis. For these voxels, the calculated average signal change and associated standard deviation was 3.99+/-1.40 for L-H and 3.55+/-0.90 for R-H. The average time course of the signal in the activated voxels within the SC, for both L-H and R-H, has been plotted using MATLAB software and it is shown in Fig. 7.7. All activated voxels ($p<0.01$ uncorrected) in the 6 analysed slices are shown for each volunteer in Fig. 7.6. In all volunteers activations were found inside the spinal cord and, generally, both ipsi- and contralaterally. In Fig. 7.8 the histogram shows the number of activated voxels ipsilateral and contralateral for each slice considering both R-H and L-H stimulation over all subjects. There is a predominant overall number of ipslaterally activated voxels, however, contralateral activated voxels were found as well during most scans (Fig. 7.6). Activity was found in both anterior and posterior horns of the spine (Fig. 7.6).

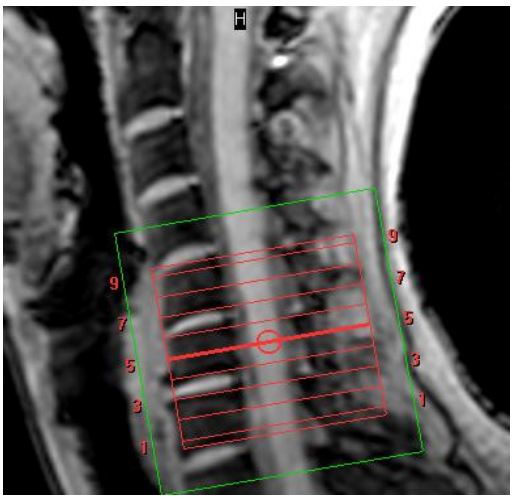

Fig. 7.5: Localization of the 9 slices. The slices were always centred transverse to the cord and the central slice was always placed in the middle of the C6 spinal segment.

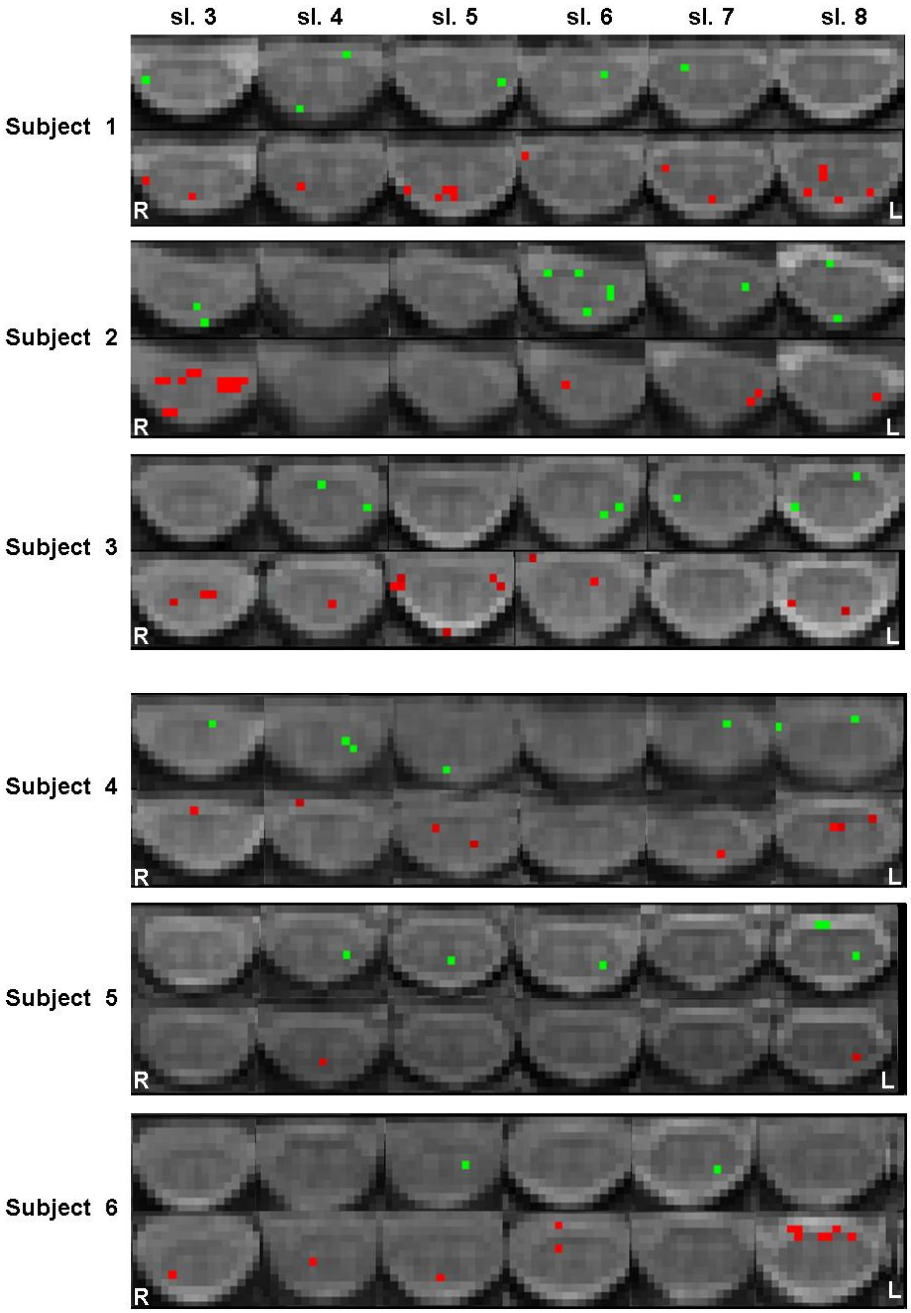

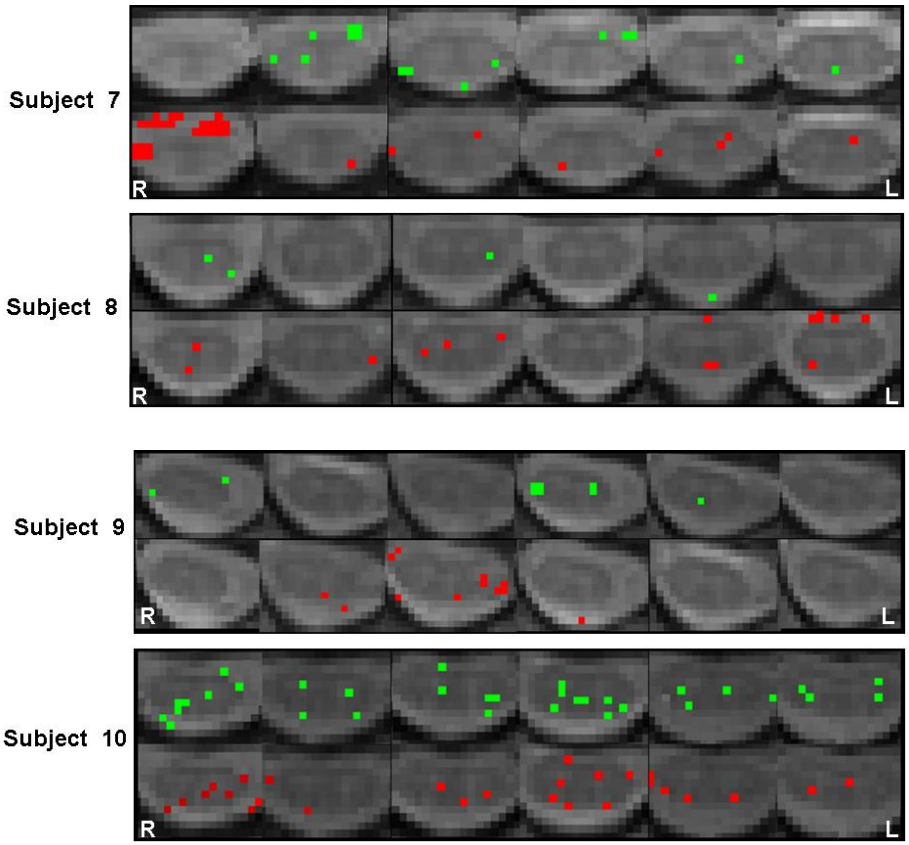

Fig. 7.6: Activations in the 6 central slices for the 10 subjects for right (in red) and left (in green) hand stimulation. Activated voxels are overlaid on the mean image. Slice order refers to that shown in Fig. 7.5.

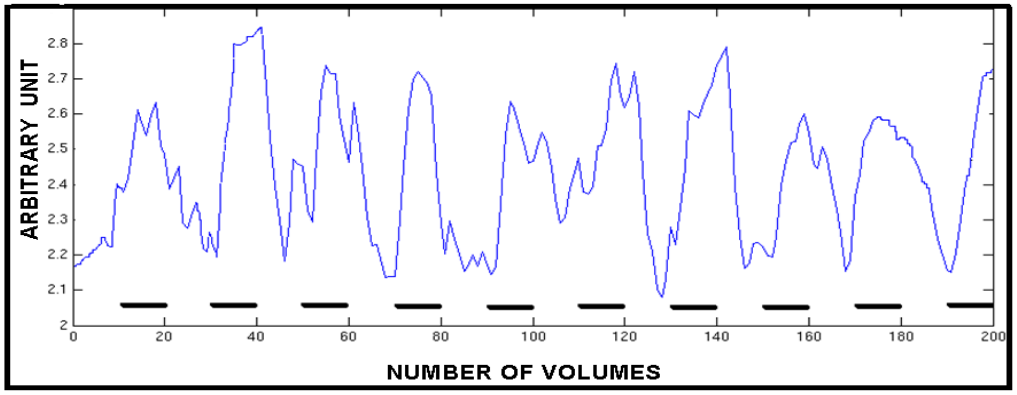

Fig. 7.7: Average signal time course for the activated voxels inside the SC for both R-H and L-H stimulus.

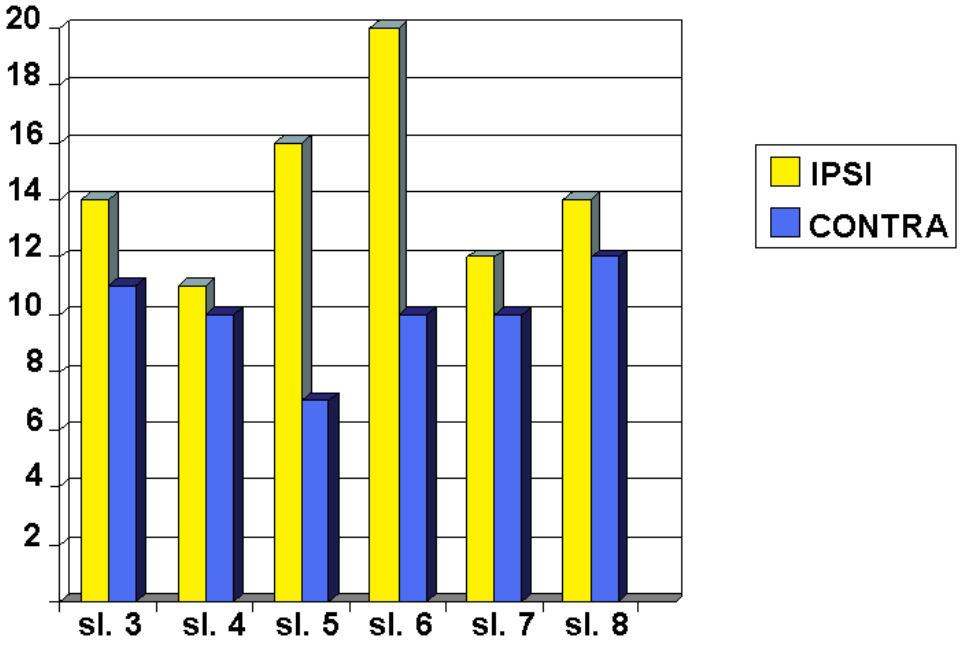

Fig. 7.8: Total number of ipsilateral (in yellow) and contralateral (in blue) activated voxels over all subjects in the 6 analyzed slices, considering both right and left stimulation. Slice numbers refer to Fig. 7.5.

7.2.4 - Discussion

The mean TSNR was in good agreement with the result obtained in section 7.1. This was expected because the sequence and imaging parameters used in this study were the same as in section 7.1.

The signal changes that were found in this study are in agreement with those reported in other studies, where a mean signal increase spanning from 3 to 5% has been detected (Yoshizawa et al., 1996; Stroman and Ryner, 2001; Stroman et al., 2002a,b; Govers et al., 2007; Maieron et al., 2007).

Consistency between the plot of the signal in activated voxels throughout the time-series and the stimulation paradigm indicates correlation between the detected neuronal activity and the applied stimulus.

Activations during a sensory stimulation can be found ipsi- and contra-laterally as reported by previous studies (Giove et al., 2004; Summers et al., 2010) and the large number of interneurons

that are involved in response to the applied stimulus (Heimer, 1988) may be activated and give rise to detected signal changes.

Besides expected posterior neuronal activity, anterior activity was found too. Notwithstanding the stimulation was not nociceptive, it is possible that both the thumb may move as a reflex in response to the vibrational stimulus that has been applied for 36 consecutive seconds in each block, or that sensitive afferent modulated anterior spinal activity.

The overall number of activated voxels inside the spine, considering all subjects, is always greater in ipsilateral than in contralateral side of the SC for all slices. It is interesting to notice that the ratio between the number of ipsi- and contra- lateral activated voxels is particularly high, compared with the other slices, at slice 5 (ratio ipsi/contra = 2.3) and slice 6 (ratio ipsi/contra = 2). These two slices are placed in the top part of the C6 vertebral level, where the nerve supplying the stimulated dermatome enters the spinal cord. This appropriate somatotopic neuronal activity supports reliability of results.

In the literature there are other studies that detected differences in activity ipsilateral and contralateral to stimulus lateralization (Stroman et al., 1999; Madi et al., 2001; Stroman and Ryner, 2001; Stroman et al., 2002), however, activation tended to be found on both right and left hemicords. Moreover, there are also studies that were not able to measure any lateralization effect in activation (Backers et al., 2001; Govers et al., 2007). The methods applied in the present study allowed the detection of a reliable segmental response that arose concomitant to neuronal activity elicited by stimulation.

7.3 - Conclusion

In this chapter motor and sensory tasks have been applied to volunteers and results showed more consistent activations using the sensory task. Results showed that delivering the stimulus to an area of skin corresponding to a specific dermatome improves specificity of the task and this specificity is reflected in the spinal functional response. Motor tasks are usually more affected by task-related motion than sensory tasks. Subject motion that correlates with the

performed task can reduce sensitivity to detect significant task-related effects. Small movements, even of submillimetre amplitude, that may involuntarily occur in the arm during finger-tapping, may affect the experimental results. Moreover, it is wise to discard the data if the subject cannot properly undertake the requested task. This may be the case of certain patients that are movement-impaired because of any disease. Sensory tasks, not requiring any movement of the subjects, are theoretically 'safer' from this point of view. However, a sensory task where a change in the tone of the muscles is involved, may be affected by task-related motion due to involuntary movements of those muscles, resulting in detection of false task-related activity. Changes in muscle tone or body posture induced by the task might reduce the sensitivity due to an increase in the variance throughout the time-series (Cohen Adad and Wheeler-Kingshott, 2014).

To conclude, I decided to apply the sensory task developed in section 7.2 to MS patients too and results are reported in the next chapter.

CHAPTER 8 – FUNCTIONAL-STRUCTURAL RELATIONSHIP IN THE CERVICAL SPINAL CORD: APPLICATION TO MULTIPLE SCLEROSIS

Introduction

After having assessed the spinal functional response using both motor and sensory tasks and having obtained more consistent results using the sensory paradigm, in this chapter that very same paradigm is delivered to both controls and MS patients.

Performing functional and structural scans in the spinal cord is technically challenging because of several issues such as small voxel dimensions, lack of signal, lack of dedicated software, susceptibility-changes related artefacts and distortions, movement and physiological confounds [Stroman, 2005; Stroman et al., 2014]. It is even more challenging to set up fMRI and DWI/DTI protocols that are affected by distortions in a similar way in order to be able to compare structural and functional information more precisely. In this chapter I propose a protocol tackling these issues, where the same SE-ZOOM-EPI sequence is employed to excite a reduced FOV for both diffusion and functional scans with identical voxel dimensions and prescriptions.

Results obtained in a group of patients affected by multiple sclerosis are compared with those obtained in a group of healthy controls. This study presents a few technical 'firsts' for the spinal cord, such as: using a reduced field-of-view sequence to perform a fMRI experiment, applying DRIFTER software to clean up the functional signal and describing functional asimmetry by a lateralization index (LI).

8.1 - Investigation of functional-structural correlation changes in multiple sclerosis using a reduced field-of-view

8.1.1 - Background

The spinal cord is a key site of pathology in multiple sclerosis (MS) [Bot and Barkhof, 2009; Lukas et al., 2013]. Being a clinically and functionally eloquent pathway, lesions or damage to the cord can have profound clinical sequelae. However, a complete understanding of the relationships between the pathophysiological changes in the cord and clinical disability is incomplete. Recently, there has been a growing interest in measuring spinal cord function and white matter microstructure using MRI (Wheeler-Kingshott et al., 2013; Stroman et al., 2014). These techniques are likely to provide important insights into cord pathophysiology in MS and have been pioneered by only a few groups around the world. Despite the very limited literature, functional MRI has been reliably applied to explore spinal cord functionality in MS patients during tactile and proprioceptive tasks (Agosta et al., 2008a, 2008b, 2009b; Valsasina et al., 2010, 2012). These studies have demonstrated that fMRI can detect important changes in the cord (such as abnormal patterns of activation) due to MS but much research needs still to be done in order to confirm these results aiming at translation from technical development to clinical applications. Consistency between different studies is important to determine the reliability of the results before adoption into the clinical setting. Diffusion weighted imaging (DWI) is a technique sensitive to microstructural properties of tissue through its sensitivity to water molecules displacement. Over the past decade, it has been successfully developed and applied to the spinal cord more consistently than fMRI; in particular the number of diffusion tensor imaging (DTI) studies of the human spinal cord has considerably increased thanks also to specific acquisition strategies being now offered on clinical scanners such as reduced field of view methods.

8.1.2 - Purpose

Investigating correlations between functional and diffusion data in the spinal cord and assessing differences between two groups of controls and MS patients.

8.1.3 - Materials and Methods

Subjects - Twelve healthy controls (HC) without any history of neurologic disease and twelve MS patients gave informed consent to participate in this study.

Two HC and three MS datasets were discarded because visual assessment determined that the subjects moved too much during the acquisition of either fMRI (and/or the corresponding recorded physiological traces were not usable) or DWI scans.

This study was therefore performed on 10 HC (6 male and 4 female; Mean Age+/-SD: 35.3+/-7.2) and 9 MS patients (3 male and 6 female; Mean Age+/-SD: 41.4+/-8.5). All subjects were right-handed. The median EDSS score of the patients was 4 (range = 1–7), four of them were secondary progressive MS and the remaining five were relapsing-remitting MS patients.

MRI protocol - All subjects were scanned with a protocol of 2 fMRI sessions and one DWI scan followed by a 3D fat-suppressed fast field echo (3D-FFE) sequence. All scans were performed on a 3T MRI scanner (Philips Achieva TX, Best, Netherlands) with a 16 channel neurovascular coil. The fMRI paradigm comprised a block design of 10 rest epochs alternating with 10 stimulus epochs, each lasting 36 seconds. A localized sensory stimulus was delivered using an MR-compatible custom-built rotating brush and applied to the C6 dermatome over the palmar surface of the thenar eminence. For each subject, left and right hands were stimulated in separate, consecutive fMRI sessions, the order being randomized between subjects. The paradigm was optimised employing a sensory task that could be used on patients with movement impairment, not able to perform properly motor tasks involving the upper limbs. Functional scans were acquired using SE-ZOOM-EPI sequence, with a reduced field of view for

targeted areas of fMRI activations. The imaging parameters were TR=3600ms, TE=30ms, voxel size=1.19x1.19x4mm^3 with 1mm gap between slices (reconstructed to 1.19x1.19x5mm^3), with a FOV=76x48mm^2 and an acquisition matrix=64x40, 9 slices, 5 dummy scans, acquisition time was 12:22 min. The slices were prescribed transverse to the cord and the central slice was always placed in the middle of the C6 spinal segment (Fig. 8.1). Cardiac and respiratory traces were recorded with a pulse oximeter and a diaphragmatic belt. The overall volume covered included the whole C6 segment, and most of the C5 and C7 segments, depending on individual spinal lengths. The same SE-ZOOM-DTI sequence was used for diffusion images matching the fMRI protocol, using the same prescription and imaging parameters mentioned above, apart from the following: TE = 52 ms and TR = 9 RRs (cardiac gated). The DWI protocol comprised 30 b = 1000 s mm^{-2} DWI volumes with gradient directions evenly distributed over the sphere and 3 non–DWI (b = 0) volumes. The total acquisition time for the DWI scan was about 8-9 mins, depending on heart rate. All subjects were asked to remain as still as possible for the full duration of the scan session and to not respond in any way during the sensory stimulation. Furthermore, aiming at limiting involuntary movements, subjects were applied neck padding and the stimulated hand was immobilized by a custom-made restraint.

Data analysis **-** All data were analysed in subject space so results are reported for each individual participant.

fMRI - Functional datasets were processed according to the following pipeline.

Physiological noise reduction - The DRIFTER toolbox implemented in SPM8 software was applied to clean up the time-series from physiological noise due to cardiac pulsation and respiration (Särkkä et al., 2012).

Motion correction - Slice-by-slice motion correction was performed allowing 3 degrees of freedom and implemented using MATLAB codes to wrap FSL (FLIRT) software command

lines (see section 4.1). Only the six central slices, covering the whole C6 segment plus the bottom of C5 and the top of C7, were taken into account in the analysis (Fig. 8.1).

CSF pulsation - A CSF mask was drawn using FSLview on the mean image obtained from the realigned volumes of each dataset and then applied to all realigned volumes (see section 5.7). Each mask was accurately drawn in order to include only voxels that were deemed CSF (Fig. 8.4a,b). SPM8 software was used to perform statistical analysis (GLM) of functional images. In the count of activated voxels, only those within the SC and excluded by the CSF mask, were taken into account (Fig. 8.4a,b).

Statistical analysis (fMRI) - Functional results were obtained using a p=0.01 uncorrected threshold, as reported by previous spinal fMRI studies (e.g. Moffitt et al., 2005; Brooks et al., 2008; Cohen-Adad et al., 2009, 2010; Eippert et al., 2009; Stroman et al., 2011).

Average signal enhancement - Average signal enhancement was calculated as described in Eq. 7.1 in subsection 7.1.2. Time courses corresponding to the activated voxels in the same subject were averaged and signal change was calculated over the baseline. Then the signal intensity time course from each subject was averaged across all the subjects.

Lateralization index - An overall lateralization index (LI) to assess asymmetry in the activation response when stimulating either hand of each subject was defined as:
LI = total number of ipsi-lateral / total number of contra-lateral activated voxels.
Lateralization indexes for right (LI_R) and left (LI_L) hand stimulation were also separately calculated in a similar way for each subject, considering the ratio ipsi-/contra- lateral activated voxels within each run.

DWI - Diffusion-weighted datasets were processed with the following steps.

DTI fitting - The Camino toolbox (Cook et al., 2006) was used to process diffusion data to calculate fractional anisotropy (FA) values.

Quantitative maps analysis - JIM 6.0 software (Xinapse system, www.xinapse.com) was used to draw regions of interest (ROIs) in the posterior column white matter (PCWM) and to outline left and right hemicords (LH and RH) and the whole spine (WS) on the b0 images of each subject (Fig. 8.4c). The mean and standard deviation (SD) of FA were calculated for all ROIs, i.e. PCWM, WS, LH and RH (Fig. 8.4c).

Statistical analysis (DWI) - SPSS software was used to compare means and assessing functional-structural correlations. The following methods were used: the Whitney Mann U test to compare means, the Spearman's rank correlation coefficient for correlations and the Paired-Sample T test to compare means between right and left hand.

8.1.4 - Results

Activity was detected in all subjects (Table 8.1 and Table 8.2).

The number of significantly activated voxels in the ipsi- and contra-lateral location for each subject (Fig. 8.2 and Fig.8.3**)** was assessed by their location within the LH and RH ROIs. In the majority of subjects ipsilateral activation was dominant (Table 8.1 and Table 8.2). In the controls (Table 8.1), the activated voxels were mostly ipsilateral for both right hand stimulation (in 7 cases out of 10) and left hand stimulation (in 8 cases out of 10). In one case LI_R was smaller than 1 and in two cases it was equal to 1. In two cases LI_L was equal to 1. The LI coefficient is also reported for each subject and there is a majority of overall ipsilateral activations in 9 cases out of 10. In one subject instead, an equal number of ipsi- and contra-lateral activated voxels was found. In the patients as well (Table 8.2), majority of activated voxels was mostly ipsilateral for both right hand stimulation (in 6 cases out of 9) and left hand stimulation (in 9 cases out of 9). In three cases LI_R was equal to 1.

The average signal change averaged across all active voxels inside the cord of the 10 controls (Fig. 8.5) and of the 9 MS patients (Fig. 8.6) is reported. Mean signal enhancements and associated standard deviations were the following: for controls [Right hand: 3.74+/- 1.29%, and Left hand: 3.30+/-1.13%] and for patients [Right hand: 3.32+/- 1.00% and Left hand: 3.60+/- 1.28%]. Mean values were similar between right and left hand and between different groups.

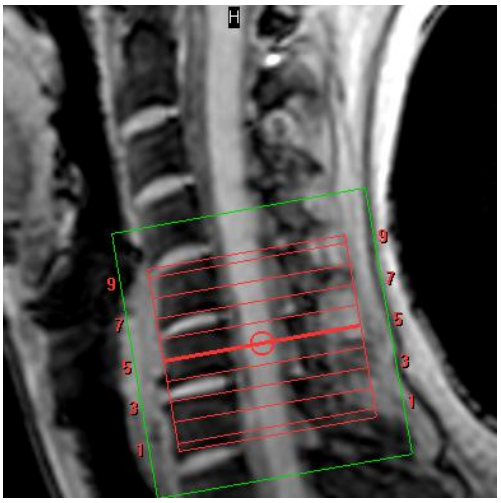

Fig. 8.1: Localization of the slices.

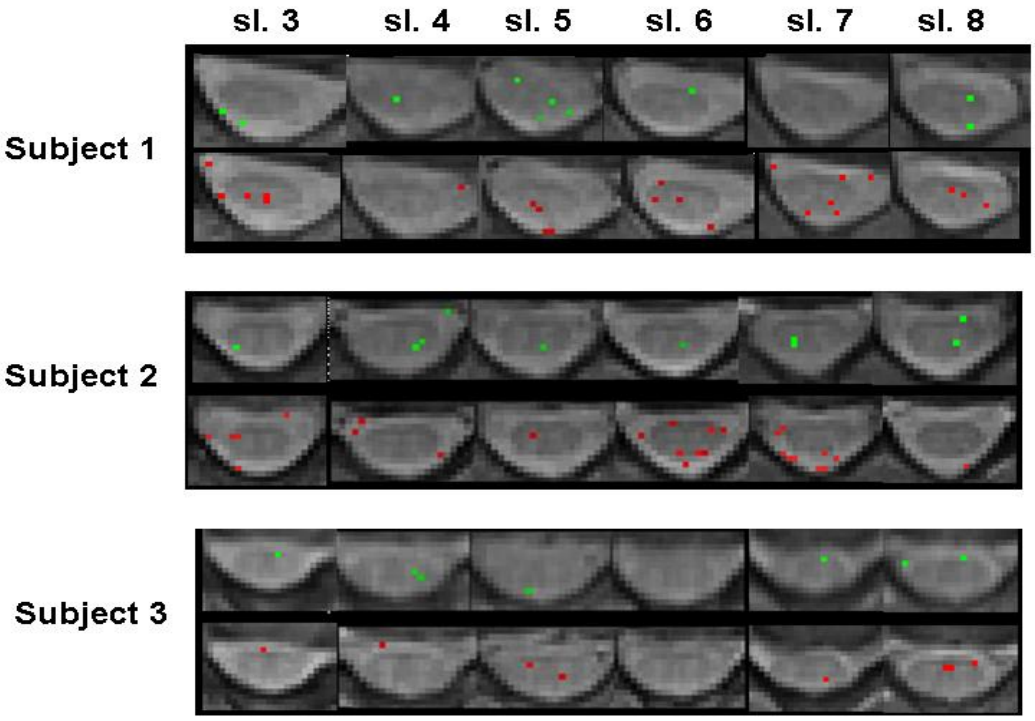

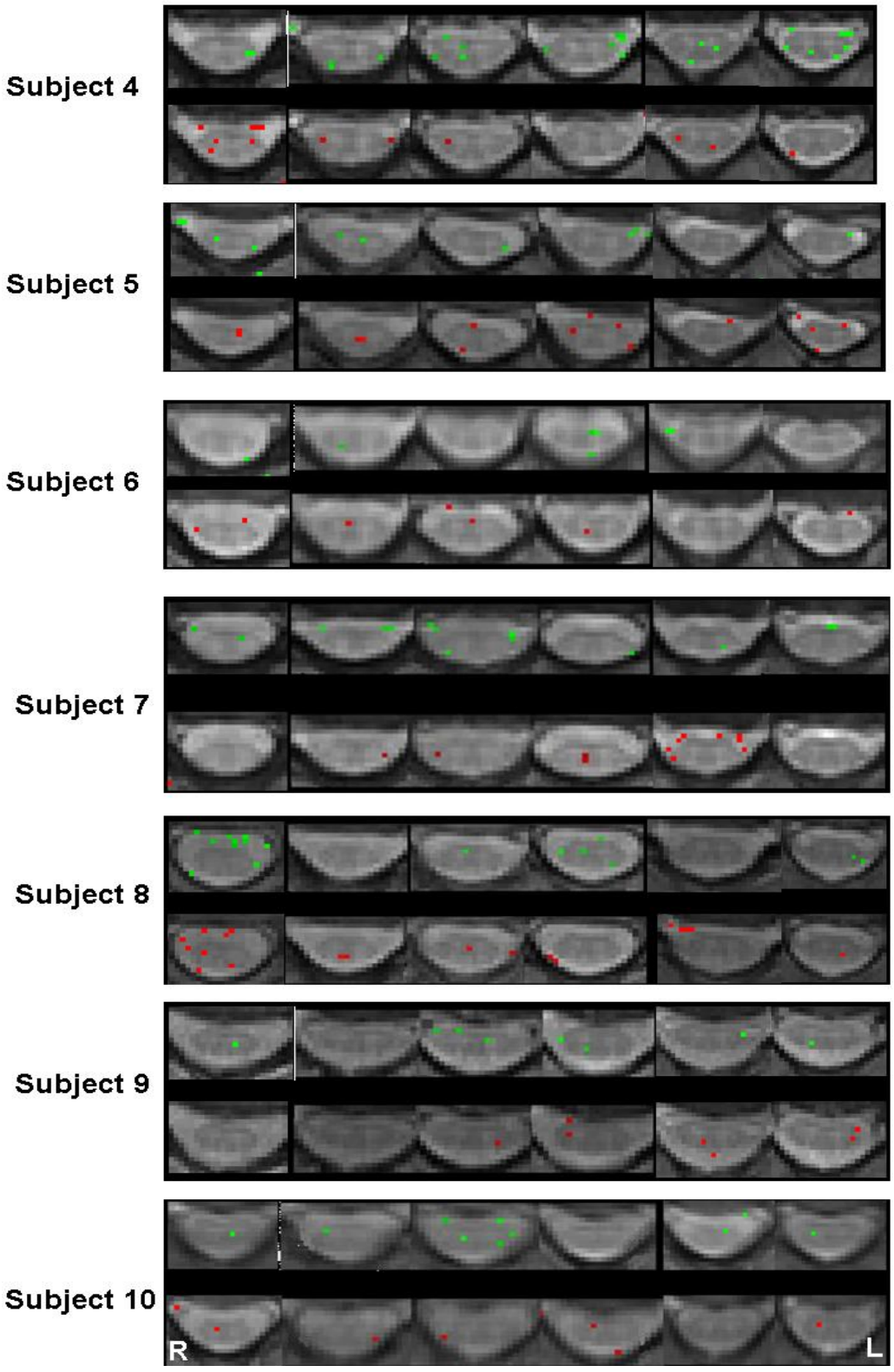

Fig. 8.2: Activations in the 6 central slices for the 10 controls for right (in red) and left (in green) hand stimulation. Activated voxels are overlaid on the mean image. Slice order refers to that shown in Fig. 8.1.

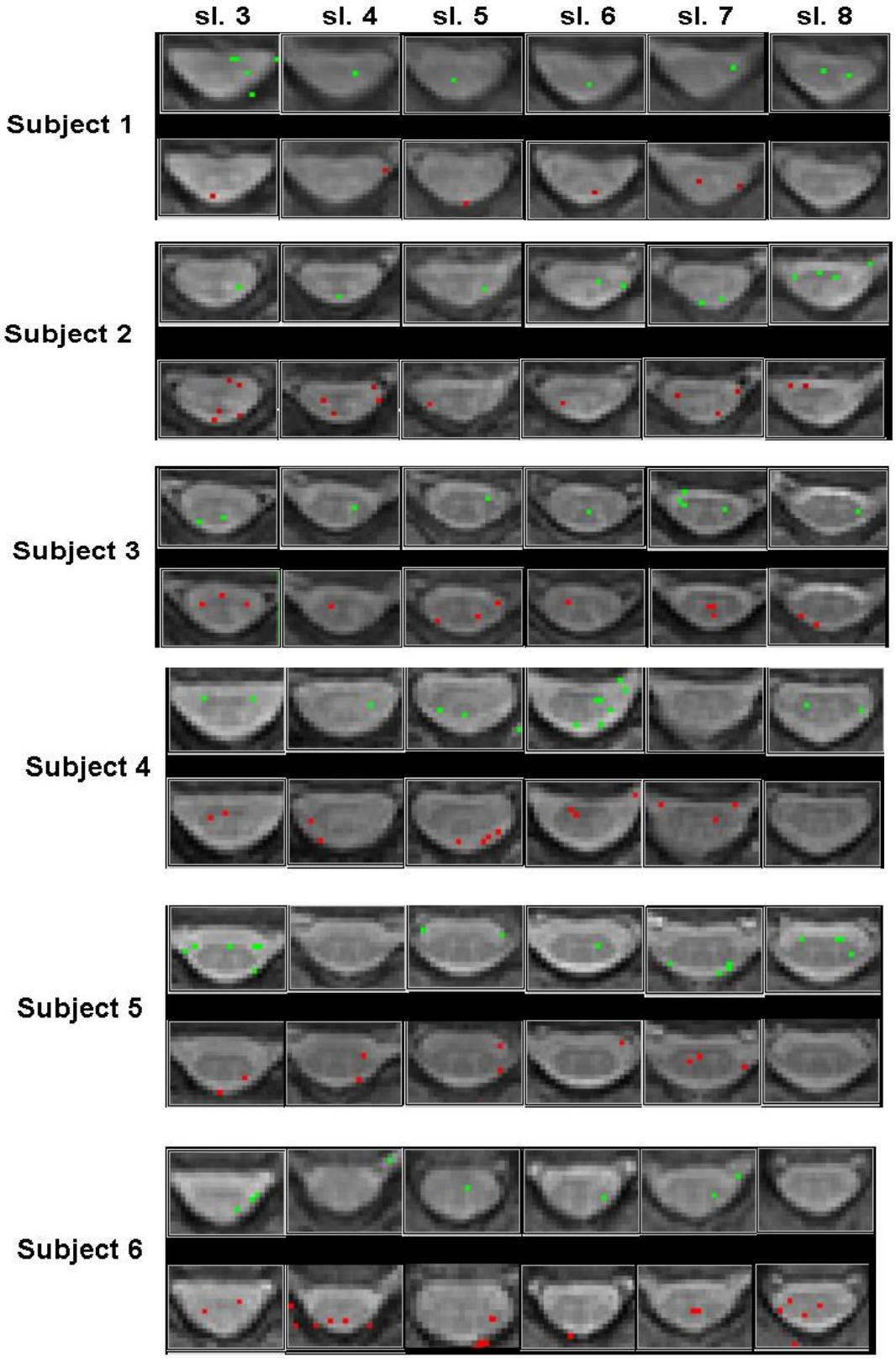
sl. 3
sl. 4
sl. 5
sl. 6
sl. 7
sl. 8
Subject 1
Subject 2
Subject 3
Subject 4
Subject 5
Subject 6

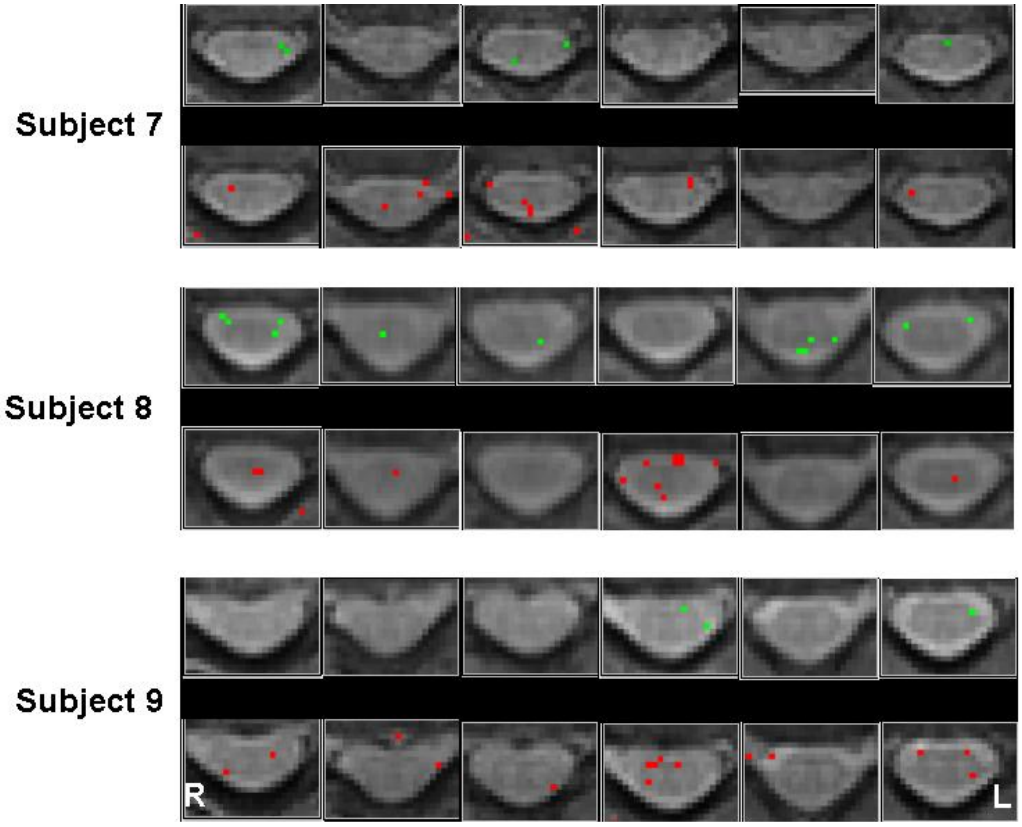

Fig. 8.3: Activations in the 6 central slices for the 9 MS patients for right (in red) and left (in green) hand stimulation. Activated voxels are overlaid on the mean image. Slice order refers to that shown in Fig. 8.1.

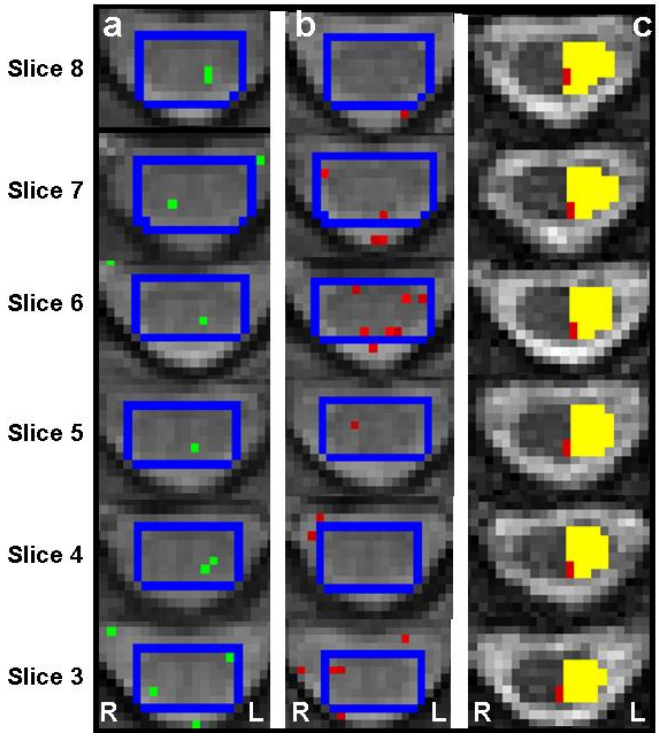

Fig. 8.4 : Spinal activity in one of the subjects for left (a; in green) and right (b; in red) hand stimulation overlaid to the mean image. The number of the slice refers to Fig.1. In the count of activated voxels, only those within the SC and excluded by the CSF mask, were taken into account The blue rectangles show the voxels considered for the CSF mask. In c) it is shown an example of the b0 images associated with the same slices and overlaid the LH (in yellow) and the PCWM (in red) masks.

	R_ipsi-contra	L_ipsi-contra	LI_R	LI_L	LI
Subject 1	8 – 6	6 – 3	1.33	2.00	1.56
Subject 2	7 – 4	7 – 2	1.75	3.50	2.33
Subject 3	3 – 4	5 – 1	0.75	5.00	1.60
Subject 4	6 – 2	8 – 7	3.00	1.14	1.56
Subject 5	6 – 5	5 – 2	1.20	2.50	1.57
Subject 6	2 – 1	2 – 1	2.00	2.00	2.00
Subject 7	3 – 1	2 – 1	3.00	2.00	2.50
Subject 8	3 – 3	3 – 3	1.00	1.00	1.00
Subject 9	2 – 2	3 – 2	1.00	1.50	1.25
Subject 10	3 – 1	3 – 3	3.00	1.00	1.50
			Mean: 1.80+/-0.90	**Mean: 2.16+/-1.26**	**Mean: 1.69+/-0.46**

Table 8.1: Number of both ipsi- and contra- laterally activated voxels for right (R_ipsi-contra) and left (L_ipsi-contra) hand stimulation for the 10 HC. Values of lateralization index are reported for right (LI_R) and left (LI_L) hand stimulation and for both of them (LI). Means and standard deviations are reported too.

	R_ipsi-contra	L_ipsi-contra	LI_R	LI_L	LI	EDSS
Subject 1	2 – 1	7 – 2	2.00	3.50	3.00	6.00
Subject 2	5 – 2	6 – 1	2.50	6.00	3.67	7.00
Subject 3	7 – 2	6 – 3	3.50	2.00	2.60	2.00
Subject 4	6 – 1	7 – 3	6.00	2.33	3.25	7.00
Subject 5	2 – 2	5 – 2	1.00	2.50	1.75	2.00
Subject 6	5 – 5	4 – 0	1.00	4.00	1.80	1.00
Subject 7	5 – 2	3 – 1	2.50	3.00	2.67	6.00
Subject 8	3 – 3	7 – 4	1.00	1.75	1.43	2.00
Subject 9	6 – 4	3 – 0	1.50	3.00	2.25	3.00
			Mean: 2.33+/-1.62	Mean: 3.12+/-1.10	Mean: 2.49+/-0.75	

Table 8.2: Number of both ipsi- and contra- laterally activated voxels for right (R_ipsi-contra) and left (L_ipsi-contra) hand stimulation for the 9 MS patients. Values of lateralization index are reported for right (LI_R) and left (LI_L) hand stimulation and for both of them (LI). Means and standard deviations are reported below. EDSS value also is reported for each subject.

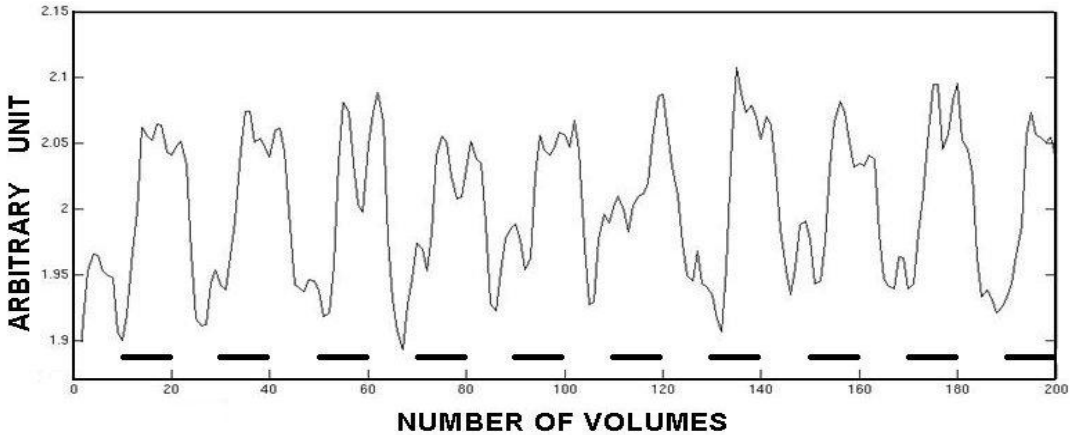

Fig. 8.5: Average time course of all activated voxels within the spinal cord of 10 controls for both right and left task. Activation epochs are indicated by black lines.

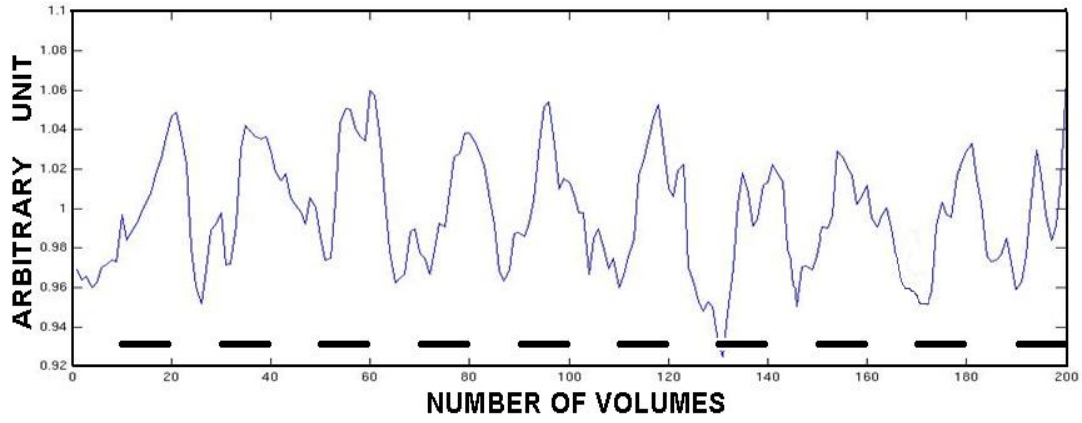

Fig. 8.6: Average time course of all activated voxels within the spinal cord of 9 MS patients for both right and left task. Activation epochs are indicated by black lines.

Lateralization indices (LI_R, LI_L, LI) are reported for each control (Table 8.1) and each patient (Table 8.2). Results showed differences in mean LI between MS patients and HC. Calculated values for the lateralization indices (Mean+/-SD) were: for controls [LI_R = 1.80+/-0.90, LI_L = 2.16+/-1.26 and LI = 1.69+/-0.46] and for patients [LI_R = 2.33+/-1.62, LI_L = 3.12+/-1.10 and LI = 2.49 +/- 0.75]. Neither signal enhancements for right and left hand stimulation nor lateralization indexes LI_L and LI_R analyzed with the paired-sample T test showed statistically significant difference. The EDSS value for each patient is also reported in Table 8.2. Values of FA were calculated in both groups for each ROI, i.e. WS, LH, RH, PCWM and the mean values and standard deviations are shown in the box plots in Fig. 8.7. For the controls, the following values of fractional anisotropy were calculated (Mean+/-SD): FA_WC=0.66+/-0.03, FA_RH=0.66+/-0.03, FA_LH=0.65+/-0.03, FA_PCWM=0.76+/-0.04. For the patients instead, the following values were found (Mean+/-SD): FA_WC=0.59+/-0.07, FA_RH=0.58+/-0.06, FA_LH=0.59+/-0.06, FA_PCWM=0.67+/-0.06. Correlations between LI and FA were evaluated for MS and HC regarding the posterior column white matter (PCWM),each hemicord (LH, RH) and the whole cord (WS).

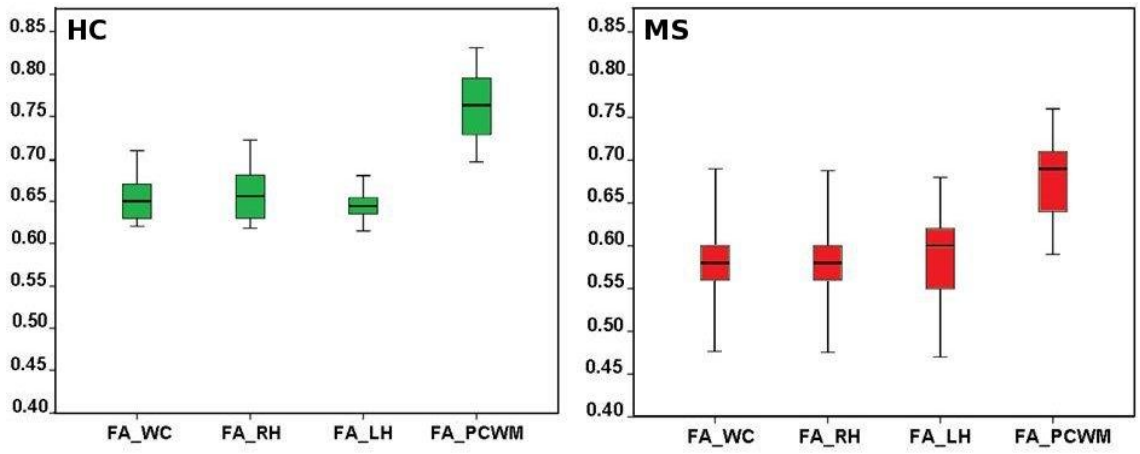

Fig. 8.7: Mean values of fractional anisotropy (FA) calculated for the 10 controls (HC, in green) and the 9 MS patients (MS, in red) referring to 4 different kinds of ROIs covering: whole cord (WC), right hemisphere (RH), left hemisphere (LH) and posterior column white matter (PCWM).

Greater LI in MS patients (i.e. more ipsilateral than contralateral activity) was associated with lower fractional anisotropy calculated in PCWM (p=0.025) (Fig. 8.8) and it strongly correlated with the EDSS (p=0.002) (Fig.8.9). No other significant correlations were found.

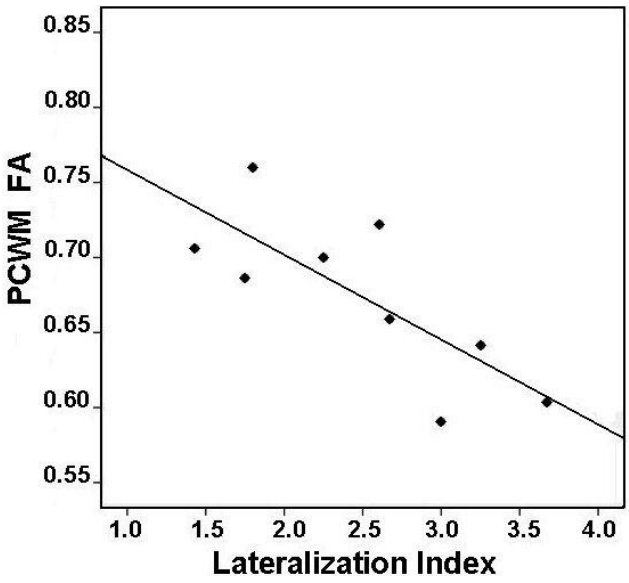

Fig. 8.8: Correlation between fractional anisotropy (FA) calculated in the posterior column white matter (PCWM) for MS patients and overall lateralization index (LI) [p=0.025; R^2linear=0.631].

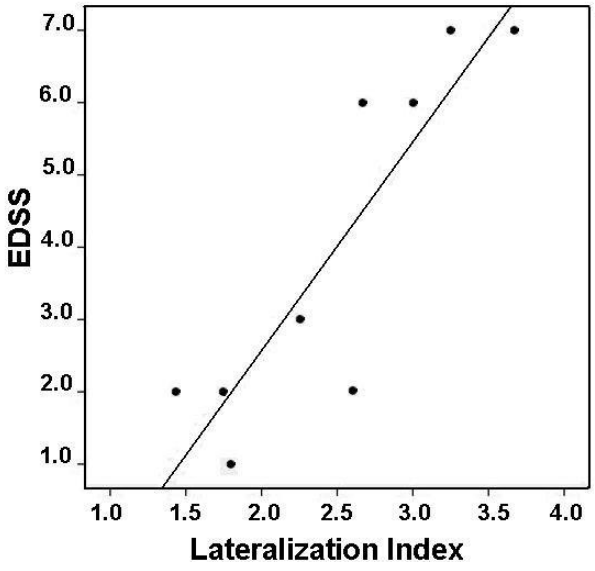

Fig. 8.9: Correlation in MS patients between EDSS and overall lateralization index (LI) [p=0.002; R^2linear=0.773].

8.1.4 - Conclusion and Discussion

The signal changes that were found in this study for the controls are in agreement with those reported in chapter 7 using the same paradigm and imaging parameters. The mean time-course of the activated voxels within the SC confirmed detection of task related neuronal activity.

The signal changes for MS patients were in agreement too with those published in MS studies that reported mean values between 3% and 4% (Agosta et al., 2008a, 2008b, 2009b; Valsasina et al., 2010, 2012).

This study successfully presented a method for obtaining structural and functional information from the cervical spinal cord with a protocol using fMRI and DWI sequences characterised by the same geometrical distortions. The method was successful in introducing a few original contributions, both from the acquisition and analysis point of view: i) using a spin echo EPI gradient-based reduced FOV sequence in a spinal fMRI experiment, ii) applying DRIFTER software physiological noise correction of the BOLD signal in the spine and iii) introducing a LI to describe functional asymmetry in the spine and using it to investigate possible structural correlations. The DTI acquisition and the diffusion parameters analysis are currently used in our research group and have been reported in a recent publication (Kearney et al., 2014).

The DTI protocol had the same geometrical properties as the fMRI therefore the scans were inherently aligned to each other, apart from possible minimal movement of the subject.

This study assessed whether in healthy subjects functional response depends on fractional anisotropy and correlated LI with this structural parameter for a number of ROIs. Results showed that in HC these are not coupled, hence, at least at cord level, these structural and functional properties are independent in healthy tissue or require a much higher sample size to be revealed. Moreover, results showed that there is indeed a correlation between functional impairment and structural damage.

Greater lateralization of functional activity detected in MS patients was found to be associated with FA reduction in the posterior column. White matter in the posterior column constitutes an important sensory pathway, important for tactile, pressure and vibration sensations (Standring et al., 2005). PCWM reduction may be due to lesions in this pathway. It could be hypothesized

that in the spine an enhancement of lateralized neural activity contributes to limit the functional impact of MS related damage.

EDSS scale is a method for quantifying disability due to MS and is an indicator of severity of the disease. The higher the EDSS index, the higher the impact of multiple sclerosis on patient's life, reflecting a more severe damage. The fact that a higher EDSS was associated with a higher LI may indicate that a larger ipsilateral neural activity is likely to compensate a more severe damage due to the disease.

Both the correlations discussed above, seem to suggest that adaptive changes remodeling functional activity occur in the spinal cord as a compensatory phenomenon in MS, in order to limit the clinical consequences of tissue damage.

Let's now discuss the variability of the detected functional activity and what the implications are for the use of spinal fMRI in the clinical setting.

The interpretation of the functional results obtained for each subject of this study is not straightforward. This is due to both low reproducibility and inter-subject variability of the results. Although the reproducibility of the applied methods, tested in a previous section of this thesis (section 5.12), gave encouraging outcome, the variability of neural activity between subjects is an important issue that needs to be considered. Different subjects, even if healthy controls, might present slightly different anatomical features. Although the spinal nerves supplying the C6 dermatome enter the spinal cord at the C6 vertebral segment, the exact location of these nerves may change between subjects within a vertebral segment spanning a few centimetres. For this reason, the neural activity detected in different subjects by applying the same sensory stimulus, might even occur in different slices. Moreover, even the extent of the activated area might change between subjects (Standring et al., 2005). In order to make easier the interpretation of any functional abnormality due to the disease it would be very useful to have a table reporting reference values from healthy controls, in such a way to compare these values with those obtained in an exam. Regrettably, such a table does not exist yet.

To conclude, the results obtained in this study warrant further investigations in patients with neurological conditions such as MS where both structural and functional data are recorded. The

proposed strategy using geometrically matched protocols makes these studies feasible and easier to analyse and interpret.

Chapter 9 – CONCLUSIONS AND FUTURE DIRECTIONS

9.1 - Conclusion

The purpose of this thesis was to define a functional and structural protocol to study spinal cord alterations, which could merge information from different modalities. Given the different stages of functional and structural MRI of the spine, in this thesis I have discussed and tackled several issues about spinal fMRI, investigating more in depth aspects that have been often reported only superficially in the literature. After an introductory part concerning magnetic resonance principles, I tested the ZOOM-EPI sequence using a reduced FOV in the brain to assess its performance in fMRI studies and then I have applied it to the spinal cord. This is the first time that this sequence has been applied to perform fMRI in the spine. Due to the very limited literature, there is no established pipeline suggesting how to analyse spinal functional datasets and different research groups perform analyses in a subjective way, possibly biasing results and hindering comparisons between different studies.

In chapter 3, after an anatomical description of the spinal cord, I discussed the physiological mechanisms that underpin the signal change as a consequence of functional activation. The BOLD and SEEP effects were introduced and put in context within a wide literature review.

In chapter 4, I developed an analysis pipeline testing all the preprocessing steps that can be found in the literature. Results have shown that: 2D-realignment guarantees the higher TSNR, neither slice timing nor temporal derivatives are decisive for detecting functional activations, smoothing spinal datasets may have more drawbacks than advantages. This pipeline has then been applied to all datasets in this thesis.

In chapter 5, I discussed and compared the performances of both RETROICOR-like methods and DRIFTER software to remove physiological noise due to cardiac pulsation and respiration. This is the first time that DRIFTER software was tested in the spinal cord. After assessing the

better performance of DRIFTER software, this was applied to all the functional studies included in this thesis. A CSF regressor, accounting for CSF pulsation, was always included in the analysis. Reproducibility of spinal fMRI is an issue not usually reported in current literature, especially at single subject level. In chapter 5, I tested the reproducibility of the methodology I proposed in individual subjects and results obtained from test and re-test scans on 3 healthy subjects showed common patterns of activity both ipsilaterally and contralaterally.

In chapter 6, I tested the performance of an alternative spinal HRF showing how it constitutes a valid alternative to the canonical HRF and that it would be worth investigating this issue, underestimated in the literature, in greater depth.

In chapter 7, I performed two functional studies on healthy subjects aiming at investigating neuronal activity in response to a motor and a sensory task. TSNR was reported and signal changes were in agreement with the literature (Yoshizawa et al., 1996; Stroman and Ryner, 2001; Stroman et al., 2002a,b; Govers et al., 2007; Maieron et al., 2007). In both experiments a predominant overall number of ipsilaterally activated voxels was found, however, a minority of contralateral activated voxels also was detected for most scans. Due to small spinal dimensions, it was not straightforward to locate activated voxels in either the dorsal or ventral horns of the spinal cord, however, results showed that the applied methods strongly reduced the number of false activations found both in the CSF and outside the spinal cord, increasing reliability of those activations detected within the cord. Furthermore, results showed that a localised sensory task (delivered with a custom made MRI compatible rotating brush) is more suitable than a motor task (fingertapping) to detect lateralization capability in the spinal cord. Moreover, this sensory paradigm could be delivered passively to all subjects, without requiring them to perform any task, limiting the risk of involuntary task related movement. For these reasons, this sensory stimulus was chosen for being applied to MS patients too.

In chapter 8, I reported a multimodal study including both controls and MS patients. The same ZOOM-EPI sequence, employed to perform diffusion and functional scans with identical voxel dimensions and geometrical prescription, allowed more precise comparisons between structural and functional information. The mean signal changes for healthy controls were in agreement with those found in chapter 7 and, for MS patients, they were consistent with values reported in

the literature. In most subjects ipsilateral activation was dominant. Results showed differences in mean lateralization (LI) index between MS patients and controls. Greater LI in MS patients (i.e. more ipsilateral than contralateral activation) was associated with lower posterior column white matter fractional anisotropy and it strongly correlated with the EDSS.

In conclusion, the initial purpose of this PhD project has been fully achieved by: demonstrating that it is possible to detect functional activation using ZOOM-EPI, already used for DI, developing a robust analysis pipeline, tackling important technical issues, assessing the feasibility of the technique with different stimuli and, finally, presenting a multimodal protocol suitable for investigating correlations between functional and diffusion data acquired in the cervical spinal cord of both healthy controls and MS patients.

9.2 - Future directions

Although, at present, SC fMRI technique is not ready to be applied in the clinical setting, in future, the clinical applications of SC fMRI might be really helpful to patients suffering from spinal injuries or spinal diseases, assessing the grade of functional damage and the response to an applied treatment. Furthermore, spinal fMRI might aid clinical diagnosis and surgical planning for several neurological and psychiatric conditions (Detre, 2006; Jezzard and Buxton, 2006; Matthews et al., 2006; Owen and Coleman, 2008). Recently, functional studies have been performed as group studies (for statistical strength), including resting state experiments too, on both volunteers and patients (Wei et al., 2010; Brooks et al, 2012; Barry et al., 2014; Eippert et al., 2014; Nejad et al., 2014). However, although group analysis adds to literature on SC-fMRI, at the current state of art this kind of study does not add further information aiming at the translation to the clinical setting. The first aim that should be achieved, in my opinion, is an improvement of spinal fMRI reliability at single subject level and the establishment of an acknowledged analysis pipeline for single subjects studies. Moreover, so far, the papers published on spinal fMRI investigate only activations in the cervical segments, except for a few

studies performed in the lumbar spine in humans (Kornelsen et al., 2004; Moffitt et al., 2005) and animals (Zhao et al., 2008; Cohen-Adad et al., 2009a). Although the ZOOM sequence used in this study proved to be valuable, strategies to use reduced FOV imaging with gradient or RF based methods should be compared for both functional and structural MRI. This was beyond the scope of this thesis but given the promising results obtained, further investigation of sequence designs is warranted. One major hurdle for spinal fMRI and DI is the development of efficient coils to detect signal. While for brain applications there has been an expansion of multi-channel coils, for spinal cord imaging we are still using the standard coils with a limited number of receive arrays. To increase reliability of both functional and structural imaging of the spine, higher SNR would be greatly beneficial, built together with strategies to limit motion and improve patient comfort. This is an aspect of spinal imaging that was not investigated at all during this thesis as it was beyond the scope of this work.

Hopefully, developing new analysis techniques, new sequences and dedicated software, might make possible to apply spinal fMRI to all the spinal segments and to improve its reliability too, allowing the translation to the clinical setting.

BIBLIOGRAPHY

Abragam, A. "The principles of nuclear magnetism, 1961." Oxford: University Press 119 (1998): 120.

Agosta F., Valsasina P., Rocca M.A., Caputo D., Sala S., Judica E., Stroman P.W., Filippi M.. Evidence for enhanced functional activity of cervical cord in relapsing multiple sclerosis. Magn Reson Med (2008a) 59: 1035–1042.

Agosta F., Valsasina P., Caputo D., Stroman P.W., Filippi M.. Tactile-associated recruitment of the cervical cord is altered in patients with multiple sclerosis. NeuroImage 39 (2008b) 1542 – 1548.

Agosta F., Valsasina P., Caputo D., Rocca M.A., Filippi M.. Tactile-associated fMRI recruitment of the cervical cord in healthy subjects. Hum Brain Mapp (2009a); 30: 340–345.

Agosta F., Valsasina P., Absinta M., Sala S., Caputo D., Filippi M.. Primary progressive multiple sclerosis: Tactile-associated functional MR activity in the cervical spinal cord. Radiology (2009b); 253: 209–215.

Aguirre G.K., Zarahn E., M. D'Esposito.. The variability of human, BOLD hemodynamic responses. NeuroImage (1998); 8 (4): 360 – 369.

Ances B.M., Leontiev O., Perthen J.E., Liang C., Lansing A.E., Buxton R.B.. Regional differences in the coupling of cerebral blood flow and oxygen metabolism changes in response to activation: Implications for BOLD-fMRI. NeuroImage 39 (2008) 1510 – 1521.

Andrew, Edward Raymond. Nuclear magnetic resonance. Cambridge University Press, 1955.

Backes W.H., Mess W.H., Wilmink J.T.. Functional MR Imaging of the Cervical Spinal Cord by Use of Median Nerve Stimulation and Fist Clenching. AJNR Am J Neuroradiol 2001; 22:1854–1859.

Bandettini P.A., Wong E.C., Hinks R.S., Tikofsky R.S., Hyde J.S.. Time course EPI of human brain function during task activation. Magn. Reson. Med. 25, 390–397 (1992).

Bandettini P.A., Wong E.C., Jesmanowicz A., Hinks R.S., Hyde J.S.. Spin-echo and gradient-echo EPI of human brain activation using BOLD contrast: a comparative study at 1.5 T. NMR Biomed 1994 Mar; 7(1-2): 12-20.

Bandettini P.A., et al. Characterization of cerebral blood oxygenation and flow changes during prolonged brain activation. Hum Brain Mapp. 1997; 5(2): 93–109.

Barry R.L., Smith S.A., Dula A.N., Gore J.C.. Resting state functional connectivity in the human spinal cord. Elife. 2014 Aug 5; 3: e02812.

Bennett C.M. and Miller M.B.. How reliable are the results from functional magnetic resonance imaging? Ann. N.Y. Acad. Sci. 1191 (2010) 133-155.

Bernstein, Matt A., Kevin F. King, and Xiaohong Joe Zhou. Handbook of MRI pulse sequences. Elsevier, 2004.

Bhattacharyya P.K., Mathew B., Bermel R., Phillips M., Stone L., Lowe. M.. GABA correlates differently with fMRI activation volume and BOLD signal in noisy datasets.. Proc. Intl. Soc. Mag. Reson. Med. 22 (2014).

Birn R.M., Diamond J.B., Smith M.A., Bandettini PA. Separating respiratory-variation-related fluctuations from neuronal-activity-related fluctuations in fMRI. Neuroimage (2006); 31(4): 1536-48.

Bodurka J., Ye F., Petridou N., Bandettini P.A.. Determination of the brain tissue-specific temporal signal to noise limit of 3 T BOLD-weighted time course data. Paper Presented at: Proc. Intl. Soc. Mag. Reson. Med. 2005 (Miami).

Borogovac A., Asllani I.. Arterial Spin Labeling (ASL) fMRI: advantages, theoretical constrains, and experimental challenges in neurosciences. Int J Biomed Imaging. (2012); 2012:818456.

Bot J.C. and Barkhof F.. Spinal-cord MRI in multiple sclerosis: conventional and nonconventional MR techniques. Neuroimaging Clin N Am. 2009 Feb; 19(1): 81-99.

Bouwman C.J., Wilmink J.T., Mess W.H., Backes W.H.. Spinal cord functional MRI at 3 T: gradient echo echo-planar imaging versus turbo spin echo. Neuroimage (2008); 43, 288–296.

Boynton G. M., Engel S. A., Glover G. H., Heeger, D. J.. Linear systems analysis of functional magnetic resonance imaging in human V1. Journal of Neuroscience (1996), 16, 4207-4221.

Brannen J.H., Badie B., Moritz C.H., et al. Reliability of functional MR imaging with word-generation tasks for mapping Broca's area. AJNR Am J Neuroradiol (2001); 22:1711–18.

Brieu N., Beaumont E., Dubeau S., Cohen-Adad J., Lesage F.. Characterization of the hemodynamic response invivo rat lumbar spinal cord by intrinsic optical imaging and laserspeckle microscopy. J Neurosci Methods. 2010; 30:191(2):151–157.

Brooks J.C.W., Beckmann C.F., Miller K.L., Wise R.G., Porro C.A., Tracey I., Jenkinson M.. Physiological noise modelling for spinal functional magnetic resonance imaging studies. Neuroimage 2008 Jan 15; 39(2): 680-92.

Brooks J.C.W., Kong Y., Lee M.C., Warnaby C.E., Wanigasekera V., Jenkinson M., Tracey I.. Stimulus Site and Modality Dependence of Functional Activity within the Human Spinal Cord. The Journal of Neuroscience, May 2, 2012. 32(18): 6231– 6239.

Brosch J.R., Talavage T.M., Ulmer J.L., Nyenhuis J.A.. Simulation of human respiration in fMRI with a mechanical model. IEEE Trans Biomed Eng 2002; 49(7): 700–707.

Brown J.E., Watcha D.S., Darnauer J., Sarin R., Glover G., Mackey S.. A hemodynamic response function for functional MRI of the cervical spine using motor and nociceptive paradigms. Proc. Int. Soc. Mag. Res. Med., 15 (2007).

Buxton R.B. and Frank L.R.. (1997). A model for the coupling between cerebral blood flow and oxygen metabolism during neural stimulation. J. Cereb. Blood Flow Metab. 17(1): 64-72.

Buxton R.B.. The elusive initial dip. NeuroImage (2001), 13, 953 – 958.

Cadotte D.W., Stroman P.W., Mikulis D., Fehlings M.G.. A systematic review of spinal fMRI research: outlining the elements of experimental design. J Neurosurg Spine 2012 (Suppl) 17: 102–118, 2012.

Carretta, Pietro. NMR-MRI,[mu] SR, and Mössbauer Spectroscopies in Molecular Magnets. Springer, 2007.

Chen Y. and Parrish TB.. Caffeine's effects on cerebrovascular reactivity and coupling between cerebral blood flow and oxygen metabolism. NeuroImage 2009; 44(3): 647–652.

Cohen M.S.. Parametric analysis of f MRI data using linear systems methods. NeuroImage (1997), 6, 93-103.

Cohen M.S. and DuBois R.M.. Stability, repeatibility and the expression of signal magnitude in functional magnetic resonance imaging. J.Magn. Reson. Imaging. (1999) 10: 33-40.

Cohen-Adad J., Piché M., Rainville P., Benali H. and Rossignol S.. Impact of realignment on spinal functional MRI time series. Proceedings of the 29th Annual International Conference of the IEEE EMBSCité Internationale, Lyon, France, August 23-26, 2007.

Cohen-Adad J., Hoge R.D., Leblond H., Xie G., Beaudoin G., Song A., Krueger G., Doyon J., Benali H., Rossignol S.. Investigations in functional MRI of the spinal cord of cats under ketamine. NeuroImage (2009a), 44(2): 328–339.

Cohen-Adad J., Rossignol S., Hoge R.D.. Slice-by-slice motion correction in spinal cord fMRI: SliceCorr. Proceedings 17th Scientific Meeting. International Society for Magnetic Resonance in Medicine, 2009b, Honolulu, Hawaii, p. 3181.

Cohen-Adad J., Gauthier C.J., Brooks J.C., Slessarev M., Han J., Fisher J.A., Rossignol S., Hoge R.D.. BOLD signal responses to controlled hypercapnia in human spinal cord. Neuroimage (2010) 50: 1074 – 1084.

Cohen-Adad J. and Wheeler-Kingshott C.A.M.. "Quantitative techniques for MRI of the human spinal cord." (2014).

Clark V.P., Maisog J.M., Haxby J.V.. fMRI study of faceperception and memory using random stimulus sequences. Journal of Neurophysiology (1998), 79, 3257-3265.

Dagli M.S., Ingeholm J.E., Haxby J.V.. Localization of cardiac-induced signal change in fMRI. NeuroImage (1999); 9(4): 407–415.

Dale A.M. and Buckner R.L.. Selective averaging of rapidly presented individual trials using f MRI. Human Brain Mapping (1997), 5, 329-340.

Darquié A., Poline J.B., Saint-Jalmes H., Le Bihan D.. Transient decreases in water diffusion observed in occipital cortex during visual stimulation. MAGMA, 11 (suppl. 1) (2000), pp. 76–77.

Deckers R.H.R., van Gelderen P., Ries M., Barret O., Duyn J.H., Ikonomidou V.N., Fukunaga M., Glover G.H., de Zwart J.A.. An adaptive filter for suppression of cardiac and respiratory noise in MRI time series data NeuroImage 33 (2006); 1072 – 1081.

D'Esposito M., Deouell L.Y., Gazzaley A.. Alterations in the BOLD fMRI signal with ageing and disease: a challenge for neuro imaging. Nat Rev Neurosci. 2003; 4(11): 863–872.

Detre J.A., Wang J.. Technical aspects and utility of fMRI using BOLD and ASL. Clin Neurophysiol. (2002) May;113(5): 621-34.

Detre J.A.. Clinical applicability of functional MRI. J Magn ResonImaging 2006; 23(6): 808–15.

Dirac, Paul.Adrien Maurice. "The principles of quantum mechanics." (1930).

Duncan K.J., Pattamadilok C., Knierim I., Devlin J.T.. Consistency and variability in functional localisers. Neuroimage (2009); 46: 1018–1026.

Eippert F., Finsterbusch J., Bingel U., Büchel C.. Direct Evidence for Spinal Cord Involvement in Placebo Analgesia Science 326, 404 (2009).

Eippert F., Tracey I.. The spinal cord is never at rest. Elife. 2014 Aug 5; 3: e03811.

Ekstrom A.. How and when the Fmri BOLD signal relates to underlying neural activity: the danger in dissociation. (2010) Brain Res Rev 62:233-44.

Figley C.R. and Stroman P.W.. Development and validation of retrospective spinal cord motion time-course estimates (RESPITE) for spin-echo spinal fMRI: Improved sensitivity and specificity by means of a motion-compensating general linear model analysis. NeuroImage 44 (2009); 421–427.

Figley C.R., Leitch J.K., Stroman P.W.. In contrast to BOLD: signal enhancement by extravascular water protons as an alternative mechanism of endogenous fMRI signal change. Magn Reson Med 2010 Oct.; 28(8): 1234-43.

Fox P.T. and Raichle M.E.. Focal physiological uncoupling of cerebral blood flow and oxidative metabolism during somatosensory stimulation in human subjects. Proc. Natl Acad. Sci USA (1986). 83(4): 1140-1144.

Friese S., Hamhaber U., Erb M., Klose U.. B-waves in cerebral and spinal cerebrospinal fluid pulsation measurement by magnetic resonance imaging. J. Comput. Assist. Tomogr. 2004: 28, 255–262.

Friston, K., Ashburner, J., Frith, C., Poline, J.-B., Heather, J., and Frackowiak, R.. Spatial registration and normalization of images. Human Brain Mapping, 2: 165–189 (1995).

Friston K.J., Fletcher P., Josephs O., Holmes A., Rugg M.D., Turner R.. Event-related fMRI: Characterizing Differential Responses. NeuroImage (1998), 7, 30-40.

Friston K.J., Holmes A.P. & Ashburner J.. Statistical Parametric Mapping (SPM). Academic Press; 2006.

Fujita H., Meyer E., Reutens D.C., Kuwabara H., Evans A.C., Gjedde A.. Cerebral [15O] Water Clearance in Humans Determined by Positron Emission Tomography: II. Vascular Responses to Vibrotactile Stimulation. J Cereb Blood Flow Metab (1997); 17: 73–79.

Gao J.H. and Liu H.L.. Inflow effects on functional MRI. NeuroImage 62 (2012) 1035–1039.

Gati J.S., Menon R.S., Ugurbil K., Rutt B.K.. Experimental Determination of the BOLD Field Strength Dependence in Vessels and Tissue . Magn Reson Med 38:296302 (1997).

Geissler A., Lanzenberger R., Barth M., Tahamtan A.R., Milakara D., Gartus A. and Beisteinera R.. Influence of fMRI smoothing procedures on replicability of fine scale motor localization. NeuroImage 24 (2005); 323 – 331.

Giove F., Garreffa G., Giulietti G., Mangia S., Colonnese C., Maraviglia B.. Issues about the functional MR Imaging of the human spinal cord. Magnetic Resonance Imaging 22: 1505-1516 (2004).

Giulietti G., Giove F., Garreffa G., Colonnese C., Mangia S., Maraviglia B.. Characterization of the functional response in the human spinal cord: Impulse-response function and linearity. Neuroimage (2008); 42(2): 626-34.

Glover G.H., Li T.Q., Ress D.. Image-based method for retrospective correction of physiological motion effects in fMRI: RETROICOR. Magn. Reson. Med. 2000. 44, 162–167.

Govers N., Béghin J., Van Goethem J.W.M., Michiels J., van den Hauwe L., Vandervliet E., Parizel P.M.. Functional MRI of the cervical spinal cord on 1.5 T with fingertapping: to what extent is it feasible?. Neuroradiology (2007) 49:73–81.

Guimaraes A.R., Melcher J.R., Talavage T.M., et al.. Imaging subcortical auditory activity in humans. Hum Brain Mapp. 1998; 6(1): 33–41.

Haacke, E. Mark, et al. "Magnetic resonance imaging." Physical principles and sequence design (1999).

Handwerker D.A., Ollinger J.M., D'Esposito M.. Variation of BOLD hemodynamic responses across subjects and brain regions and their effects on statistical analyses. NeuroImage 21 (2004) 1639 – 1651.

Hashemi, Ray Hashman, William G. Bradley, and Christopher J. Lisanti. MRI: the basics. Lippincott Williams & Wilkins, 2012.

Heimer L.. The human brain and spinal cord functional neuroanatomy and dissection guide. New York: Springer-Verlag; 1988. Pp.152-167.

Hennig J., Janz C., Speck O., Ernst T.. Functional spectroscopy of brain activation following a single light pulse: Examinations of the mechanism of the fast initial response. Int J Imag Syst Technol, 6 (1995), pp. 203–208.

Hou J.M., Sun T.S., Xiang Z.M., Zhang J.Z., Zhang Z.C., Zhao M., Zhong J.F., Liu J., Zhang H., Liu H.L., Yan R.B., Li H.T.. Alterations of resting-state regional and network-level neural function after acute spinal cord injury. Neuroscience. 2014 Jul 30; 277C: 446-454.

Hu X., Le T.H., Parrish T., Erhard P.. Retrospective estimation and correction of physiological fluctuation in functional MRI. Magnetic Resonance in Medicine (1995), 34: 201-212.

Huettel S.A. and McCarthy G.. Regional Differences in the Refractory Period of the Hemodynamic Response: An Event-Related fMRI Study. Neuroimage (2001); 14(5): 967–976

Hyde J.S., Biswal B.B., Jesmanowicz A.. High-Resolution fMRI Using Multislice Partial k-Space GR-EPI With Cubic Voxels . Magnetic Resonance in Medicine 46:114 –125 (2001).

Jabbi, M., et al. "Response to “Voodoo Correlations in Social Neuroscience” by Vul et al." (2009).

Jezzard P. and Clare S.. Sources of distortion in functional MRI data. Human Brain Mapping, 8:80–85, (1999).

Jezzard P. and Buxton R.B.. The clinical potential of functional magnetic resonance imaging. J Magn Reson Imaging 2006; 23(6):787–93.

Jin T., Wang P., Tasker M., Zhao F., Kim S.G.. Source of nonlinearity in echo-time-dependent BOLD fMRI. Magn Reson Med (2006); 55:1281–90.

Jo H.J., Lee J.M., Kim J.H., Shin Y.W., Kim I.Y., Kwon J.S., and Kim S.I.. Spatial accuracy of fMRI activation influenced by volume- and surface-based spatial smoothing techniques. NeuroImage 34 (2007): 550 – 564.

Jochimsen T.H., Norris D.G., Moller H.E.. Is There a Change in Water Proton Density Associatedwith Functional Magnetic Resonance Imaging?. Magnetic Resonance in Medicine 53:470 – 473 (2005).

Josephs O., Turner R., Friston K.. Event-Related fMRI. Human Brain Mapping (1997), 5: 243–248.

Kearney H., Schneider T., Yiannakas M.C., Altmann D.R., Wheeler-Kingshott C.A., Ciccarelli O., Miller D.H.. Spinal cord grey matter abnormalities are associated with secondary progression and physical disability in multiple sclerosis. J Neurol Neurosurg Psychiatry. 2014 Aug 5. pii: jnnp-2014-308241. doi: 10.1136/jnnp-2014-308241.

Kim S.G. and Ogawa S.. Biophysical and physiological origins of blood oxygenation level-dependent fMRI signals. Journal of Cerebral Blood Flow & Metabolism (2012) 32, 1188–1206.

Kornelsen J., Stroman P.W.. fMRI of the lumbar spinal cord during a lower limb motor task. Magn Reson Med 2004;52:411-414.

Krueger G. and Glover G.H.. Physiological noise in oxygenation-sensitive magnetic resonance imaging. Magn. Reson. Med. (2001); 46, 631 – 637.

Krueger G., Kastrup A., Glover G.H.. Neuroimaging at 1.5 T and 3.0 T: comparison of oxygenation-sensitive magnetic resonance imaging. Magn. Reson. Med. 2001. 45, 595 – 604.

Kong Y., Jenkinson M., Andersson J., Tracey I., Brooks J.C.W.. Assessment of physiological noise modelling methods for functional imaging of the spinal cord. NeuroImage 60 (2012) 1538–1549.

Kwong K.K., Belliveau J.W., Chesler D.A., Goldberg I.E., Weisskoff R.M., Poncelet B.P., Kennedy D.N., Hoppel B.E., Cohen M.S., Turner R., Cheng H.M., Brady T.J., Rosen B.R.. Dynamic magnetic

resonance imaging of human brain activity during primary sensory stimulation. Proc Natl Acad Sci USA. 1992 Jun 15; 89 (12): 5675-9.

Le T.H. and Hu X.. Retrospective Estimation and Correction of Physiological Artifacts in fMRI by Direct Extraction of Physiological Activity from MR Data. Magnetic Resonance in Medicine (1996), 35:290-298

Le Bihan D., Urayama S., Aso T., Hanakawa T., Fukuyama H.. Direct and fast detection of neuronal activation in the human brain with diffusion MRI. Proc. Natl. Acad. Sci. USA (2006). 103, 8263–8268.

Le Bihan D.. The 'wet mind': water and functional neuroimaging. Phys. Med. Biol. (2007). 52, R57–R90.

Leitch J.K., Figley C.R., Stroman P.W.. Applying fMRI to the spinal cord and brainstem. Magn.Reson.Imaging 28:1225-1233 (2010).

Li G., Ng M.C., Wong K.K., Luk K.D., Yang E.S.. Spinal effects of acupuncture stimulation assessed by proton density-weighted functional magnetic resonance imaging at 0.2 T. Magnetic Resonance Imaging 23 (2005) 995 – 999.

Lieberman M.D., Berkman E.T., Wager. T.D.. Correlations in social neuroscience aren't voodoo: Commentary on Vul et al. (2009). Perspect. Psycholog. Sci.(2009) 4: 299–307.

Lindauer U., Royl G., Leithner C., Kuhl M., Gold L., Gethmann J., Kohl-Bareis M., Villringer A., Dirnagl U.. No evidence for early decrease in blood oxygenation in rat whisker cortex in response to functional activation. NeuroImage (2001), 13, 988 – 1001.

Lindeberg T., Lidberg P., Roland P.E.. Analysis of brain activation patterns using a 3-D scale-space primal sketch. Hum Brain Mapp. 1999; 7(3): 166-94.

Logothetis N.K. and Wandell B.A.. Interpreting the BOLD Signal. Annual Review of Physiology. Vol. 66 (2004): 735-769.

Logothetis N.K.. What we can do and what we cannot do with fMRI. Nature 2008, 453:869-78.

Lu H., Golay X., Pekar J.J., Van Zijl P.C.. Functional magnetic resonance imaging based on changes in vascular space occupancy. Magn Reson Med. (2003) Aug; 50(2): 263-74.

Lu H., van Zijl P.C.. A review of the development of Vascular-Space-Occupancy (VASO) fMRI. Neuroimage (2012) Aug 15; 62(2): 736-42.

Lu H., Hua J., van Zijl P.C.. Noninvasive functional imaging of cerebral blood volume with vascular-space-occupancy (VASO) MRI. NMR Biomed. (2013) Aug; 26(8): 932-48.

Lukas C., Sombekke M.H., Bellenberg B., Hahn H.K., Popescu V., Bendfeldt K., Radue E.W., Gass A., Borgwardt S.J., Kappos L., Naegelin Y., Knol D.L., Polman C.H., Geurts J.J., Barkhof F., Vrenken H.. Relevance of spinal cord abnormalities to clinical disability in multiple sclerosis: MR Imaging findings in a large cohort of patients. Radiology. 2013 Nov; 269(2): 542-52.

Lund T.E., Madsen K.H.. Sidaros K., Luo W.L., Nichols T.E.. Non-white noise in fMRI: does modelling have an impact? NeuroImage 29, 54–66 (2006).

Madi S., Flanders A.E., Vinitski S., Herbison G.J., and Nissanov J.. Functional MR Imaging of the Human Cervical Spinal Cord. AJNR Am J Neuroradiol 22: 1768–1774, October 2001.

Maieron M., Iannetti G.D., Bodurka J., Tracey I., Bandettini P.A., Porro C.A.. Functional Responses in the Human Spinal Cord during Willed Motor Actions: Evidence for Side- and Rate-Dependent Activity. The Journal of Neuroscience, April 11, 2007, 27(15): 4182 – 4190.

Malinen S., Schurmann M., Hlushchuk Y., Forss N., Hari R.. Improved differentiation of tactile activations in human secondary somatosensory cortex and thalamus using cardiac-triggered fMRI. Exp Brain Res. 2006; 174(2): 297–303.

Marcus M.L., Heistad D.D., Ehrhardt J.C., Abboud F.M.. Regulation of total and regional spinal cord blood flow. Circ Res. 1977;41(1):128–134.

Matthews P.M., Honey G.D., Bullmore E.T.. Applications of fMRI intranslational medicine and clinical practice. Nat Rev Neurosci 2006; 7(9): 732–44.

Menon R.S., Ogawa S., Tank D.W., Ugurbil K.. 4 Tesla gradient recalled echo characteristics of photic stimulation-induced signal changes in the human primary visual cortex. Magn Reson Med 1993;30:380 – 6.

Mikl M., Marecek R., Hlustík P., Pavlicová M., Drastich A., Chlebus P., Brázdil M., Krupa P.. Effects of spatial smoothing on fMRI group inferences. Magn Reson Imaging. 2008 May; 26(4): 490-503.

Moffitt M.A., Dale B.M., Duerk J.L., Grill W.M. Functional magnetic resonance imaging of the human lumbar spinal cord. J. Magn. Reson. Imaging 2005; 21, 527–535.

Nash P., Wiley K., Brown J., Shinaman R., Ludlow D., Sawyer A.M., Glover G., Mackey S.. Functional magnetic resonance imaging identifies somatotopic organization of nociception in the human spinal cord. Pain 2013; 154(6): 776-81.

Nejad K.K., Sugiura M., Thyreau B., Nozawa T., Kotozaki Y., Furusawa Y., Nishino K., Nukiwa T., Kawashima R.. Spinal fMRI of interoceptive attention/awareness in experts and novices Neural Plast.

2014; 2014: 679509.

Ng M.C., Wong K.K., Li G., Lai S., Yang E.S., Hu Y., Luk K.D.. Proton-density-weighted spinal fMRI with sensorimotor stimulation at 0.2T. NeuroImage 29 (2006): 995 – 999.

Nix W, et al. Comparison of vascular reactivity in spinal cord and brain. Stroke. 1976;7(6):560–563.

Ogawa S., Lee T.M., Nayak A., Glynn P.. Oxygenation-sensitive contrast in magnetic resonance image of rodent brain at high magnetic fields. Magn. Reson. Med. (1990a) 14, 68–78.

Ogawa S., Lee T.M.. Magnetic resonance imaging of blood vessels at high fields: in vivo and in vitro measurements and image simulation. Magn Reson Med. 1990b Oct; 16(1): 9-18.

Ogawa S., Lee T.M., Kay A.R., Tank D.W.. Brain magnetic resonance imaging with contrast dependent on blood oxygenation. Proc. Natl Acad. Sci. USA 87, 9868–9872 (1990c).

Ogawa S., Tank D.W., Menon R., Ellermann J.M., Kim S.G., Merkle H., Ugurbil K.. Intrinsic signal changes accompanying sensory stimulation: functional brain mapping with magnetic resonance imaging. Proc. Natl Acad. Sci. USA 89, 5951–5955 (1992).

Ohta S., Meyer E., Fujita H., Reutens D.C., Evans A., Gjedde A.. Cerebral [15O]Water Clearance in Humans Determined by PET: I. Theory and Normal Values. Journal of Cerebral Blood Flow & Metabolism (1996) 16, 765–780.

Owen A.M. and Coleman M.R.. Functional neuroimaging of the vegetative state. Nat Rev Neurosci 2008; 9(3): 235–43.

Pauling L. and Coryell C. D.. The magnetic properties and structure of hemoglobin, oxyhemoglobin and carbonmonoxy hemoglobin. Proc. Nayl. Acad. Sci. (1936) 22, 210-216.

Piche M., Cohen-Adad J., Nejad M.K, et al. Characterization of cardiac-related noise in fMRI of the cervical spinal cord. Magn Reson Imaging. 2009; 27(3): 300–310.

Poline J.B. and Brett M.. The general linear model and fMRI: Does love last forever? NeuroImage (2012); 62: 871–880.

Raichle M.E., MacLeod A.M., Snyder A.Z., Powers W.J., Gusnard D.A., and Shulman G.L.. A default mode of brain function. PNAS January 16 2001 vol. 98 no. 2: 676 – 682.

Raj D., Anderson A.W., Gore J.C.. Respiratory effects in human functional magnetic resonance imaging due to bulk susceptibility changes. Phys Med Biol 2001; 46(12): 3331–3340.

Restom K., Behzadi Y., Liua T.T.. Physiological noise reduction for arterial spin labeling functional MRI . NeuroImage 31 (2006) 1104 – 1115.

Reynell C. and Harris J.J.. The BOLD signal and neurovascular coupling in autism. Developmental Cognitive Neuroscience 6 (2013) 72 – 79.

Richter W. and Richter M.. The shape of the fMRI BOLD response in children and adults changes systematically with age. NeuroImage. 2003; 20(2): 1122 – 1131.

Rigamonti, Attilio, and Pietro Carretta. Structure of matter: an introductory course with problems and solutions. Springer, 2009.

Rutten G.J.M., Ramsey N.F., van Rijen P.C., et al. Reproducibility of fMRI-determined language lateralization in individual subjects. Brain Lang (2002); 80: 421 – 37.

Särkkä S., Solin A.,.Nummenmaa A, Vehtari A., Auranen T., Vanni S., Lin F-H.. Dynamic retrospective filtering of physiological noise in BOLD fMRI: DRIFTER. NeuroImage 60 (2012) 1517 – 1527.

Sasaki S., Yazawa I., Miyakawa N., Mochida H., Shinomiya K., Kamino K., Momose-Sato Y., Sato K.. Optical Imaging of Intrinsic Signals Induced by Peripheral Nerve Stimulation in the in Vivo Rat Spinal Cord. NeuroImage. 2002; 17(3): 1240 – 1255.

Savitzky A. and Golay M.J.E.. Smoothing and Differentiation of Data by Simplified Least Squares Procedures. Anal. Chem., 1964, 36 (8), pp 1627 – 1639.

Schmitt F., Stehling M.K., Turner R.. Echo-Planar imaging: theory, technique and application. Springer, Berlin, 1998.

Sladky R., Friston K.J., Tröstl J., Cunnington R., Moser E., Windischberger C.. Slice-timing effects and their correction in functional MRI. NeuroImage 58 (2011) 588–594.

Slichter, Charles P.. Principles of Magnetic Resonance, Third Edition, Springer-Verlag (1990).

Smith S.A., Edden R.A., Farrell J.A., Barker P.B., Van Zijl P.C.. Measurement of T1 and T2 in the cervical spinal cord at 3 tesla. Magn Reson Med 2008 Jul; 60(1): 213-9.

Smith S.M.. Overview of fMRI analysis. The British Journal of Radiology, 77 (2004), S167–S175.

Standring, Susan, et al. "Gray's anatomy: the anatomical basis of clinical practice." American Journal of Neuroradiology 26.10 (2005): 2703.

Stracke C.P., Pettersson L.G., Schoth F., Moller-Hartmann W., Krings T.. Interneuronal systems of the cervical spinal cord assessed with BOLD imaging at 1.5 T. Neuroradiology (2005) 47: 127 – 133.

Stroman P.W., Nance P.W., Ryner L.N.. BOLD MRI of the human cervical spinal cord at 3 tesla. Magn. Reson. Med. (1999). 42, 571 – 576.

Stroman P.W., Krausea V., Frankenstein U.N., Malisza K.L., Tomanek B.. Spin-echo versus gradient-echo fMRI with short echo times. Magn Reson Imag 19 (2001a) 827 – 831.

Stroman P.W., Krause V., Malisza K.L., Frankenstein U.N., Tomanek B.. Characterization of contrast changes in functional MRI of the human spinal cord at 1.5 T . Magnetic Resonance Imaging 19 (2001b) 833 – 838.

Stroman P.W. and Ryner L.N.. Functional MRI of motor and sensory activation in the human spinal cord. Magn. Reson. Imaging (2001), 19, 27 – 32.

Stroman P.W., Krause V., Malisza K.L., Frankenstein U.N., Tomanek B.. Extravascular proton-density changes as a non-BOLD component of contrast in fMRI of the human spinal cord. Magn. Reson. Med. 2002a. 48, 122 – 127.

Stroman P.W., Krause V., Malisza K.L., Frankenstein U.N., Tomanek, B.. Functional magnetic resonance imaging of the human cervical spinal cord with stimulation of different sensory dermatomes. Magn. Reson. Imaging 2002b. 20, 1 – 6.

Stroman P.W.. Magnetic Resonance Imaging of Neuronal Function in the Spinal Cord: Spinal fMRI.Clinical Medicine & Research. Volume 3, Number 3: 146 - 156 (2005).

Stroman P.W., Malisza K.L.. Functional magnetic resonance imaging at 0.2T. Neuroimage (2003a); 20: 1210 - 1214.

Stroman P.W., Tomanek B., Krause V., Frankenstein U.N., Malisza K.L.. Functional magnetic resonance imaging of the human brain based on signal enhancement by extravascular protons (SEEP fMRI). Magn Reson Med (2003b); 49: 433 – 439.

Stroman P.W., Kornelsen J., Lawrence J.. An Improved Method for Spinal Functional MRI With Large Volume Coverage of the Spinal Cord. JOURNAL OF MAGNETIC RESONANCE IMAGING 21: 520 – 526 (2005a).

Stroman P.W., Kornelsen J., Lawrence J., Malisza K.L.. Functional magnetic resonance imaging based on SEEP contrast: response function and anatomical specificity. Magnetic Resonance Imaging 23 (2005b) 843 – 850.

Stroman P.W.. Discrimination of errors from neuronal activity in functional MRI of the human spinal cord by means of general linear model analysis. Magn. Reson. Med. 56, 452–456 (2006).

Stroman P.W., Wheeler-Kingshott C.A.M., Bacon M., Schwab J.M., Bosma R., Brooks J.C.W., Cadotte D., Carlstedt T., Ciccarelli O., Cohen-Adad J., Curt A., Evangelou N., Fehlings M.G., Filippi M., Kelley B.J., Kollias S., Mackay A., Porro C.A., Smith S., Strittmatter S.M., Summers P., Tracey I.. The current state-of-the-art of spinal cord imaging: Methods. Neuroimage (2014); 84: 1070 - 81.

Summers P.E., Ferraro D., Duzzi D., Lui F., Iannetti G.D., Porro C.A.. A quantitative comparison of BOLD fMRI responses to noxious and innocuous stimuli in the human spinal cord. Neuroimage 2010 May 1; 50(4): 1408 - 15.

Symms M.R., Wheeler-Kingshott C.A., Parker G.J.M., Barker G.J.. ZOnally-magnified Oblique Multislice (ZOOM) EPI. Proc. Intl. Sot. Mag. Reson. Med. 8 (2000).

Thron A.K.. Vascular anatomy of the spinal cord: Neurological investigations and clinical syndromes. New York: Springer-Verlag; 1988. p 8 – 64.

Tofts Paul, ed. Quantitative MRI of the brain: measuring changes caused by disease. John Wiley & Sons, 2005.

Tousignant-Laflamme Y., Rainville P., Marchand S.. Establishing a link between heart rate and pain in healthy subjects: a gender effect. The Journal of Pain. 2005. Volume6, Issue6, June 2005, Pages 341–347.

Triantafyllou C., Hoge R.D., Krueger G., Wiggins C.J., Potthast A.,Wiggins G.C., Wald L.L.. Comparison of physiological noise at1.5 T, 3 T and 7 T and optimization of f MRI acquisition parameters. NeuroImage (2005); 26, 243 – 250.

Triantafyllou C., Hoge R., Wald L.. Effect of spatial smoothing on physiological noise in high-resolution Fmri. NeuroImage (2006); 32(2): 551 – 7.

Triantafyllou C., Polimeni J.R., Wald L.L. "Physiological noise and signal-to-noise ratio in fMRI with multi-channel array coils." Neuroimage 55.2 (2011): 597 – 606.

Valsasina P., Agosta F., Caputo D., Stroman P.W., Filippi M.. Spinal fMRI during proprioceptive and tactile tasks in healthy subjects: activity detected using cross-correlation, general linear model and independent component analysis. Neuroradiology (2008); 50: 895 – 902.

Valsasina P., Agosta F., Absinta M., Sala S., Caputo D., Filippi M.. Cervical cord functional MRI changes in relapse-onset MS patients. J Neurol Neurosurg Psychiatry (2010); 81: 405 – 408.

Valsasina P., Rocca M.A., Absinta M., Agosta F., Caputo D., Comi G. and Filippi M.. Cervical cord FMRI abnormalities differ between the progressive forms of multiple sclerosis. Hum. Brain Mapp. (2012). 33: 2072 – 2080.

Van den Aardweg J.G., Karemaker J.M.. Influence of chemoreflexes on respiratory variability in healthy subjects. Am J Respir Crit Care Med 2002; 165(8): 1041 – 1047.

Vul E., Harris C., Winkielman P., Pashler H.. Puzzlingly High Correlations in fMRI Studies of Emotion, Personality, and Social Cognition. Perspect. Psycholog. Sci. (2009) 4: 274 – 290.

Wall P.D., Merrill E.G., Yaksh T.L.. Responses of single units in laminae 2 and 3 of cat spinal cord. Brain Res 160: 245 – 260, 1979.

Wei P., Li J., Gao F., Ye D., Zhong Q., Liu S.. Resting state networks in human cervical spinal cord observed with fMRI. Eur J Appl Physiol. 2010 Jan; 108(2): 265 – 71.

Weibull A., Gustavsson H., Mattsson S., Svensson J.. Investigation of spatial resolution, partial volume effects and smoothing in functional MRI using artificial 3D time series. Neuroimage (2008); 41: 346 – 353.

Wheeler-Kingshott C.A.M., Parker G.J., Symms M.R., Hickman S.J., Tofts P.S., Miller D.H., Barker G.J.. ADC Mapping of the human optic nerve: increased resolution, coverage and reliability with CSF-suppressed ZOOM-EPI. Magnetic Resonance in Medicine (2002a); 47(1): 24 – 31.

Wheeler-Kingshott C.A.M., Hickman S.J., Parker G.J.M., Ciccarelli O.. Investigating cervical spinal cord structure using axial diffusion tensor imaging. NeuroImage 16, 93 –102 (2002b).

Wheeler-Kingshott C.A.M., Stroman P.W., Schwab J.M., Bacon M., Bosma R., Brooks J., Cadotte D.W., Carlstedt T., Ciccarelli O., Cohen-Adad J., Curt A., Evangelou N., Fehlings M.G., Filippi M., Kelley B.J., Kollias S., Mackay A., Porro C.A., Smith S., Strittmatter S.M., Summers P., Thompson A.J., Tracey I.. The current state-of-the-art of spinal cord imaging: Applications. The current state-of-the-art of spinal cord imaging: Applications. Neuroimage 84 (2014): 1082 – 1093.

Wilm B.J., Gamper U., Henning A., Pruessman K.P., Kollias S.S., Boesiger P.. Diffusion-weighted imaging of the entire spinal cord. NMR Biomed 2009, 22: 174 – 181.

Woods R., Cherry S., and Mazziotta J.. 1992. Rapid automated algorithm for aligning and reslicing PET images. J. Comput. Assist. Tomography, 16:620 – 633.

Worsely K.J. and Friston K.J.. Analysis of fMRI time-series revisited again. Neuroimage (1995); 2: 173 – 181.

Xie G., Piché M., Khoshnejad M., Perlbarg V., Chen J.I., Hoge R.D., Benali H., Rossignol S., Rainville P., Cohen-Adad J.. Reduction of physiological noise with independent component analysis improves the detection of nociceptive responses with fMRI of the human spinal cord. Neuroimage (2012); 63(1): 245 – 52.

Yacoub E., Duong T.Q., Van De Moortele P., Lindquist M., Adriany G., Kim S.G., Ugurbil K., Hu X.. Spin-echo fMRI in humans using high spatial resolutions and high magnetic fields. Magn Reson Med (2003); 49: 665 – 4.

Yoshizawa T., Nose T., Moore G.J., Sillerud L.O.. Functional Magnetic Resonance Imaging of Motor Activation in the Human Cervical Spinal Cord. Neuroimage (1996); 4: 174 – 182.

Zhao F., Williams M., Meng X., Welsh D.C., Coimbra A., Crown E.D., Cook J.J., Urban M.O., Hargreaves R., Williams D.S.. BOLD and blood volume-weighted fMRI of rat lumbar spinal cordduring non-noxious and noxious electrical hindpaw stimulation. NeuroImage (2008); 40: 133 – 147.